UC Santa Barbara
UC Santa Barbara Electronic Theses and Dissertations

Title

New Directions in Correlated Electronic Systems

Permalink

Author

Pawlak, Kelly Ann

Publication Date

2020

UNIVERSITY of CALIFORNIA

Santa Barbara

New Directions in Correlated Electronic Systems

A dissertation submitted in partial satisfaction of the

requirements for the degree of

Doctor of Philosophy

in

Physics

by

Kelly Ann Pawlak

Committee in charge:

Professor Cenke Xu, Chair

Professor Chetan Nayak

Professor David Weld

June 2020

The dissertation of Kelly Ann Pawlak is approved:

_____

Professor Chetan Nayak

_____

Professor David Weld

_____

Professor Cenke Xu, Chair

June 2020

KELLY ANN PAWLAK

Condensed Matter Physics, Ph. D.
Applied and Computational Mathematics, B.S.

CA, USA   kapawlak@ucsb.edu   (732) 763-6002

EDUCATION

Ph.D. Condensed Matter Physics   Sep 2014 – Jun 2020

University of California, Santa Barbara

  Masters degree awarded 2017
  Advisor: Cenke Xu
  Thesis: *New Directions in Strongly Correlated Materials*

B.Sc. Physics   Jan 2010 – Jun 2014

Florida State University

  Honors; GPA: 3.82/4.00
  Advisor: Oskar Vafek

B.Sc. Applied and Computational Mathematics   Jan 2010 – Jun 2014

Florida State University

  Honors; GPA: 3.96/4.00
  Advisor: Ziad Musslimani
  Hon. Thesis: *Self-Dual Nonlinear Schrodinger Equation*

AWARDS

UCSB Graduate Fellowship   Sep 2018 – May 2019

  $24K/yr (1 year)

NSF Graduate Research Fellowship   Sep 2014 – May 2018

  $34K/yr (3 years)

UCSB P.Broida Fellowship   Sep 2014 – May 2014

  $3K/yr (1 year)

Undergraduate Awards   Jan 2013 – Sep 2014

  FSU Research and Creative Activity ($4k); 1st Place Lanunutti Physics Research
  Award ($750); FSU Honors Thesis Award ($600); NSF Travel ($ 500);

Organizations (Undergraduate)   Jan 2013 – Sep 2014

  Pi Mu Eplsion Mathematics Society (Historian, President), Sigma Pi Sigma
  Physics Society (President), Phi Beta Kappa Honors Society

RESEARCH EXPERIENCE

Graduate Researcher   Sept 2014 – Ongoing

University of California, Santa Barbara

  Theory: Phase transitions and exotic phenomena of novel solid state materials

Research Assistant   Jun 2013 – Sep 2014

National High Magnetic Field Laboratory

  Theory: Unconventional Superconductivity and Emergent Phases

PUBLICATIONS

Journal Articles

Wu, Xiao-Chuan, Anna Keselman, Chao-Ming Jian, Kelly Ann Pawlak, and Cenke Xu (2019). "Ferromagnetism and spin-valley liquid states in moiré correlated insulators". In: *Physical Review B* 100.2, p. 024421.

Wu, Xiao-Chuan, Kelly Ann Pawlak, Chao-Ming Jian, and Cenke Xu (2018). "Emergent Superconductivity in the weak Mott insulator phase of bilayer Graphene Moiré Superlattice". In: *arXiv preprint arXiv:1805.06906*.

Bi, Zhen, Chao-Ming Jian, Yi-Zhuang You, Kelly Ann Pawlak, and Cenke Xu (2017). "Instability of the non-Fermi-liquid state of the Sachdev-Ye-Kitaev model". In: *Physical Review B* 95.20, p. 205105.

Pawlak, Kelly Ann, James M Murray, and Oskar Vafek (2015). "Emergence of superconductivity in a doped single-valley quadratic band crossing system of spin-1/ 2 fermions". In: *Physical Review B* 91.13, p. 134509.

Conference Proceedings

Murray, James, Kelly Pawlak, and Oskar Vafek (2015). "Interaction-driven phase instabilities in two-dimensional quadratic band touching systems". In: *APS Meeting Abstracts*.

Presentations

Pawlak, Kelly (2017). *The Sachdev-Ye-Kitev Model: Overview and New Results*. University of Geneva, CH, Colloquiumm.

Pawlak, Kelly A (2014). *Emergence of Superconductivity in Doped Quadratic Band Touching Systems*. University of Colorado, Boulder, CO, Poster.

Pawlak, Kelly (2013). *Stability of Bose-Einstein Condensates in a Random Potential*. IMACS, Contributed Talk.

TEACHING EXPERIENCE

Advanced Laboratory (Course Author, TA)   May 2019 – Ongoing
University of California, Santa Barbara

OUTREACH

Outreach Alliance – FSU   Sep 2013 – Sep 2014
As an extension of the NSF Funded STARS Alliance program, I worked with a start-up RSO to create a network of university student groups and local school district administrators for the purpose of direct collaboration on outreach projects. I managed a flagship group of physics students (communication, supplies, schedules) in outreach projects around the county.

ADDITIONAL TRAINING

FTPI Summer School   2016
Fine Theoretical Physics Institute

NHMFL Theory Winter School   2015
National High Magnetic field Laboratory

Boulder School in Materials Physics   2014
Department of Physics, U. Colorado, Boulder

Laboratory Research Assistant   2010-2012
Florida State University
  Photochemistry; Supervisor: Jack Saltiel

Abstract

New Directions in Correlated Electronic Systems

by

Kelly Ann Pawlak

Despite great theoretical effort since the conception of manybody physics to elucidate the nature of interacting fermions — in a precise and quantitative manner — the phase diagrams of many correlated electronic systems remain impenetrable to even the most rigorous and skilled approaches. In this manuscript I detail the new techniques, models, and solid-state materials that lie along the contemporary boundaries of scientific understanding in strongly correlated materials. In particular, I discuss the fundamental obstacles of manybody electronic systems and discuss how these issues are exemplified by the various results reviewed. The work presented in Chapters 2-4 are representative of my time at UCSB, and reflect the collaborations and publications of my Ph.D.

Contents

Chapter 1

Introduction

Despite great theoretical effort since the conception of manybody physics to elucidate the nature of interacting fermions — in a precise and quantitative manner — the phase diagrams of many correlated electronic systems remain impenetrable to even the most rigorous and skilled approaches. The difficulty in understanding correlated electronic systems are two-fold, and this manuscript aims to stress the following essential points:

1. Manybody physics is generically difficult in the presence of interactions

2. Fermionic degrees of freedom adjoin additional complexity due to the Pauli-exclusion principle and anti-symmetry.

This thesis is structured as follows: The remainder of Chapter 1 is dedicated to the discussion of the essential theoretical aspects manybody physics, approaches to interacting theories, the unique properties of fermions and ramifications of these from a theoretical standpoint. It has been written with the intention of providing a broad conceptual

overview of physics the author considers foundational in approaching the issues described.

Following this discussion, we detail work done on three systems. Chapter 2 is a recount of a 2015 publication [78], in which we study a continuum theory that demonstrates the emergence of strongly correlated behavior in an system with an arbitrarily weak coupling. This work demonstrates the failure of mean field theory to accurately predict macroscopic phenomenology of a relatively simple system, highlighting the importance of rigorously treating correlations in manybody systems. We find that the failure of mean field theory hinges upon a high degree of symmetry in the underlying theory, where multiple symmetry breaking terms become "intertwined" under renormalization, leading to unconventional and topological orders.

In Chapter 3, we move to focus on strongly-coupled systems and their emergent properties. Here we review the Sachdev-Ye-Kitaev (SYK) model, an exactly solvable model of strong correlations that gives rare insights into exotic quantum critical fermionic phases and their instabilities. After summarizing the basic features of the model, we discuss the work presented in Ref. [7], which demonstrated the first known instabilities of the SYK Non-Fermi liquid Phase.

Finally, in Chapter 4, we give a detailed overview of a fresh experimental platform, Magic Angle Moire Systems, that can tune between the weakly and strongly coupled regimes. This new material class has a high fabrication yield, low disorder and can be tuned non-destructively by gate voltages — allowing experimentalists to traverse the entire phase diagram for each sample, in contrast to conventional materials which must be,

e.g., chemically doped. This tunability promises unprecedented potential to reform both our fundamental understanding of correlated systems as well as our theoretical approach. After a review of the material properties and prominent models, we move on to review two specific models. We first consider a work [115] that proposes an explanation for the observed Ferromagnetic correlated insulating states and superconductivity in some systems. Following this, we move on to discuss the peculiar features of superconductivity in some of these systems, and a possible origin of the phenomenology published in Ref. [116]

1.1 Manybody Physics: Interaction, Correlation, Emergence

As theorists advancing the bleeding edge of correlated physics, we must unambiguously define the barriers that have limited our success. Precise, contextual characterization of these problems should lead to clever improvisation — and hopefully fresh solutions.

There exists a perennial misrepresentation of the fundamental difficulty in manybody physics, namely, that the sheer number of degrees of freedom (DOFs) — whether these are $N = 10^{26}$ electrons in a crystal or $N = 10^4$ microbes in a swarm – is the singular crux of the theorist's agenda. Quite contrarily, for the physicist interested in the statistical, macroscopic, quantities characterizing the collective state of such a system – the observables which are typically useful, and physically accessible by experiment — this multitude presents itself, decisively, as a benefit.

In fundamentally stochastic systems, a large-N number of identical constituents often implies heavily damped fluctuations about mean behavior, in a fashion akin to the Central Limit Theorem — as any student of statistics might tell you, in this *thermodynamic limit*, macroscopic observables representing averaged behavior become highly predictive, else deterministically related by state equations. The parameter dependence of such observables charts out a phase diagram — a paradigm of manybody theory, meaningful only in the large-N— which categorizes qualitative behavior of the system as parameter regions delineated by phase transitions and cross-overs. The most trivial example of a "Large-N" theory is the free Ising model in an external field h, who's energy and evolution is calculated via the many-body Hamiltonian over all sites:

$$H_I = -\sum_i^{\text{sites}} h \cdot \sigma_i \tag{1.1}$$

Statistical behavior of the system at a given temperature is contained in the partition function, which by virtue of site independence, can be exactly computed for arbitrarily large systems:

$$\mathcal{Z}[\beta] = \sum_{\sigma_i = \pm 1} e^{-\beta \sum_i h \cdot \sigma_i} = (2 \cosh(\beta h))^N \tag{1.2}$$

as can the mean magnetization, $M = \frac{1}{N} \sum_i \sigma_i$, and its fluctuations about the mean behavior, $\delta \bar{M}$:

$$\bar{M} \equiv \langle M \rangle = \tanh(\beta h)$$

$$\delta \bar{M} \equiv \sqrt{\langle M^2 \rangle - \bar{M}^2} = \frac{\text{sech}(\beta h)}{\sqrt{N}}$$

The reader should notice that in the above expression, the fluctuations about the mean vansh with increasing N as expected for a well-behaved statistical system. Indeed as N grows towards infinity, our mean-field solution becomes increasingly accurate. This can be understood in the context of statistics, since the partition function factorizes into a product of independent systems, $\mathcal{Z}[\beta] = \prod_i (\mathcal{Z}_i[\beta])$, so that we can define the characteristic function over the entire system as

$$\varphi \equiv \langle e^{i \sum_i \sigma_i x_i} \rangle = \prod_i^N \langle e^{i\sigma_i x_i} \rangle = \prod_i^N \varphi_i \tag{1.3}$$

By the Central limit theorem, it can be shown that the product of the characteristic functions of a number of density functions tends to the characteristic function of the normal density as the number of density functions increases without bound, implying that the resultant distribution for any simple macroscopic quantity should limit to a Gaussian. Our ability to reduce the problem to this form hinges upon the factorization of the partition function into a Large-N product — a process that is ambiguous, if not impossible, in most manybody problems of interest.

If large-N works to our advantage, we must carefully reconsider our intuition: The difficulty in manybody physics — and the connecting theme between the otherwise distinct systems reviewed in this manuscript — arises from the *interactions* between the N microscopic constituents. In a *free theory*, defined by the absence of interaction, DOFs maintain complete independence — one simply solves for the single particle behavior and computes observables with respect to N ensembles. Interactions, from a statistical viewpoint, induce correlation, which generally requires simultaneous solutions involving large

sets of — if not all — relevant DOFs within a system. In this sense, a correlated system of a large N number of constituents is, in the worst case, more accurately described as a $N = 1$ system of extreme complexity involving N variables, hence leaving the laws of statistics helpless.

This perspective is perhaps best captured in the quenched-disorder Edward-Anderson Spin Glass model:

$$H = \sum_{\langle ij \rangle} J_{ij} \sigma_i \sigma_j, \tag{1.4}$$

where we imagine a classical spin system with randomly chosen couplings between all neighbors. The problem of characterizing the low-energy states for an arbitrary realization of the couplings is hard in the literally sense — the problem has been shown to be NP-Hard [4]. However, this model validates our nuanced understanding of large-N in a satisfying way: partial solubility occurs when theorists make large-N even *larger*. Indeed, the few macroscopic characteristics we are actually able to compute hinge upon applying, typically via the Replica Trick, a *disorder average* over the couplings J_{ij}, — in essence making a parametrically large number of fictitious interacting *copies* of this system — to enable the use of statistics. Even with these tools, this problem is still difficult, and further simplifications, such as all-to-all couplings, must be made, as well as elaborate accounting for the interactions of replicas themselves, as first pointed out by Mezard *et. al.* [67].

We should understand that, unlike free theories, there is no sense in which the model of Eq 1.4 results in a $\mathcal{Z}[\beta]$ that factorizes, even approximately. However, we see that the

partition function of the system, following the replica trick, can be written as product of N_r copies, $\sim (\mathcal{Z}[\beta])^{N_r}$, and the correlations of observables between copies are sufficiently weak for most analyses. We conclude that a truly large-N system is hence one that may be written, or well-approximated, by $\mathcal{Z} = (\mathcal{Z}_s)^N$. In the case that such a description does not exist, the large-N adage takes shape in a meaningful form: when our system is indivisible, we must somehow understand the behavior of a *single* system of exceptional functional complexity by building upon the equations which govern its N correlated moving parts. Our problem becomes determining the extent to which correlation obfuscates independence and, hence, the degree to which statistics can rescue our efforts.

While the spin glass model may appear pathological due to the extensive number of couplings — and hence lack of symmetry – quite generally, interacting problems are not solvable, even in ideal statistical limits. This is evidenced by a profound dearth of exact solutions for even the most simply articulated systems. This complexity is further escalated in the case of mobile particles, whose free theory contains *transport* terms that rouse non-local correlations across the system in a manner that is sensitive to dimensionality, symmetry and the mathematical structure of any interaction terms. Arguably, the combination of transport and interaction accounts for the most damning explosions of complexity, usually only approachable using sophisticated field-theoretic techniques and speculative approximations.

The nature of transport and the role of dimensionality in the orchestration of complexity in a manybody system warrants a short discussion for intuition. Consider a simple

model of a diffusive random walk on a d-dimensional isometric lattice, where the particles of the system have an equal probability of moving onto any neighboring site. In the absence of interactions, it can be shown that in dimensions $d \leq 2$, the probability of two particles meeting in space at some point in time tends to unity as $t \to \infty$, even when the particles are infinitesimally small [102]. In the presence of local interactions, the *reentrant* behavior of the low dimensional system *greatly* increases the frequency of these events. In higher dimensions, however, interactions play a weaker perturbative role, ultimately having little to no effect on the macroscopic behavior unless the particles are designated with a finite size. We find that this actually leads to dramatic results, and that in some cases, interactions may never be neglected regardless of how weak they are [103].

The final topic to consider in this section is how one actually approaches these problems. For a system of interest, a mathematical prognosis can be developed by asking a series of insightful questions. The following list is a non-exhaustive, but frequently reference list of questions typically asked, and reflect the main tactics represented in this thesis:

Can we neglect or approximate interactions permissibly?

As a first approach, one usually takes two historically defensible limits that permit approximate treatment. These are the *weak* and *strong* coupling limits, and represent hopeful regimes where we separately focus on the constituents and the whole, respectively. In the former, one presupposes that the free, single particle, theory dominates equilibrium, and calculates perturbative corrections to observables with respect to a small

coupling constant. In the latter, the free theory is treated as a perturbation to a new problem defined by the interactions alone, when analytical progress is possible.

The intuition behind these approaches is somewhat obvious: we might expect that the low energy states of a given system should look like the low energy states of the most important term in the model. This approach has success in theories that don't suffer from intermediate couplings, multiple particle species, high degrees of symmetry, low dimensional physics or other origins of correlated error. Ultimately, the implicit connotation that perturbative treatments beget small deviations in macroscopic observables is wholly misleading at best; in fact, these limits are always far from trivial in interesting systems, and a naive application of such approaches should inevitably produce incorrect answers.

What this approach does help with, however, is the identification of phase transitions: If the two limits of an interacting theory have distinct low energy phases, there must be at least one phase transition or crossover between them. Moreover, the symmetry properties of the two limiting phases can offer clues to deduce the kind of transition that occurs, especially in $T = 0$ quantum phase transitions.

Can we identify collections of variables whose behavior is essentially uncorrelated?

Another useful tool is to make a change of variables. For example, in an interacting bose gas, a common canonical transformation is to separate fields the atomic fields into their

amplitude ($\sqrt{\rho}$) and phase (ϕ), resulting in an action

$$\int d\tau d^d r \left[\frac{1}{g}(\partial_\tau \phi)^2 + \frac{\rho}{m}(\nabla \phi)^2 + g\rho^2 \right] + \mathcal{S}_0[\rho]. \tag{1.5}$$

Such a transformation makes apparent the fact that the interactions are most important to the amplitude dynamics which govern the local density of the gas. The phase DOF of the bosons, however, is well approximated by a massless free theory for ρ held constant, allowing us to partially solve the theory. As it turns out, the phase dynamics are the most important aspect of this theory, and describe a large swath of superfluid phenomenology at low energies, where the amplitude degrees of freedom are "frozen out" due to the mass term. This tool is a common prescription across many systems, especially those with charge-spin separation, containing particles or quasi-particles whose single-particle phase space can be modeled as the direct product of a rotor and scalar degree of freedom.

Can we reduce complexity by sifting out the physics which dominates macroscopic behavior?

Often it is found that the microscopic details of a theory play little to no role in the emergent macroscopic description we seek. In such cases — when we are interested in the long-time, large scale leading functional behavior of order parameters — we can approach a theory by the process of renormalization. In the way that the central limit theorem tells us that the distribution of sample means (from PDFs with well defined first and second moments) approaches a gaussian, renormalization applies local averages over DOF to generate a limiting scale-invariant theory. Such theories define *universality*

classes, characterized by critical exponents governing correlation functions, to which many distinct microscopic models may belong to. We consider these theories to be *emergent* since they arise from the correlations of many DOF rather than the microscopic description of the model.

In the most exotic cases, emergence can lead to continuum theories that emulate famous gauge theories of the Standard Model, a hallmark of frustrated magnetic systems. Many interacting electronic theories on symmetric lattices, such as those to be discussed, have emergent superconducting phases despite their microscopic theory lacking the conventional BCS terms– or attractive interactions at all. Emergence is, of course, not limited to quantum mechanical systems: perhaps most astounding is that even classical ecology problems, governed by stochastic Lotka-Voleterra equations under rigorous treatment, have effective descriptions given by the *Reggeon Theory* of QCD [102].

Summarily, the correlations between variables, and not their multiplicity, is what makes manybody physics famously difficult. It is also what makes the field so interesting — these perceived analytical failures are symptomatic of a grander phenomenon that only occurs in interacting systems at large-N: emergence, which indicates the existence of an effective analytical description of a system, usually over large spatio-temporal scales, which is qualitatively distinct from the underlying microscopic theory. Here the appropriate description of the system is not based on the original particles, but rather effective excitations capturing the essential qualities of the low-energy physics, which may have distinct states and symmetries, whose interactions and transport often retain no sem-

blance to those of the former. Theories that lead to emergent physics are intrinsically interesting. They also tend to have practical engineering value as in high temperature superconductivity, and especially in the emerging field of quantum computation and information science.

1.1.1   Manybody Fermions: An Overview

The counter-intuitive nature of fermions and the novelty of their manybody phases may be entirely traced back to two properties which, to the best of our knowledge, must be defined axiomatically based on empirical evidence. The first is their the mutual exclusion: for half-odd-integer spin particles, it is only possible for a single particle to occupy a given state. This result is known to quantum physics as the Pauli-Exclusion principle, but it is not necessarily unique to fermions — hardcore bosons and other classical DOF can exhibit "effective" mutual exclusion, especially in a local basis. For systems amenable to an occupation-basis (i.e. second quantized) description – including many classical non-equilibrium systems– exclusion leads to a *local* anti-commutation relation $\left\{a_n, a_n^\dagger\right\} = 1$.

The second property is *global* exchange anti-symmetry, which appears to be unique to elementary fermions. Given a manybody wavefunction, anti-symmetry implies that the exchange of any two identical particles results in a multiplicative phase: $|\Psi(f_1, f_2, \dots)\rangle = -|\Psi(f_2, f_1, \dots)\rangle$. It should be understood that this is a completely non-local effect. In a second quantized form, this generalizes the previous anti-commutation relations to $\{a_n, a_m^\dagger\} = \delta_{nm}$ and $\{a_n, a_m\} = \left\{a_n^\dagger, a_m^\dagger\right\} = 0$. In this form, it's clear that Pauli

exclusion can, in a sense, be seen as a consequence of anti-symmetry; however, given the appearance of exclusion in beyond elementary fermions, this attribution may be misguided. Mathematically, it is possible to define various kinds of mutual exclusion (see para-statistics, quons, etc and their applications) as well as various phase relations under exchange (e.g. anyons) that generalize the boson and fermion statistics; ultimately these need not be explicitly related, and their effects on manybody physics are distinct.

With these properties in hand, we must now understand how and to what extent our manybody calculations should be affected. We begin our discussion in the absence of interactions. For a free theory, wherein one only needs to consider N ensembles of a single particle state, exclusion becomes a passive variety of interaction: the system can no longer be a product of N identical single-particle states – each successive particle must instead occupy the lowest energy (E) state available, leading to the *filling* of an energy band. It is then clear that, for fermionic particles, the precise functional form of the Density of States (DoS, $g(E)$), even at low temperatures (T), plays dominant role in the macroscopic physics.

To demonstrate how exclusion alters the statistical nature of our solutions, we begin with a simple non-interacting gas of fermions. The partition function, however, now only runs over singly occupied states

$$\mathcal{Z} = \sum_{\{n_k\}=0,1} e^{-\beta \sum_k (\epsilon_k - \mu) n_k} \tag{1.6}$$

where ϵ_k is the momentum-dependent energy level and μ the chemical potential. The above partition function leads to the most important equation for fermion systems,

namely the Fermi-Dirac (FD) distribution:

$$\langle n_k \rangle = \frac{1}{1 + e^{\beta(\epsilon_k - \mu)}} \tag{1.7}$$

which traces out a steep sigmoid curve at low temperatures. The variance in occupation at any finite is given by $\text{var}(n_\epsilon) = \langle n_\epsilon \rangle (1 + n_\epsilon)$, and gives an intuition for the smearing of occupancies in thermal systems.

The FD distribution ultimately sets our first approximations for the properties of real materials if we assume that we can apply an independent electron approximation. Contrary to classical and bose particles, each fermion in a free system has a mean equipartition energy $\frac{E}{N} = \frac{3}{5} k_b T$, leading to drastic changes in the various macroscopic order parameters that govern thermodynamic systems. Most notable of these is the suppression of the specific heat, $c_V = \frac{\partial}{\partial_T} \left(\frac{2}{V} \sum_k \epsilon_k \langle n_k \rangle \right) = \frac{\pi^2}{2} \frac{n k_b^2 T}{\epsilon_f}$, accounting for the lack of obvious electron contribution at room temperature in many real materials. The FD distribution also gives us an approximation for other quantities such as T^2 temperature dependence on resistivity at low temperatures and B^2 magneto resistance scaling, which have remarkable agreement with empirical studies in many systems. In the next section we will explain why the independent electron approximation seems to apply to systems that naturally contain interactions, despite the previous lengthy discussion about correlations.

1.1.2 Fermi Liquid Theory

Much of our progress in Condensed Matter physics has relied on the unprecedented reliability of the independent electron approximation. The explanation for this is the

domain of Landau's Fermi Liquid (FL) theory, which posits that the fundamental physics which governs single electron states — *i.e.* exclusion and band filling — is applicable to many interacting theories, and is wholly responsible for the observed macroscopic behavior. In short, FL theory asserts that many interactions do not fundamentally alter the basic statistical analysis of manybody fermions, and that a "redressing" of constants in an interacting theory will reveal that the macroscopic behavior is still captured by a Hilbertspace constructed from N independent fermionic DOF, even if these "quasi particles" are not necessarily the same fundamental DOF of the microscopic theory.

The construction of FL theory relies on a thought experiment such that imagine a continuous, *adiabatic*, process where we slowly turn on an interaction starting in a free theory, leading to two important effects

1. The energies of single-fermion states are modified in some continuous way

2. The introduction of the interaction now permits the scattering of fermions into and out of energy levels above the fermi-surface at $T = 0$.

The first point is trivial in the sense that, depending on the nature of the introduce interaction, we would expect a shift in occupation energies corresponding to states which maximize or minimize this new energetic constraint. The second point is more nuanced — what is hidden here is the breaking of a local conservation principle, namely, that in a free fermion theory the number of fermions occupying a given state, $n_{\epsilon(\vec{k})}$, is *conserved*. One interactions are turned on, however, there is no guarantee that these continue to represent "good" quantum numbers.

15

To make the this point explicit, we can look at how interactions change the possible transitions of a fermi gas by inspection of the Hamiltonian, containing a two-body interaction $V(\vec{x}_1 - \vec{x}_2)$, in matrix form:

$$
\begin{aligned}
H &= H_0 + H_{int} \\
&= \sum_{\vec{k}} \epsilon(\vec{k})|\vec{k}\rangle\langle\vec{k}| + \sum_{\{\vec{k}\}} \delta^{2\pi}(\vec{k})V(\vec{k}_1,...,\vec{k}_4)|\vec{k}_1,\vec{k}_2\rangle\langle\vec{k}_3\vec{k}_4|
\end{aligned}
\tag{1.8}
$$

where $\delta^{2\pi}(\vec{k}) = \delta\vec{k}_1 + \vec{k}_2 - \vec{k}_3 - \vec{k}_4 + n2\pi$ enforces conservation of momentum in a clean lattice. We see that the effect of V is to mix the free eigenstates by electron-electron scattering in momentum space. This reorganizes the partition function as

$$
\begin{aligned}
\mathcal{Z} &= \sum_n \frac{(-\beta)^n}{n!} \mathrm{Tr}\left((H_0 + H_{int})^n\right) \\
&= \sum_n \frac{(-\beta)^n}{n!} \mathrm{Tr}\left(H_0^n + \sum_m H_0^{n-m}H_{int}H_0^{m-1} + \cdots H_{int}^n\right)
\end{aligned}
\tag{1.9}
$$

where it is clear that the Boltzmann weights for states are now scrambled by transitions under the action of H_{int}.

The validity of FL theory depends on the extent to which these scatterings alter the low energy behavior of the macroscopic system. One way to evaluate the "goodness" of the single electron states is to calculate their lifetime, or relaxation time τ, in the presence of an interaction. This is a measure of how quickly single particle states decay into other excitations. In a free fermion system, the lifetime of particle excitations at $T = 0$ is always infinite, as required by mathematics — as eigenstates of the Hamiltonian, they may only incur a phase rotation in their amplitude. Turning on interactions, however, these states develop a finite half-life due to the transitions.

The structure of Eq. 1.8 becomes useful for determining the validity of FL theory. Due

to energy conservation, scattering events must satisfy the constraint $\epsilon(k_1)+\epsilon(k_2) = \epsilon(k_3)+$
$\epsilon(k_4)$. Furthermore, the Pauli exclusion principle dictates that fermions with $\epsilon(k_1), \epsilon(k_2)$
must be scattered into *unoccupied* states at $\epsilon(k_3), \epsilon(k_4)$. Given these constraints, we can
employ the adiabatic argument alluded to in the beginning of the section: As we turn
on infinitesimal interactions around $T = 0$, H_{int} cannot act non-trivially on fermions
at the fermi surface, $\epsilon(k_f)$, since it is not possible to simultaneously satisfy momentum
conservation and the Pauli exclusion principle unless all $\epsilon(\vec{k})$ are identical— there are no
available states for an electron to scatter into, since one of them would need to scatter
into a state below the filled fermi-surface. This implies that the particle lifetime near the
fermi-surface is *infinite* at $T = 0$.

If H_{int} acts on a fermion just above the fermi-surface, then the space of solutions has
a finite measure. In this case, the width of the shell dictating the constraints is of the
order $W = |\epsilon(k_1)-\epsilon_f|$, leading to a lifetime proportional to W^{-2}. Once we allow for finite
temperature, we then have to consider $g(E)$, where state occupancy is smeared around
around the fermi-surface by a thermal width $\epsilon_f \pm k_b T$, which by a similar argument gives
$\tau \propto \frac{1}{(k_b T)^2}$

If the half-life is large enough, which by the above arguments can be made by ap-
proaching low enough energies and temperatures, we can likely ignore the contributions
without consequence, leading to a new FL description of the interacting theory made
by renormalizing the energies and parameters due to 2nd order and higher perturbative
contributions from H_{int}. Here we are free to continue using the independent electron

approximation, and the system can be considered a veritable Large-N statistical problem, which, as we have belabored previously, is the idealistic scenario in a many-body problem.

Conversely, in cases that interactions cause frequent scatterings or induce the formation of bound states, our macroscopic theory can no longer be described by a naive independent electron picture: strongly correlated principles take effect and we must proceed with caution, attempting to find a set of variables that may be utilized for an adequate description of the system. In particular, FL theory fails in the presence of additional excitations — such as phonons, photons or other effective gapless or bosonic modes, possibly due to symmetries — can mediate electron dynamics. In these cases, the above construction of FL theory fails, since the energy conservation ceases to restrict the scattering phase space of the excited electrons. We will also see that FL theory requires a finite fermi-surface, and that the above arguments have no domain over systems tuned to band-touching points such that the fermi-surface becomes approximated by single point.

1.1.3   Other Fermionic Phases

While the FL theory of the above, along with band theory, offers insights into the nature of metals, semi-conductors, band insulators, gasses and some semi-metals, it fails to account for the qualitative behavior of many electron systems with strong interactions, low dimensions, high-degrees of symmetry, topological band structures or phonon interactions. We give a brief review of some of these systems.

Mott Insulators: When interaction strengths are strong, H_{int} can dominate the low energy phase description. Our approach to FL theory is then reversed, starting from the fully localized electron eigenstates, and slowly turning on transport. Particularly in crystalline materials at integer fillings, coulomb interactions can stifle electronic transport, such that the leading order terms, like exchange interactions, become effective spin (and valley) couplings of the localized electrons. In these circumstances, the theory can be well approximated by one of many interacting spin models that describe magnetic systems, such as the Heisenberg model. Depending on the symmetries of these models, the low lying excitations can be particle-like such as magnons, or gapless excitations over a continuous symmetry group. The breadth of these works is beyond the scope of the present discussion, but is discussed in nearly any solid state or condensed matter text book.

Topological Insulators: Another insulating phase occurs, counter-intuitively, for some free and weakly coupled fermion systems on finite lattices that are invariant under time reversal and have a topologically protected gap in the bulk. These systems are hallmarked by their conducting surface states described by gapless Dirac fermions, which propagate along the boundaries of the material. Carriers in these surface states have their spin locked at a right-angle to their momentum. At a given energy the only other available electronic states have different spin, so back-scattering scattering is strongly suppressed and conduction on the surface is highly metallic. Non-interacting topological insulators are characterized by integer a topological invariant derived from the Brillouin

zone of the relevant band structure, which cannot be changed in the absence of impurities or removal of the bulk gap. The behavior of these systems is superficially similar to 2D electron gasses in strong magnetic fields.

Topological order: Magnetic systems with high degrees of frustration can give rise to emergent quasi-particles that don't obey either bose or fermi statistics. The most famous example it Kitaev's exactly solvable Toric code [51], with more recent work focusing on frustrated itinerant magnetic systems. These theories have the celebrated feature of giving rise to emergent gauge theories, including those with similarity to QED and QCD, which ultimately stem from invariance of order parameters under many symmetry transformations. Some such systems feature novel critical deconfinement transitions where the quasi-particles, otherwise in strong bound states, transition into a asymptotically free phase with only weak coupling. In this phase, the unique mutual statistics of these particles allow for fault-tolerant quantum computation, making them a popular subject of study in condensed matter physics.

Superconductivity: On the other hand, we also find that interacting fermion systems give rise to transport-dominated orders distinct from FL. For example, when coupled to phonon modes of a lattice, the effective interaction between electrons can become attractive, leading to strong pairing in low dimensional systems. These Cooper-pairs of Bardeen–Cooper–Schrieffer (BCS) theory result in effective *bosonic* quasi-particles which can undergo bose-einstein condensation. The resulting band structure of the bosonic theory typically features a gap about the original fermi-surface of size $\Delta \sim k_b T_c \sqrt{1 - T/T_c}$

that suppresses the breaking of pair wavefucntions. In this low-energy bound state, BCS theory predicts the expulsion of a magnetic field from the superconductor and the variation of the penetration depth with temperature. It also describes the variation of the critical magnetic field with temperature relating the $T = 0$ critical field to the value of the transition temperature and the density of states at the Fermi level. Most famously, the local $U(1)$ symmetry of the bound-state permits the existence of the persistent, resistance-free, currents known to superconductivity.

One of the greatest mysteries in correlated electronic systems is the occurrence of High Temperature Superconductivity, which cannot be explained by the otherwise highly successful BCS model with a theoretical limit of $T_c \sim 30K$. The main class of high-temperature superconductors are the cuperates, distinguished for their 2D copper-oxide planes thought to play the largest role in conduction, with upper T_c's in the range of $150K$. With extremely complicated substructures stemming from their complex lattices, as well as doping and stoichiometric disorder, the origin of HTSC in these compounds, as well as many of their intermediate temperature phases, is poorly understood. In addition to these, iron-based compounds are intensively studied, and despite a nearly identical phase diagram, their unconventional superconducting physics seems to be governed by an alternate "heavy fermion" phenomenology.

Non-Fermi-Liquids: Many of the mentioned low-temperature phases discussed, especially high temperature superconductors, share a unique fate in the finite temperature regime in the vicinity of their critical point. In this quantum-critical regime, the tense
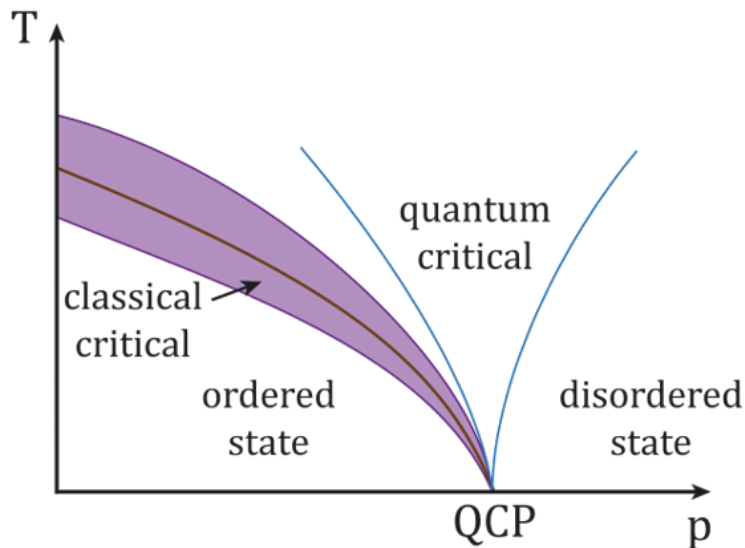
Figure 1.1: A typical phase diagram of correlated electron systems

competition between ordering and scattering processes seems to appears to lead to a universal phase that has no quasi-particle description. Also refereed to as "Strange Metals", Non-Fermi Liquids (NFL) represent a strong deviation from the ordinary description of fermonic theories, most notably producing a linear T dependence on resistivity and plankian dissipation. Despite the ubiquity of this phase in many correlated systems, little is known about its phenomenology or instabilities to ordered phases. We review and discuss the aspects of these systems in great depth throughout Chapter 3.

1.1.4 In Conclusion

In this chapter we covered some of the essential aspects of correlated systems that lead to high degrees of complexity and frustration in theoretical work. Despite the largeness of N in these systems, correlation between DOF often render blunt statistical analyses

useless. In order to make progress in our understanding, we must make use of clever and creative techniques, and limit our ambitions to approachable questions. In the case of fermionic systems, the Pauli exclusion principle along with exchange symmetries leads to new diverse behavior. We found that in some cases the net effect of these phenomena were actually beneficial from a discussion of FL theory— revealing that free approximations have a wider range of applicability than one might expect. However, the properties of fermions often increase mathematical complexity in the most interesting systems, especially those with itinerent electrons, frustration or a large degree of symmetry. In the remainder of this thesis we explore such systems and the recent progress.

Chapter 2

Intertwined Orders

Building on the perspectives presented in the introduction, we now discuss a model which explicitly demonstrates the precarious nature of manybody electronic systems. Specifically, we will show that a free fermion system with an *arbitrarily* weak repulsive interaction experiences a complete breakdown of its mean-field solutions, in stark contrast with the intuition we gained from Landau Fermi-Liquid theory. Moreover, we will demonstrate that the complexity of the emerging phase diagram is highly sensitive to perturbations — in some cases even realizing superconducting phases despite the repulsive nature of the bare interaction.

The work presented here considers an electronic system with a symmetry-protected band crossing point. Two-dimensional quadratic band crossing (QBC) systems, in which two parabolically dispersing bands meet at a single point in momentum space, have emerged as an attractive venue in which to study multi-criticality and competing orders.

At certain fillings, rather than a fermi-surface, such systems have a single fermi point in momentum space. In contrast to systems with Dirac points in two spatial dimensions, which are robust to weak short-range electron-electron interactions, analogously constructed QBC systems are prone to instabilities even at weak coupling: despite the point-like surface, the quadratic dispersion guarantees a finite DOS — and hence the possibility of critical fluctuations — in its vicinity. These instabilities become apparent by a simple scaling analysis: since the quadratic dispersion imbues electron fields with a scaling dimension of $d_\psi = 1/2$ ($z = 1$), all local two-body interactions are marginal.

As we will show, arbitrarily weak interactions in QBC systems protected by a high degree of symmetry can lead to a complex phase diagram consisting of many symmetry-broken phases. Furthermore, the leading emergent order can be missed by a mean-field analysis, which only probes the relative strengths of the various order parameters in the microscopic theory. This failure can be attributed to the fact that such a comparison between symmetry breaking orders represents a flat caricature of the otherwise rich phenomenology — it is misleading in the way that

We find that instead of a straightforward a nonlinear relationship between order parameter strengths at different scales. Even if the order parameter amplitudes are small in the microscopic theory, their *fluctuations* may couple channels in a nonlinear fashion. Integration of fluctuations down to the fermi-surface reveal that macroscopic order can be driven by short-range symmetry breaking across all channels simultaneously. Surprisingly, some exotic phases in this study only emerge in the presence of order parameters

that are otherwise *unrelated* to the macroscopic phase in question. The nonlinear interdependence of the strength of these fluctuations is best described as "intertwined" orders.

2.1 A QBC Hubbard model

As first demonstrated by Haldane [39], band crossing point carries quantized Berry flux as required by time-reversal symmetry. This flux is computed as a closed integral along a path in the Brillouin Zone (BZ), Γ, enclosing the band crossing point: $-i \oint_\Gamma d\mathbf{k} \cdot \langle \psi(\mathbf{k})|\boldsymbol{\nabla}_\mathbf{k}|\psi(\mathbf{k})\rangle = n\pi$, where the integral is computed over the appropriate band wavefunction $\psi(\mathbf{k})$ and n is an integer. For a Dirac point, the Berry flux is $\pm\pi$. Instead, the Berry flux at a QBC is either 0 or $\pm 2\pi$ [100]. A zero flux QBC is an accidental band crossing, which can be removed by infinitesimal band mixing without breaking any symmetries. In contrast, a QBC with $\pm 2\pi$ flux must be split into two Dirac points with equal $\pm\pi$ flux, and may therefore be protected from collapse by underlying symmetries.

Motivated by the unique properties of QBCs, and their susceptibility to instabilities, our goal is to construct a model with a crossing point that is robust to perturbations in the non-interacting theory. In general, there are two ways to remove a QBC: by splitting it into several Dirac points while preserving the total Berry flux or by breaking time-reversal (or similar) symmetry to open a gap. In the former case, consider that a QBC with flux 2π can be split into two separate Dirac points each with flux π, or three Dirac points with flux π and one additional Dirac point with $-\pi$. The first scheme breaks the

point group symmetry leaving, at most, a two-fold rotational symmetry unbroken. The latter case can take place while preserving a three-fold rotational symmetry, such as the case of bilayer graphene [73, 75]. For a QBCP with a fourfold or sixfold symmetry axis, the split into Dirac points cannot occur without breaking that symmetry. Thus, for a QBC (with Berry flux $\pm 2\pi$) to be stable without fine tuning, we require a model with C_4 or C_6 rotational symmetry in addition to preservation of time-reversal.

While there are numerous models that produce QBCs, we restrict our attention to the simplest possible toy model that captures the essential ingredients. We are interested in a 2D theory with a QBC which is protected — that may not be split into two Dirac points– and is invariant under time-reversal. Two simple lattices that have this property are the C_{v4} symmetric checkerboard lattice — a bipartite sum of two square lattices, describing numerous common materials including the copper-oxide planes of cuperate high-temperature superconductors (HtSC) — exhibiting a QBC at half filling and C_{v6} symmetric lattices such as the well-known 3-band kagomè lattice systems with a QBC at 1/3 filling.

Both models may be described by the same two-band Hamiltonian by interpolating the hopping parameters. We use the following low-energy effective Hamiltonian to describe such a QBC system : [101]

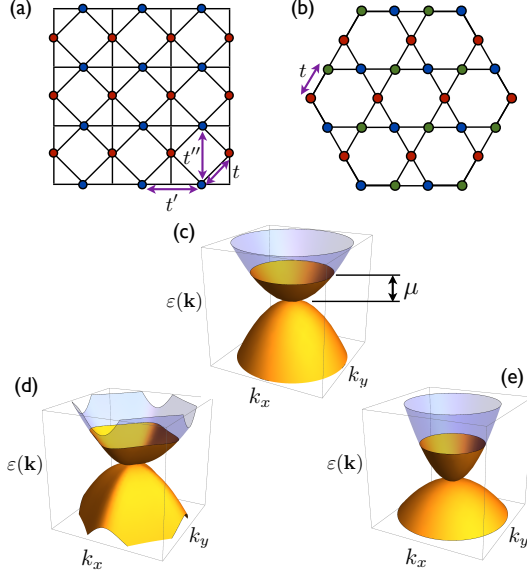$$H = H_0 + H_{int}, \tag{2.1}$$

where

Figure 2.1: (a) Checkerboard lattice, with nearest neighbor (t) and next-nearest neighbor (t', t'') hoppings shown. (b) Kagome lattice, with nearest neighbor hopping t. (c) Energy bands near a 2D quadratic band touching point in the rotationally invariant and particle-hole symmetric limit, with chemical potential μ. (d) For $\eta = 1.3\frac{\pi}{4} \neq \frac{\pi}{4}$, the dispersion has only 4-fold rotational symmetry. (e) For $\lambda = 0.4 \neq 0$, the bands become particle-hole asymmetric.

$$H_0 = \sum_{|\mathbf{k}|<\Lambda} \sum_{\alpha=\uparrow\downarrow} \psi_{\mathbf{k}\alpha}^\dagger \mathcal{H}_0(\mathbf{k}) \psi_{\mathbf{k}\alpha},$$

$$\mathcal{H}_0(\mathbf{k}) = t_I \mathbf{k}^2 1 + 2t_x k_x k_y \sigma_1 + t_z(k_x^2 - k_y^2)\sigma_3 \tag{2.2}$$

$$= \frac{\mathbf{k}^2}{\sqrt{2}m} \left[\lambda 1_2 + \sin\eta \sin 2\theta_{\mathbf{k}} \sigma_1 + \cos\eta \cos 2\theta_{\mathbf{k}} \sigma_3 \right],$$

where Λ is an ultraviolet momentum cutoff, σ_i are the usual Pauli matrices with $i = 0$ to be understood as the 2×2 identity, $1/\sqrt{2}m = \sqrt{t_x^2 + t_z^2}$, $\lambda = t_I/\sqrt{t_x^2 + t_z^2}$ describes particle-hole anisotropy, and $\tan\eta = t_x/t_z$ describes rotational anisotropy. The corresponding dispersion is

$$\varepsilon_\pm(\mathbf{k}) = \frac{\mathbf{k}^2}{2m} \left[\sqrt{2}\lambda \pm \sqrt{1 + \cos(2\eta)\cos(4\theta_{\mathbf{k}})} \right]. \tag{2.3}$$

For $|t_I| < \min(|t_x|, |t_z|)$, the model has two parabolic bands meeting at $\mathbf{k} = 0$, with

Interaction	g_0	g_1	g_2	g_3
Forward scattering (checkerboard or kagome)	g	0	0	0
Hubbard (checkerboard)	$\frac{1}{2}U$	0	0	$\frac{1}{2}U$
Hubbard (kagome)	$\frac{2}{3}U$	$\frac{1}{3}U$	0	$\frac{1}{3}U$

Table 2.1: Bare interactions $g_i(0)$ appearing in (2.4) for longer-range (forward scattering) and short-range (Hubbard) interactions, as determined by deriving the low-energy effective theory from a microscopic model on the checkerboard or kagome lattice.

one band dispersing upward and the other downward as one moves away from this point, as shown in Figure 2.1.

As written, the Hamiltonian (2.1) is invariant under the symmetries of the C_{4v} point group, and may arise as a low-energy effective theory for electrons on the checkerboard lattice at half filling, with the parameters in (2.2) related to the lattice hopping parameters shown in Figure 2.1 as $t_x = t/2$, $t_z = (t' - t'')/2$, and $t_I = (t' + t'')/2$.[101] It can also describe a system having C_{6v} symmetry if one takes $t_x = t_z = t$ and $g_1 = g_3$. In this case the low-energy theory has full rotational symmetry, since any other possible terms consistent with six-fold rotational symmetry would contain higher powers of momentum and hence would be irrelevant. Such an effective theory may arise from electrons on a kagome lattice at $\frac{2}{3}$ filling[101]. In either case, the QBC point is robust to perturbations which do not break time reversal or point group symmetries. In the absence of external symmetry-breaking fields, only a spontaneous symmetry-breaking instability to an ordered phase can alter the QBC point. The group representations for the C_{4v} and C_{6v} cases together with the corresponding symmetry-allowed interaction terms are shown in Table 2.2.

2.1.1 Previous Analyses

As mentioned, previous studies have detailed the phase diagram of this model using various approaches. In the work of Sun et. al., [101] a mean field analysis was applied to investigate both spinless and spin-1/2 fermion systems.

In the spinless case, a Hamiltonian of the form of Eq. 2.2 was studied, considering only a nearest neighbor interaction term between distinct lattice sites $H_{int} \sim g \int d^2x |\psi^\dagger(x)\sigma^x\psi(x)|^2$. A scaling argument demonstrates that such an interaction represents a marginally relevant perturbation for any finite repulsive coupling. To investigate the leading order in the resultant strong coupling theory, they constructed order parameters for the three possible symmetry broken phases: the QAH which breaks $\mathcal{T}$ and two nematic parameters which break lattice symmetry down to C_2 by splitting the QBC into two Dirac points with equivalent flux. The strength of these order parameters were then compared in the weak coupling microscopic theory. They found that in the case of spinless fermions, a Quantum anomalous hall phase with topologically protected edge states was the dominant instability at weak coupling, with a crossover into a nematic phase at intermediate strengths.

In the spin-1/2 model described by Eq. 2.2, they considered contributions from the four shortest-range interactions: a) an on-site repulsive Hubbard U, b) a nearest neighbor repulsion V, c) a nearest neighbor exchange interaction J, and d) a pair-hopping term W. These correspond to linear combinations of our couplings as given by Table 2.1. The evaluation of these perturbations lead to six marginally-relevant terms by scaling. In

the mean-field limit, the phase diagram obtained for the parameter regime $U > V > 0$ at $T = 0$: For $U > 2V > 0$, the system is in the NSN phase at low temperatures for $2V > U > 0$; the QAH phase for $J > 0$; the QSH phase for $J < 0$. For $U \to \infty$ (and $J = 0$), there is a NSN state, while $V \to \infty$ stabilizes a nematic phase.

Another study by Uebelacker and Honerkamp [105] used a functional renormalization (fRG) approach to study the QBC system of Eq. 2.2. In an fRG approach, numerical evaluation of the flow is accomplished by assuming that the quadratic part of the action is dependent upon a cutoff parameter, such that the propagator is restricted to acting within the high-energy Hilbert space. Perturbative corrections are then computed and summed from some UV cutoff Λ_0 down to the desired scale low-energy scale Λ. The emergence of a strong coupling phase is indicated by a divergence at some critical scale $\Lambda_c > \Lambda$, and a comparison of Λ_c between interactions reveals the leading instability of the system. Using this method, they similarly found NSN as the leading instability.

2.2   A Renormalization Group Approach

An analysis based on a mean-field calculations may not be reliable in cases where there are competing instabilities with diverging susceptibilities in multiple channels. As we will demonstrate in the next sections, the existence of multiple orders can lead to surprising nonlinear effects: fluctuations in one channel, even if it is not the leading order, may couple to the flow of another, altering the IR behavior and even changing the sign of the interaction.

In order to simplify the approach, we will focus our efforts on the simplest parameter choice in Eq. 2.2 , following the work published by two of us previously [72]. Analysis of the generalized model may be found in the Appendix A. We choose the rotationally invariant and particle-hole symmetric limit, where $\eta = \pi/4$ and $\lambda = 0$. The band structure takes the simple form $\epsilon(\vec{k}) = \pm\frac{k^2}{2m}$. The interaction term appearing in (2.1) is defined to be

$$H_{\text{int}} = \frac{2\pi}{m} \sum_{i=0}^{3} g_i \int d^2x \left(\sum_{\alpha=\uparrow\downarrow} \psi_\alpha^\dagger(\mathbf{x})\sigma_i\psi_\alpha(\mathbf{x}) \right)^2, \tag{2.4}$$

which contains all marginal symmetry-allowed couplings. The low-energy effective Hamiltonian used to describe the system is given by $H = H_0 + H_{\text{int}}$, where the non-interacting part introduced by Sun et $al.$ is given by [101] We employ a Wilsonian RG procedure [106, 108, 107] in order to study the effects of interactions and instabilities to ordered phases at low energy scales. It is useful to define the following action:

$$S = \int d\tau \left[\sum_{|\mathbf{k}|<\Lambda} \sum_\sigma \psi_{\mathbf{k}\sigma}^\dagger (\partial_\tau + \mathcal{H}_0(\mathbf{k}))\psi_{\mathbf{k}\sigma} + H_{\text{int}} \right], \tag{2.5}$$

where the Grassmann fields $\psi_{\mathbf{k}\sigma}$ now depend on imaginary time τ. The RG step is then performed by eliminating states within the momentum shell $\Lambda(1 - d\ell) < |\mathbf{k}| < \Lambda$ while integrating over all frequencies. By including all one-loop diagrams and rescaling the couplings after each RG step, one obtains the following flow equations:

32

$$\frac{dg_i}{d\ell} = \sum_{j,k=0}^{3} A_{ijk} g_j g_k. \tag{2.6}$$

These coefficients, A_{ijk}, are calculated from the five 1-loop diagrams that contribute at second-order, and are explicitly given in Appendix A. It can be shown that the parameters λ and η do not flow at this order, preserving the topology and symmetry of the bands. From (2.6), one sees that the couplings are marginally relevant and generally flow to infinite values for sufficiently large ℓ. The *ratios* of these couplings, however, approach fixed finite values, with each of these fixed ratios corresponding to a particular ordered phase. Due to the perturbative nature of this approach, the flow equations remain valid only at weak coupling and break down at RG scales where $g_i(\ell) \gtrsim 1$.

It is convenient to define a set of new couplings by a linear transformation in the valley-singlet channels: $g_{\pm} = (g_3 \pm g_1)/2$. Remaining in the limit of a rotationally invariant ($\eta = \pi/4$), particle-hole symmetric ($\lambda = 0$) system, the flow equations (2.6) in this new basis take on the following relatively simple form:

$$
\begin{aligned}
\dot{g}_0 &= -4g_0 g_+ \\
\dot{g}_+ &= -(g_0 - g_+)^2 - (g_2 - g_+)^2 - 6g_+^2 \\
\dot{g}_2 &= 4(g_0 g_2 - g_2^2 - g_-^2 + g_+^2 - 3g_2 g_+) \\
\dot{g}_- &= 2g_-(g_0 - 3g_2 - 2g_+).
\end{aligned}
\tag{2.7}
$$

From this equation we see that g_- will not be generated if it vanishes initially, which indeed must be the case when the system has C_6 rotational symmetry. One also sees from (2.7) that $\dot{g}_+ \leq 0$, indicating that $g_+(\ell)$ decreases under RG flow. Apart from certain fine-tuned initial conditions from which the coupling ratios flow toward one of
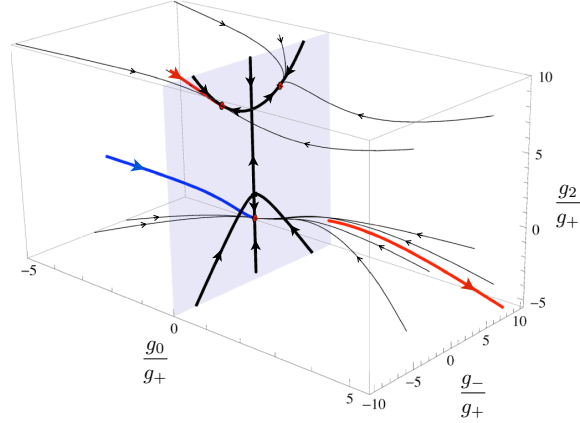
Figure 2.2: Renormalization group flows of the coupling ratios, with $g_\pm = (g_3 \pm g_1)/2$, with fermion dispersion taken to be rotationally invariant ($\eta = \pi/4$) and particle-hole symmetric ($\lambda = 0$). The three stable fixed ratios are shown in red, with the upper two corresponding to a QAH phase, while the stable fixed ratio with $g_2/g_+ < 0$ corresponds to a QSH phase. The trajectories corresponding to Hubbard and forward scattering interaction are shown as bold red and blue lines, respectively. In the Hubbard case, the flow begins with $g_0/g_+ > 0$ and then reappears in the opposite quadrant when $g_+(\ell)$ passes through zero. Apart from the unstable Gaussian fixed point, all flows terminate in the $g_0/g_+ = 0$ plane as $g_+ \to -\infty$. For the black arrows, the flow direction corresponds to $g_+ < 0$. If $g_+ > 0$ initially, the couplings first flow opposite to the direction shown (as shown for the Hubbard case) until g_+ changes sign and the trajectories follow the arrows shown.

the mixed-stability fixed ratios in the $g_0 = 0$ plane shown in Figure 2.2, one finds in all cases that $g_+(\ell)$ passes through 0 and eventually flows toward large negative values. AS done in Ref. [108], using the monotonic decrease of $g_+(\ell)$ allows one to reparameterize the flow equations in terms of the flow of this coupling, so that the new flow equations are of the form $d(g_i/g_+)/dg_+ = \Phi_i(\{g_j/g_+\})$.

As shown in Figure 2.2, which illustrates the RG flows of the reparametrized coupling ratios, there are three stable fixed values. All of the fixed ratios lie in the plane $g_0/g_+ = 0$. In order to identify these phases, one can analyze the susceptibilities of various symmetry-braking order parameters by introducing the following source terms into the action:

Rep. (C_{4v})	g_i	$M_i^{(c)}$	Phase (c)	$M_i^{(s)}$	Phase (s)	$M_i^{(pp)}$	$\tilde{g}_i$	Phase (pp)
A_1	g_0	1_4	–	$1\vec{s}$	FM	$1s_2$	$\tilde{g}_0$	s
A_2	g_2	$\sigma_2 1$	QAH	$\sigma_2 \vec{s}$	QSH	$\sigma_2(is_2\vec{s})$	$\tilde{g}_2$	p
B_1	g_3	$\sigma_3 1$	Nem. (site)	$\sigma_3 \vec{s}$	NSN (site)	$\sigma_3 s_2$	$\tilde{g}_3$	$d_{x^2-y^2}$
B_2	g_1	$\sigma_1 1$	Nem. (bond)	$\sigma_1 \vec{s}$	NSN (bond)	$\sigma_1 s_2$	$\tilde{g}_1$	d_{xy}
Rep. (C_{6v})								
A_1	g_0	1_4	–	$1\vec{s}$	FM	$1s_2$	$\tilde{g}_0$	s
A_2	g_2	$\sigma_2 1$	QAH	$\sigma_2 \vec{s}$	QSH	$\sigma_2(is_2\vec{s})$	$\tilde{g}_2$	p
E_2	(g_1, g_3)	$(\sigma_3 1, \sigma_1 1)$	Nem.	$(\sigma_3 \vec{s}, \sigma_1 \vec{s})$	NSN	$(\sigma_3 s_2, \sigma_1 s_2)$	$(\tilde{g}_3, \tilde{g}_1)$	$(d_{x^2-y^2}, d_{xy})$

Table 2.2: Fermionic couplings g_i, together with the representation of C_{4v} or C_{6v} under which they transform, the matrices appearing in the source term bilinears (2.8), and the phases associated with each bilinear. The possible excitonic phases are ferromagnet (FM), quantum anomalous Hall (QAH), quantum spin Hall (QSH), charge nematic on sites or bonds, and nematic-spin-nematic (NSN) on sites or bonds. The last three columns show the matrices appearing in the particle-particle bilinears in (2.8), the transformed couplings from (2.13), and the corresponding superconducting phases (s-wave, p-wave, and d-wave). In the left most columns the pair couplings $\tilde{g}_i$ are given with their corresponding superconducting phases.

$$S_\Delta = \int d\tau \int d^2x \left\{ \sum_{i=1}^{4} \left[\Delta_i^{(c)} \psi^\dagger M_i^{(c)} \psi + \vec{\Delta}_i^{(s)} \cdot \psi^\dagger \mathbf{M}_i^{(s)} \psi \right] \right.$$
$$\left. + \frac{1}{2} \left[\sum_{i=1}^{3} \Delta_i^{(pp)} \psi^\dagger M_i^{(pp)} \psi^* + \vec{\Delta}_4^{(pp)} \cdot \psi^\dagger \mathbf{M}_4^{(pp)} \psi^* + H.c. \right] \right\}. \tag{2.8}$$

The matrices that define the various fermion bilinears in charge (c), spin (s), and particle-particle (pp) channels are given in Table 2.2.

The source terms in (2.8) flow under RG as follows:

$$\frac{d \ln \Delta_i^{(c,s,pp)}}{d\ell} = 2 + \sum_{j=0}^{3} B_{ij}^{(c,s,pp)} g_j, \tag{2.9}$$

where the coefficients $B_{ij}^{c,s,pp}$ are provided in the SI. It is then possible to compute susceptibilities by taking derivatives of the free energy with respect to these source terms: $\chi_i = -\partial^2 f / \partial \Delta_i \partial \Delta_i^*$. The full expressions for χ_i are given in the SI. One finds that they exhibit power law behavior near the RG scale ℓ_* where the couplings $g_i(\ell)$ diverge, i.e. $\chi_i \sim (\ell_* - \ell)^{-\lambda}$. These exponents are given by
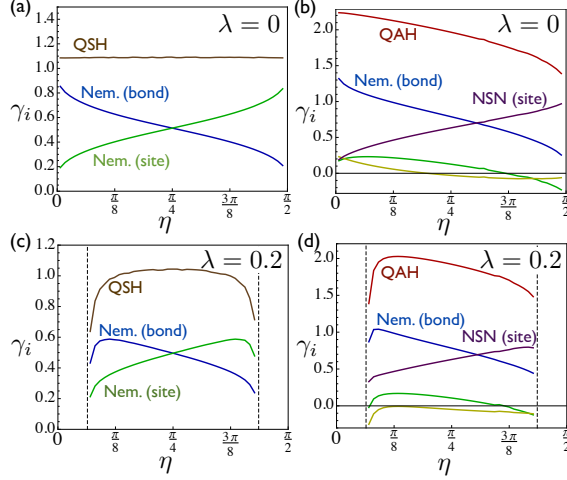
Figure 2.3: Critical exponents of divergent susceptibilities as a function of anisotropy ($\eta = \pi/4$ corresponds to the rotationally invariant case). Left panels correspond to long-ranged interaction ($g_0(0) > 0$ only); right panels correspond to Hubbard interaction ($g_0(0) = g_3(0) > 0$). Upper panels are calculated with particle-hole symmetry; lower panels are calculated with particle-hole asymmetry $\lambda \neq 0$.

$$\gamma_m^{(c,s,pp)} = \frac{2\sum_j B_{mn}^{(c,s,pp)} \rho_n}{\sum_{ijk} A_{ijk}\rho_i\rho_j\rho_k}, \tag{2.10}$$

where $\rho_i = \lim_{\ell \to \ell_*} g_i(\ell)/\sqrt{\sum_j g_j^2(\ell)}$. The susceptibility exponents are shown for various

values of rotational anisotropy and particle-hole asymmetry in Figure 2.3. In the case

of long-ranged interaction, one can see from the figures that QSH is the leading insta-

bility, with subleading instabilities to charge nematic phases. For Hubbard interaction,

the leading instability is to the QAH phase, with subleading instabilities to either charge

nematic along bonds or nematic spin nematic (NSN) on sites. The susceptibilities them-

selves for both types of interaction are shown in the Appendix, from which we see that

the results for the leading instabilities match those from Figure 2.3.

Ultimately, this procedure reveals that two of the three stable fixed points correspond

to the QAH phase, while the third corresponds to QSH. We thus conclude that *all* possible

instabilities of the system at weak coupling are to *topologically ordered phases*, and that these instabilities are realized for arbitrarily weak values of the couplings g_i.

For density-density interactions, the only nonzero bare couplings are g_0 and g_3, with the other couplings generated upon running the RG. For on-site Hubbard interaction on the checkerboard lattice, $g_0(\ell = 0) = g_3(\ell = 0)$, while for the case of long-ranged forward scattering interaction, only g_0 is nonzero initially. The spatial range of the interaction can then be adjusted by interpolating between these two limits. For all sufficiently short-ranged interactions satisfying $g_3(0)/g_0(0) > 0.26$, the couplings flow to the fixed ratios at $(g_0, g_-, g_2) = (0, -3.73, 7.46)g_+$, corresponding to the QAH phase. For $g_3(\ell = 0)/g_0(\ell = 0) < 0.26$, on the other hand, the couplings flow to $(g_0, g_-, g_2) = (0, 0, -1.09)g_+$, corresponding to QSH. Although we have focused on the symmetric case with $\eta = \pi/4$ and $\lambda = 0$, the results remain qualitatively similar away from the particle-hole symmetric and rotationally invariant limit.

2.2.1 Fluctuation Driven Intertwined Orders

The following point is stressed: The realization of the QAH phase depends crucially on the coupling g_2 that is *generated by fluctuations* — these fluctuations are clearly captured in the RG approach, but sorely missing in the mean-field analysis. As such, the realization of the QAH phase for the Hubbard interaction is in apparent contrast with the previously discussed results of Refs. [101] and [105], both of which found NSN as the leading instability. The NSN phase preserves rotational symmetry in the charge channel

while breaking it in the spin channel [76]. The analysis of Ref. [101] was based on a mean-field analysis, which may not be reliable in cases where there are competing instabilities with diverging susceptibilities in multiple channels. Indeed, since the Hubbard interaction does not couple neighboring sites on opposite sublattices, it is clear that the QAH order parameter $\langle \psi^\dagger (\sigma_2 1) \psi \rangle$ will not be favored at mean-field level.

On the other hand, while the fRG study of Ref. [105] does include such fluctuations, that method is restricted to strong or intermediate couplings $U \gtrsim t$, and so complements the analysis of weak-coupling instabilities. That a NSN phase is realized at strong coupling is not surprising, as this corresponds to a Ne$\vec{e}$l state in which spins anti-align with their nearest neighbors. Such a state is not favored at weak coupling, however, due to its gapless excitation spectrum, which can be expected to gain less condensation energy than the fully gapped QAH phase. As pointed out previously [101], in the charge (spin) nematic phases, the quadratic band touching splits into two (four) Dirac cones, so that the excitation spectrum remains gapless in each of these cases. As the magnitude of the order parameter grows, these cones move further apart. In a theory that takes the full lattice into account, the cones eventually annihilate far from the original band touching points, and the spectrum becomes fully gapped for sufficiently strong interactions. At weak coupling, however, this cannot occur, and one expects the fully gapped spectra of the QAH or QSH phases to be favored in this case, which is indeed what is found.

2.3   Emergent order in Doped QBCs

We now extend these results [72] by investigating the single-valley QBC system away from half filling, showing that d-wave and conventional s-wave superconducting order can be realized at nonzero doping for repulsive short-range and longer-range interactions, respectively. The contents of this section closely follow our 2014 publication [78].

We return to the normalization analysis under the flow of Eqn. 2.5 , where we now include a finite chemical potential by the substitution $\mathcal{H}_0 \to \mathcal{H}_0 - \mu$. The chemical potential scales as $\mu \to \mu e^{2\ell}$ at T=0 [107, 71]. Again, one sees that the couplings are marginally relevant and generally flow to infinite values for sufficiently large ℓ, though their ratios approach fixed finite value. A reevaluation of our diagrams reveal that, away from half-filling, only particle-particle scattering leads to chemical potential dependence in the flow equations. This is somewhat intuitive — the effect of chemical potential on our system is to modulate the *density*, so one would expect that the particle-particle scattering channel should be sensitive to its presence at 2nd order. Moreover, reconstructing the flow coefficients of 2.6 for the finite μ case, the new contribution only appears in the particle-hole fluctuation, corresponding to coefficients A^5:

$$A_{ijk}^5(\mu_\ell) = \left(\frac{1}{1 - \mu_\ell^2} \right) A_{ijk}^5(0), \tag{2.11}$$

where we have defined $\mu_\ell \equiv \mu e^{2\ell} / \frac{\Lambda^2}{2m} = \hat{\mu} e^{2\ell}$. This can be understood by consider-

ing that a renormalized particle-particle interaction rate naturally leads to a change in particle-hole densities, since these events scatter fermions near the fermi-surface.

Using the new coefficients, we may rewrite the flow equations such that the μ-dependent terms are separate, in order to make use of the previously established results:

$$\frac{dg_i}{d\ell} = \sum_{j,k=0}^{3} \left(A_{ijk}(0) + \left(\frac{\mu_\ell^2}{1-\mu_\ell^2}\right) A_{ijk}^5(0) \right) g_j g_k$$
$$= \dot{g}_i(\ell, \mu = 0) + \left(\frac{\mu_\ell^2}{1-\mu_\ell^2}\right) \sum_{j,k=0}^{3} A_{ijk}^5(0) g_j g_k.$$

(2.12)

Further insight can be gained by using the so-called Fierz identities [107] to recast the interaction term as a combination of pairing interactions of the general form

$$S_{int} = \int d\tau \int d^2 r \left[\sum_{j=\text{singlet}} \tilde{g}_j S_j^\dagger S_j + \sum_{j=\text{triplet}} \tilde{g}_j \vec{T}_j^\dagger \cdot \vec{T}_j \right],$$

(2.13)

where

$$S_j = \psi^T(\mathbf{r}, \tau) \sigma_j s_2 \psi(\mathbf{r}, \tau), \quad \text{for } j = 0, 1, 3$$
$$\vec{T}_j = \psi^T(\mathbf{r}, \tau) \sigma_2 \vec{s} \psi(\mathbf{r}, \tau), \quad \text{for } j = 2.$$

(2.14)

Here $\vec{s}$ is a vector of Pauli matrices corresponding to electron spin. Recasting the problem in this equivalent way and making use of the Fierz identities gives us the following relation among the ordinary and Cooper gauge couplings:

$$\tilde{g}_i(\ell, \mu) = \sum_j \mathcal{F}_{ij} g_j(\ell, \mu)$$

(2.15)

where the Fierz matrix $\mathcal{F}$ is

$$\mathcal{F} \equiv \frac{1}{4} \begin{pmatrix} 1 & 1 & -1 & 1 \\ 1 & 1 & 1 & -1 \\ 1 & -1 & -1 & -1 \\ 1 & -1 & 1 & 1 \end{pmatrix} \tag{2.16}$$

The importance of this transformation is that the flow equations are written in a way that clearly separates μ dependence

$$\frac{d\tilde{g}_i}{d\ell} = -\frac{\alpha_i}{1 - \mu_\ell^2} \tilde{g}_i^{\,2} + \sum_{j,k} \tilde{A}_{ijk} \tilde{g}_j, \tilde{g}_k \tag{2.17}$$

where $\alpha_i \geq 0$, and the coefficients $\tilde{A}_{ijk}$ are non-singular as $\mu_\ell \to 1$.

2.3.1 Flow equation solutions in the Isotropic Limit

Again, analyzing the flow equations in the simplest case of particle-hole symmetry ($\lambda = 0$) and rotational invariance ($\eta = \frac{\pi}{4}$), the coupled equations (2.12) are given by 2.7 as previously shown. In the case of C_{6v} symmetry, we have $g_- = 0$, reducing the system to one with only three couplings. The μ-dependent contributions to the flow equations

41

come from the last term in (2.12) and are given by

$$\sum_{j,k=0}^{3} A_{0jk}^5(0)g_j g_k$$
$$= g_0^2 + g_2^2 + 2\left(g_+^2 + g_-^2 + g_+(g_0 - g_2)\right),$$
$$\sum_{j,k=0}^{3} \frac{1}{2}[A_{3jk}^5(0) + A_{1jk}^5(0)]g_j g_k = (g_0 - g_2 + 2g_+)^2,$$
$$\sum_{j,k=0}^{3} A_{2jk}^5(0)g_j g_k = 2\left(g_-^2 + (g_2 - g_+)(g_0 + g_+)\right),$$
$$\sum_{j,k=0}^{3} \frac{1}{2}[A_{3jk}^5(0) - A_{1jk}^5(0)]g_j g_k = 4g_-(g_0 + g_2).$$

(2.18)

It is straightforward to obtain the flows of the transformed couplings $\tilde{g}_i(\ell)$ using the

transformation (2.15). In Figure 2.6 we show the flow of the superconducting Fierzed

couplings $\tilde{g}_i$ as plotted parametrically against a variable t defined as [107]

$$t = \frac{1}{2} \ln\left(\frac{1 - \hat{\mu}}{e^{-2\ell} - \hat{\mu}}\right),$$

(2.19)

which vanishes at $\ell = 0$ and increases without bound as the Fermi surface is approached,

thus better showing the behavior of the quickly diverging coupling flows as $\ell \to \ell_{FS}$. At

half filling, the couplings diverge to both positive and negative values, as shown in Figure

2.6.

Including a nonzero chemical potential gives an advantage to the attractive couplings,

as is apparent from (2.17), so that these diverge while the repulsive couplings saturate as

the UV cutoff approaches the Fermi level. For forward scattering, in which case all initial

couplings $\tilde{g}_i(0)$ are positive, running RG with optimal chemical potential and coupling

strength causes the Fierz coupling associated with conventional s-wave SC to diverge to large negative values. In the case of the short-range Hubbard interaction two Fierz couplings start out at zero – one of which, corresponding to a d_{xy} SC state, diverges to large negative values under RG.

As shown in Figure 2.4, the instabilities at and near half-filling [72] are to quantum anomalous Hall[38, 13] (QAH) and quantum spin Hall[47, 5, 52] (QSH) phases, both of which are topological in nature and feature charge or spin edge currents. (In the QSH case, edge spin currents will not in general be conserved in the presence of disorder.) For larger μ, the only susceptibilities that show divergent behavior for sufficiently large μ are those in the particle-particle channels, and in this case s-wave and d-wave superconducting phases are the leading instabilities of the doped system. The appearance of s-wave superconductivity driven by repulsive interaction is unusual, and comes about in this case due to the fact that (i) all couplings $\tilde{g}_i(0)$ are initially equal for longer-range interactions, so that no channel is initially disfavored; and (ii) the s-wave phase is fully gapped, making it favorable due to the increased gain in condensation energy. This is analogous to the pair density wave (PDW) instability previously found for repulsively interacting electrons on the honeycomb lattice.[107, 71] The PDW is also fully gapped, though in that case the Cooper pairs have nonzero total momentum $2\mathbf{K}$ due to the fact that pairing occurs within a Fermi pocket centered at wavevector $\mathbf{K}$.
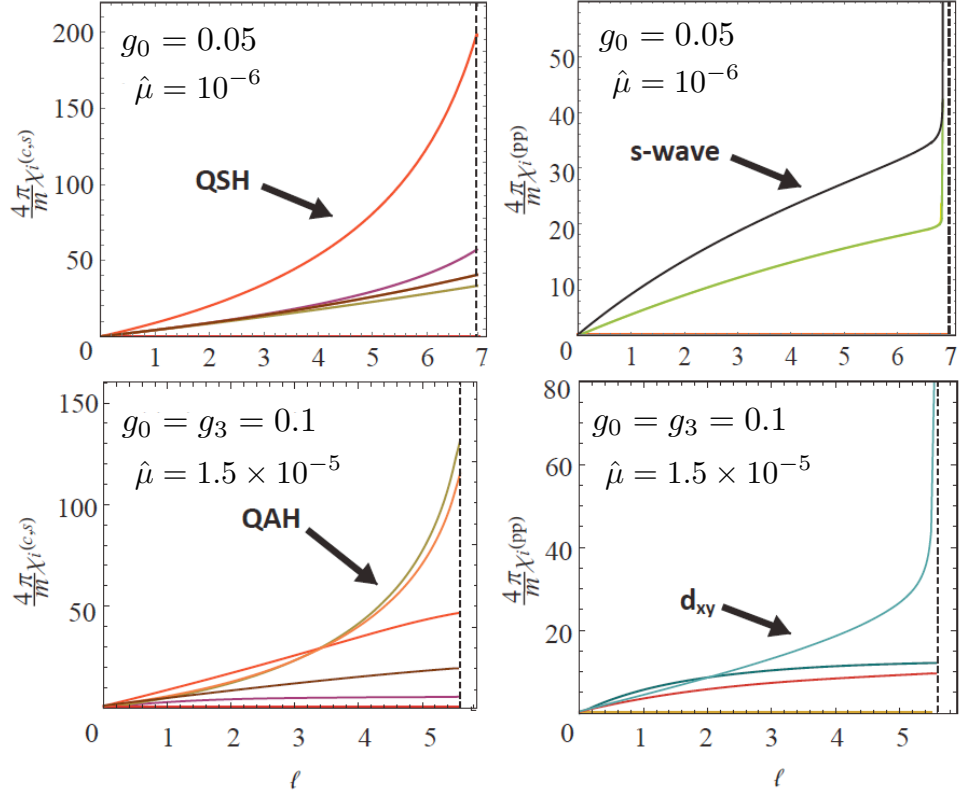
Figure 2.4: RG flows of susceptibilities for various instabilities in particle-hole and particle-particle channels with finite chemical potential. Top row: With forward scattering interaction, susceptibilities in spin and charge channels saturate at finite values (left), while the susceptibility in the s-wave particle-particle channel diverges (right). Bottom row: With Hubbard interaction (on the checkerboard lattice), susceptibilities in spin and charge channels saturate at finite values (left), while the susceptibility in the d-wave particle-particle channel diverges (right).
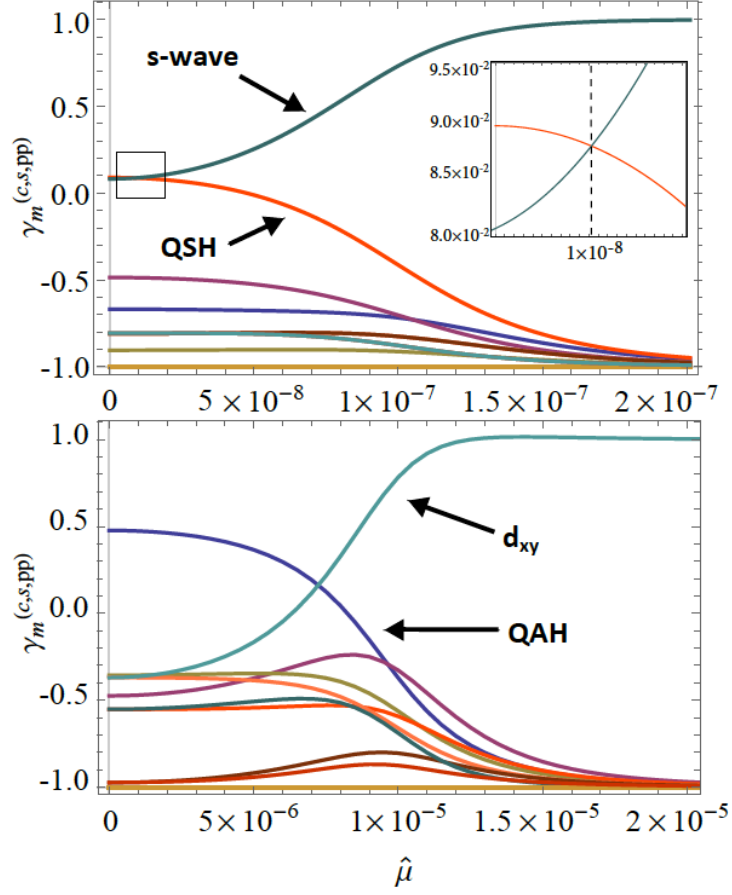
Figure 2.5: Variation of the susceptibility exponent $\gamma_m^{(c,s,pp)}$ with increasing dimensionless chemical potential $\hat{\mu}$. Moving away from half-filling causes the susceptibilities of the leading particle-hole instabilities to saturate, while those of the particle-hole channels diverge. Top: forward scattering interaction, with $g_0(0) = 0.05$ and $g_{1,2,3}(0) = 0$. Bottom: Hubbard interaction (on checkerboard lattice), with $g_0(0) = g_3(0) = 0.1$ and $g_1(0) = g_2(0) = 0$.

2.3.2 Proof of Guaranteed Superconductivity

It is apparent that for $\mu_\ell \approx 1$ the equations will become essentially decoupled. In this regime, if a pair coupling is attractive, it will diverge to negative infinity while the repulsive couplings saturate. Following the arguments given in Ref. [107], one can show that for arbitrarily weak couplings an appropriate $\hat{\mu}$ can always be chosen to accomplish this. First consider the case at half filling: at some ℓ_1 one of the couplings becomes attractive. This behavior is approximately preserved as one moves away from half filling so long as $\mu_{\ell_1} \ll 1$. On the other hand, we need to choose $\hat{\mu}$ sufficiently large such that the attractive coupling diverges at ℓ_{FS} defined by $\mu_{\ell_{FS}} = 1$ while saturating the repulsive couplings. If at half-filling, the repulsive couplings diverge at ℓ_*, then having $\mu_{\ell_{FS}} \ll \mu_{\ell_*}$ would satisfy this. Combining these conditions produces the following inequality:

$$\frac{\Lambda^2}{2m}e^{-2\ell_*} \ll \mu \ll \frac{\Lambda^2}{2m}e^{-2\ell_1}. \tag{2.20}$$

In order to show that this relationship may always be satisfied, we defer to the following argument. Consider that the $\mu = 0$ flow equations are invariant under the following transformation:

$$g_i \to bg_i, \quad \ell \to \ell/b. \tag{2.21}$$

Then we can say that there are constants C_1 and C_* such that $\ell_1 = C_1/g$ and $\ell_* = C_*/g$,
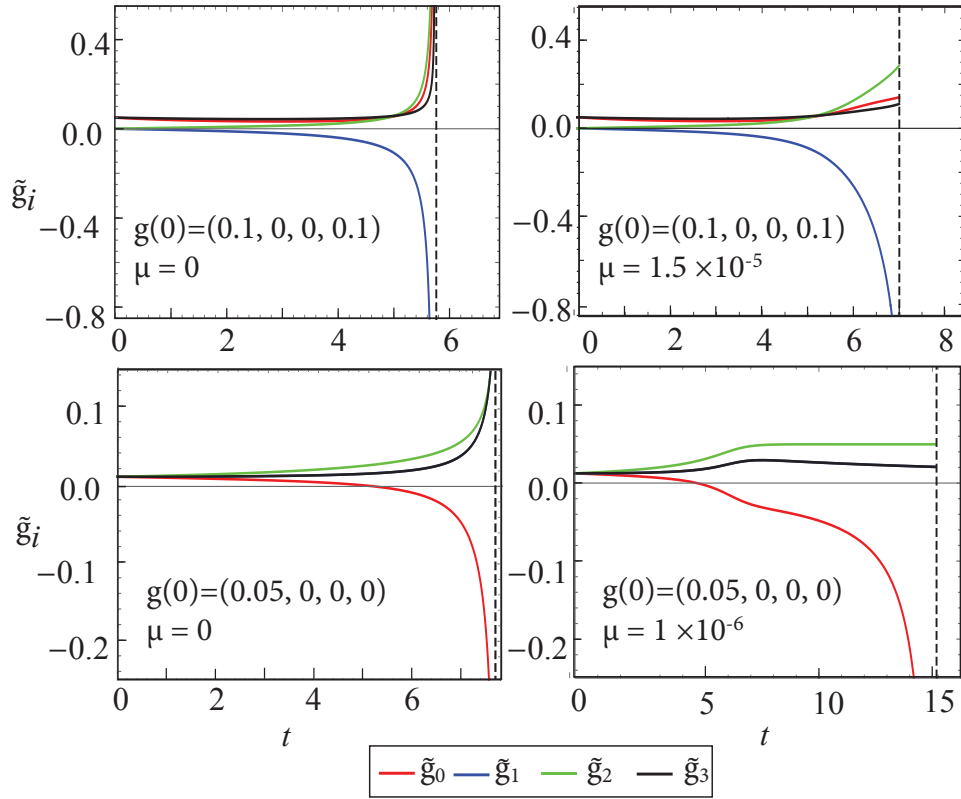
Figure 2.6: Top row: Flows of couplings for Hubbard interaction (on the checkerboard lattice), with $\hat{\mu} = 0$ (left), and $\hat{\mu} = 1.5 \times 10^{-5}$ (right). Bottom row: RG flows of couplings at half filling for forward scattering interaction with $\hat{\mu} = 0$ (left) and at $\hat{\mu} = 10^{-6}$ (right). In both cases, a sufficiently large chemical potential for a given interaction strength causes all repulsive couplings to saturate, while attractive couplings diverge.

for $g \equiv \sqrt{\sum_i g_i^2(0)}$. Therefore, we have that

$$\frac{\Lambda^2}{2m} e^{-2\frac{C_*}{g}} \ll \mu \ll \frac{\Lambda^2}{2m} e^{-2\frac{C_1}{g}} \tag{2.22}$$

It is clear that as long as the couplings can be arbitrarily weak, the relationship can be satisfied. We use the above relation to determine the coupling strength and Fermi level appropriate to obtain a superconducting phase. For example, in the case of forward scattering at half filling, we find that $C_1 \approx 0.26$ and $C_* \approx 0.40$ (see Figure 2.6). Choosing the coupling to be $g_0(0) = 0.05$, we find that $\hat{\mu} = 10^{-6}$ entirely satisfies our constraint (2.22).

2.4   Conclusions

While the appearance of superconductivity adjacent to various forms of particle-hole order has been observed in many families of strongly correlated materials, the precise mechanism for such behavior is still a matter of controversy. The fact that such phases tend to appear together appears to be at odds with the naive expectations of mean-field theory, from which one would expect such phases to compete, so that what is good for superconductivity is bad for particle-hole order and vice versa. The results of the preceding section suggest that these phases may be more usefully thought of as "intertwined" rather than competing,[29] as it is the enhanced logarithmic RG flows due to the fluctuations in particle-hole channels that ultimately lead to superconductivity. Of

particular interest in the single-valley QBC model studied here is the unusual appearance of s-wave superconductivity driven by repulsive interactions, as well as the appearance of superconductivity adjacent to topological phases of matter, as shown in Figures 2.5 and A.5. Our work raises the possibility that there may exist a quantum critical point separating these phases, although one cannot rule out the possibility of, *e.g.*, a first-order phase transition using the present approach. More broadly, the QBC model studied here thus provides a relatively simple and well-controlled arena in which to better understand the behavior of intertwined orders in 2D.

Chapter 3

Strongly Correlated Phases

Strongly correlated electron systems can result in macroscopic behavior that deviates from a conventional fermi-liquids (FL). As discussed in the introduction, FLs are defined by the nature of their low-lying excitations — while single electron-hole pairs may no longer account for these states in the presence of interactions, there exists an adiabatic transformation into quasi-particle states that preserve the fundamental description of a Fermi-gas, up to a "redressing" of parameters.

Most importantly, these quasi-particles are long-lived ($\tau \sim \frac{E_F}{T^2}$) particle-like excitations that retain a sharp spectrum in the vicinity of the fermi-surface— the qualitative structure of the system's density of states is locally conserved, permitting the application of perturbative approaches. This means that these quasi-particles, when describing a real material system, will have a the canonical properties of ordinary metals, including: T^2 temperature dependence on resistivity at low temperatures, a linear T relationship

with heat capacity and B^2 magneto resistance scaling. However, in certain systems — including many novel materials of interest and High Temperature Super Conductors— this ceases to be true: interactions lead to the complete destruction of the original fermi-surface, replacing the sharp particle-like spectrum with a broad distribution of energy levels that indicate a the presence of relevant complex, combinatorially terse, multi-particle interactions.

Compared with more common fermionic phases, little is know about these so-called Non-Fermi Liquid (NFL) phases, which frequently occur at quantum critical points of itinerant electron systems [40, 68, 60]. The strong correlations and quantum critical fluc-tuation often make it challenging to study the non-fermi liquids through the standard diagrammatic approach, and various expansion methods have been developed for that purpose [55, 70, 65, 66, 19]. Despite this, there have been few tractable models exhibit-ing the NFL phase. Barring Luttinger liquids, whose 1D phase transitions and ground states cannot be generalized to higher dimensions, there have been few widely accepted, generalizable results pertaining to these systems.

In this chapter we will discuss new results on the NFL phase, which followed a dra-matic resurgence of the so-called "SYK model" (Sachdev-Ye-Kitaev Model) in 2015. Originally posed by Sachdev and Ye in 1993 [86], the $(0 + 1)d$ model is characterized by a random all-to-all SU(N) Heisenberg interaction and a solvable low-energy theory described by the NFL phase. This model was later reintroduced by Kitaev [43] in 2015 using a majorana fermion model, conjectured to be platform for understanding holo-

graphic duality.

Perhaps more important that characterizations of the NFL phase alone, are its instabilities and phase transitions to more conventional orders. Given the vast number of real material systems who's low energy phases are expected to be described by NFL physics, a full understanding of the fermionic phase diagram in the vicinity of an NFL is of critical importance. To this goal, the work reviewed in this chapter presents the first known instabilities of a NFL. Surprisingly, the destabilizing interactions investigated have a superficial appearance to superconducting pair instabilities, deepening the nearly 100 year old mystery the quantum critical regime in High Temperature Superconductors.

3.1 From Random Magnetism in Alloys To Black Holes

The origin of the SYK model can be traced back to the theory of spin glasses which emerged in the 1970's– a time when many physicists were pondering the properties of metal alloys, such as Cu/Mg and Au/Fe. These alloys displayed competing ferro- and antiferro-magnetic interactions, leading to irregular spin alignments beyond the reach of the standard Ising paradigm. In 1975, Edwards and Anderson developed a Ising magnet to describe the new phase; it featured nearest-neighbor interactions with fully random couplings drawn from a Gaussian distribution. While this paper set the stage for spin-glass theory, the model was notoriously difficult to analyze, and its results remain highly

contentious.

Soon after the publication of this theory, Sherrington and Kirkpatrick published their own interpretations of this model. Dropping the nearest-neighbor interactions in favor of all-to-all long range couplings, the theory lead to what is now known as the SK model of spin glasses. While the model is arguably less realistic than its predecessor, this single modification permits an "exact" solution, as briefly discussed in the Introduction. Exactly solvable models, irrespective of physically questionable assumptions, are invaluable to physics– they provide concrete cornerstones upon which more complex and realistic theories may be built.

A renewed interest in quantum mechanical generalizations of these models emerged in the 1990's. Most notably, Sachdev and Ye, following the ideas of SK, proposed a number of models which sought to elucidate the nature of random quantum magnets, eventually leading to the SY model: an all-to-all Heisenberg model of $SU(M)$ spins over N sites [87], given as

$$H = \frac{1}{\sqrt{NM}} \sum_{i>j}^{N} \sum_{a} J_{ij} S_i^a S_j^a \tag{3.1}$$

Where the operator S_i^a on site i is the ath generator of the $SU(M)$ group acting on local states belonging to a Spin representation labeled by n_b (e.g. for $M = 2, S = \frac{1}{2}$, these are the Pauli Matrices, with $n_b = 1$). As before, the J_{ij} are independent parameters up to symmetry, drawn from a real Gaussian distribution with zero mean and variance

$\mathcal{J}^2$. Using the replica trick, they discovered that there existed a "Quantum Spin Fluid Phase" whose properties were distinct from the classical spin glass. The vital parameters in this theory are the representation and group labels. n_b, M. Sachdev and Ye found three interesting limits: $n_b \to \infty$ yeilding the the magnetically ordered spin-glass phase; $M \to \infty$ taking the model deep into the spin-fluid phase;

$M, n_b \to \infty$, holding the ratio $n_b/M = \kappa$ fixed: whereby varying κ one can interpolate between the spin-glass and spin-fluid phases, indicating the presence of a phase-transition at some critical κ_c.

This novel "Spin Fluid" phase was found to have exciting properties. It harbors finite entropy at $T = 0$ due to a large manifold of symmetry related gapless states, and a self-energy who's imaginary part scales as $\mathrm{Im}(\Sigma(i\omega)) \sim \sqrt{\omega}$. As was later recognized, the latter property is interesting: in a fermionic representation, this form indicates the presence of NFL behavior — the spectrum of the theory is necessarily broad near the fermi-surface since $\mathrm{Im}(\Sigma(i\omega))$ does not fall off sufficiently fast to have a sharp quasi-particle description.

3.2   The Fermionic SYK Model

In 2016, the SY model was recast into its now popular form involving fermionic degrees of freedom rather than spins. Here we will discuss its solution and important properties following Sachdev's version of the SYK model due to its availability online [85]. In addition to this, the complex fermion construction has a direct semblance to the original

SY term under the slave fermion representation $\hat{S}^a \rightarrow S_{\alpha\beta}^a c_\alpha^\dagger c_\beta$.

The Hamiltonian of the complex SYK model is given by:

$$H = \frac{1}{(2N)^{3/2}} \sum_{ijkl} J_{ijkl} c_i^\dagger c_j^\dagger c_k c_l - \mu \sum_i c_i^\dagger c_i \tag{3.2}$$

where $J_{ijkl} = J_{klij}^* = -J_{jikl} = -J_{ijlk}$ is drawn from a Gaussian distribution characterized

by

$$\langle \mathcal{O}(J) \rangle = \int \mathcal{D}J \, \mathcal{O}(J) \, e^{-\frac{\sum |J_{ijkl}|}{\mathcal{J}^2}}, \tag{3.3}$$

where $\langle J_{ijkl} \rangle = 0, \langle |J_{ijkl}|^2 \rangle = \mathcal{J}^2$. This theory can be converted to the following coherent

state path integral over Grassmann valued fields $c^\dagger(\tau), c(\tau)$:

$$\mathcal{S} = \int_0^\beta d\tau \left[\sum_i c_i^\dagger (\partial_\tau - \mu) c_i - \frac{1}{(2N)^{3/2}} \sum_{ijkl} J_{ijkl} c_i^\dagger c_j^\dagger c_k c_l \right] \tag{3.4}$$

In order to make theoretical progress toward a solution, we must deal with the disorder in the couplings. There are multiple approaches, typically involving a disorder average, taken by various authors. The two most popular methods — directly disorder averaging the partition function $\mathcal{Z}$ (Sachdev) and disorder averaging the correlation functions appearing in the Dyson Equation (Kitaev) — turn out to be formally equivalent. Due to its relative simplicity we follow the former, which is accomplished by the replica trick. A full discussion of the method is beyond the scope of this thesis but, in summary,

the partition function lacks self-averaging properties. Similarly directly integrating over the disorder during the evaluation of expectation vales for potentially good observable introduces complications – it becomes unclear how to perform a gaussian average over the denominator $\mathcal{Z}_0 = \int \mathcal{D}(c^\dagger, c)e^{\mathcal{S}[J]}$. To circumvent this, we imagine preparing a large number $\mathcal{N}$ of identical ensembles of this system, each realizing a different random configuration of the J_{ijkl} couplings, and use the following identity for some function of the couplings $\mathcal{A}$:

$$\ln(\mathcal{A}) = \lim_{\mathcal{N} \to 0} \frac{\mathcal{A}^\mathcal{N} - 1}{\mathcal{N}} \tag{3.5}$$

such that the statistical average of the logarithm is given by

$$\langle \ln(\mathcal{A}) \rangle_J = \lim_{\mathcal{N} \to 0} \frac{\langle A^\mathcal{N} \rangle_J - 1}{\mathcal{N}} \tag{3.6}$$

The function of interest is the partition function of our theory, $\mathcal{Z}$, and it can be shown that $\ln \mathcal{Z}$, the free energy, is indeed a self averaging quantity. We are then free to proceed with caution, with the intention of taking the eventual $\mathcal{N} \to 0$ limit. Prior to taking this limit we may work with the replicated action by immediately carrying out the average over the J_{ijkl}:

$$\langle \mathcal{Z}^\mathcal{N} \rangle_J = \int \mathcal{D}J e^{-|J|^2/\mathcal{J}^2} e^{\sum_a^\mathcal{N} \mathcal{S}_a[J]} \tag{3.7}$$

with replica index a, resulting in the replicated theory:

$$\mathcal{S}_J = \int d\tau \; c_{ia}^\dagger(\partial_\tau - \mu)c_{ia} - \frac{\mathcal{J}^2}{4N^3} \sum_{aa'}^\mathcal{N} \int d\tau d\tau' \left| \sum_i^N c_{ia}^\dagger(\tau)c_{ia'}^\dagger(\tau') \right|^4 \tag{3.8}$$

Following Sachdev's original paper, the model may be recast by applying a series

56

of Hubbard-Stratonivich transformations to reduce the order of the action. Two such transformations, introducing fields Q, P results in:

$$
\begin{aligned}
\mathcal{S} = \sum_{ia} \int_0^\beta c_{ia}^\dagger \left(\partial_\tau - \mu\right) c_{ia} + \sum_{ab}^{\mathcal{N}} \int_0^\beta d\tau d\tau' \Big\{ &\frac{N}{4\mathcal{J}^2} |Q_{ab}(\tau, \tau')|^2 \\
+ \frac{N}{2} Q_{ab} |P_{ab}(\tau, \tau')|^2 &- Q_{ab}(\tau, \tau') P_{ba}(\tau', \tau) \sum_i c_{ia}^\dagger(\tau) c_{ib}(\tau') \Big\}
\end{aligned}
\tag{3.9}
$$

We see that this process has resulted in a theory that is quadratic in the fermion fields, allowing us to integrate them out. The action obtained from integration has a large N prefactor, allowing us to safely apply a saddle-point approximation in the $N \to \infty$ limit:

$$
\begin{aligned}
P_{ab}(\tau, \tau') &= \mathcal{G}_{ab}(\tau, \tau') = \langle c_a^\dagger(\tau) c_b(\tau') \rangle \\
Q_{ab}(\tau, \tau') &= \mathcal{J}^2 |P_{ab}(\tau, \tau')|
\end{aligned}
\tag{3.10}
$$

The saddle point equations let us identify the field P_{ab} with the fermion Greens function. Given the previous work of Sachdev and Ye [87], we don't expect that the low energy states in the limit of interest are in the Spin Glass phase, and therefore we can argue that we only need to consider the replica diagonal solutions, allowing us to drop the replica indices all together. Doing so allows us to identify $P_{ab}(\tau, \tau') = \delta_{ab} \mathcal{G}(\tau, \tau')$. Combining the equations of the saddle point solution and solving in terms of $\mathcal{G}$ we find:

$$
\mathcal{G}(i\omega_n) = \frac{1}{i\omega_n + \mu - i\Sigma(i\omega_n)}, \quad \Sigma(\tau) = -\mathcal{J}^2 \mathcal{G}(\tau) \mathcal{G}(\tau) \mathcal{G}(-\tau)
\tag{3.11}
$$

3.2.1 Low energy physics and solutions

Before investigating the symmetries at low energies, we first make a simplification to Eq. 3.11. In the low energy limit, we expect that the contribution of $i\omega \to 0$ to be small. Furthermore the scaling dimension of the chemical potential μ similarly makes it irrelevant in the low energy limit. We can then approximate our relation, strictly in the low energy limit, to be

$$\mathcal{G}(i\omega_n) = -\frac{1}{\Sigma(i\omega_n)}$$

As an integral equation, we then find that the above algebraic equation gives us the identity

$$\int d\tau_2 \mathcal{G}(\tau_1, \tau_2) \Sigma(\tau_2, \tau_3) = -\delta(\tau_1 - \tau_2) \tag{3.12}$$

This identity is critical to the solution of the model. Upon inspection, one finds a large symmetry associated with conformal maps via time reparametrizations $\tau \to f(\sigma)$ for arbitrary functions f, g .

$$\mathcal{G}(\tau_1, \tau_2) = [f'(\sigma_1)f'(\sigma_2)]^{-1/4} \frac{g(\sigma_1)}{g(\sigma_2)} \mathcal{G}(\sigma_1, \sigma_2)$$
$$\Sigma(\tau_1, \tau_2) = [f'(\sigma_1)f'(\sigma_2)]^{-3/4} \frac{g(\sigma_1)}{g(\sigma_2)} \Sigma(\sigma_1, \sigma_2) \tag{3.13}$$

The implication of the arbitrary g factors is that there exists an emergent $U(1)$ gauge symmetry at low energies which is not present in the microscopic theory described by 3.2

By assuming a power law dependence on complex frequency $z = \omega_r + i\omega$, one can
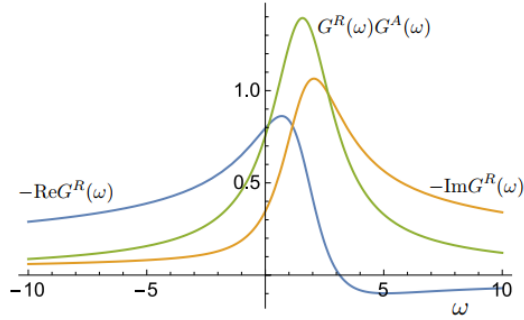
Figure 3.1: Illustration of the Greens function $\mathcal{G}(\omega)$ for the complex fermion SYK model.

show that the solution to the above equations can be given by

$$\mathcal{G}(z) = C\frac{e^{-i(\pi/4+\theta)}}{\sqrt{z}}, \quad \operatorname{Im}(z) > 0, |z| \ll \mathcal{J}, T = 0 \tag{3.14}$$

where C is an unimportant constant and θ is a parameter that characterizes the particle-hole asymmetry.

3.2.2 Notable Features

The most important observation about the Greens function of Eq. 3.14 is that it describes NFL behavior. This solution very clearly demonstrates that the spectrum of the SYK model is gapless at low temperatures. Similarly, an immediate consequence of the scaling form of $\mathcal{G}$ is that $\Sigma(\imath\omega) \sim \sqrt{i\omega}$, so that the self energy of the fermions is slowly vanishing in the vicinity of the fermi surface (here, a "fermi-point"), absent of any sharp poles characteristic of FL phases.

The entropy at $T = 0$ can be extracted by using the usual thermodynamic relations. Investigating the model in the high temperature UV limit, where μ is a relevant param-

eter, one can make an expansion of $\mathcal{G}$ to second order in $1/i\omega_n$. An inversion of this approximation allows one to show that at fixed total charge,

$$\left.\frac{\partial S}{\partial Q}\right|_T = -\left.\frac{\partial \mu}{\partial T}\right|_Q = 2\pi\mathcal{E}, \quad T \to 0 \tag{3.15}$$

From this we infer that the $T = 0$ ground state has a finite entropy density, which can be demonstrated by asserting gthat the $\mathcal{Q} = 0$ state of the SYK model necessarily has $S = 0$.

3.3 Generalizing the SYK model

In Kitaev's version construction, the SYK model is a $(0+1)d$ system that consists of N Majorana (real), rather than complex, fermions, with random all-to-all 4-fermion interactions. The couplings are necessarily drawn from a real Gaussian distribution in this case. The use of majorana DOFs rather than complex fermions has no significant effects on the qualitative characteristics of the solution or underlying phase of the $T \to 0$ model. This model was later generalized by Maldecena and Stanford to the SYK_q model, which replaces the 4-fermion interaction term with a q-fermion term [122]:

$$
\begin{aligned}
H_{\text{SYK}_q} &= (i)^{\frac{q}{2}} \sum_{i_1 < \cdots < i_q} J_{i_1 \ldots i_q} \chi_{i_1} \cdots \chi_{i_q} \\
\langle J_{i_1 \cdots q}^2 \rangle &= \frac{2^{q-1}}{q} \frac{\mathcal{J}^2 (q-1)!}{N^{q-1}}
\end{aligned}
\tag{3.16}
$$

where χ_{i_n} are Majorana fermion operators with index $i_n = 1 \cdots N$, and $J_{i_1 \ldots i_q}$ is a fully anti-symmetric tensor whose each entry is drawn from a Gaussian distribution with zero mean and variance as given in Eq. 3.16

When $q = 2$, the model is simply N Majorana fermions with only random hopping terms, which can be solved completely using the random matrix theory. The $q = 4$ SYK model (hereafter labeled as SYK$_4$ model) is most thoroughly studied. We write the Hamiltonian, with a rescaling of the $J's$ for convenience, as

$$H_{\text{SYK}_4} = \sum_{ijkl} \frac{J_{ijkl}}{4!} \chi_i \chi_j \chi_k \chi_l, \tag{3.17}$$

where J_{ijkl} is drawn from a Gaussian distribution with a variance of $\overline{J_{ijkl}^2} = 3! J_4^2 / N^3$. As demosntrated for the complex fermion version previously, in the limit of large N and low temperature, the SYK$_4$ model can be solved exactly via saddle point equations and exhibits an emergent conformal symmetry. The scaling dimension of the Fermion operator is identically $\Delta_f = 1/4$, which suggests a non-Fermi liquid behavior without quasi-particle excitations [43, 122].

Furthermore, the exact solution also suggests that the SYK$_4$ model is maximally chaotic, in the sense that its Lyapunov exponent [43, 122], a measure of quantum chaos, saturates the universal upper bound established in Ref. [99]. The saturation of the universal upper bound is also a feature of black holes. In fact, the exact solution also indicates that the SYK$_4$ model should indeed be holographically dual to a gravity theory [84, 33, 80, 44, 26, 122, 34]. When $q > 2$, all SYK$_q$ models share the properties such as maximally chaotic non-Fermi liquid ground states, and an approximate emergent conformal symmetry at large-N.

Many other aspects of the SYK model, including the numerical simulations, generalizations to models with higher symmetry, and higher dimensions, have been investigated

recently [25, 123, 34, 2, 35, 33, 32, 37, 3, 113, 104, 77, 36, 54].

One peculiar feature of the SYK_q model with $q > 2$ is that, in the large N limit, the chaotic non-Fermi liquids all have finite entropy density even when the temperature approaches zero [25, 33, 43, 122]. One might conjecture directly that the system has instabilities towards states with lower (or zero) zero-temperature entropy density upon perturbations. Indeed, in experimental systems, the non-Fermi liquid state at a quantum critical point is usually buried in a dome of ordered phase with spontaneous symmetry breaking at low temperature [64]. One usual scenario is the emergence of a superconducting dome around the quantum critical point, which occurs in cuprates, pnictides superconductors, and also some heavy fermion systems. Thus it is meaningful to ask whether the SYK_q model, especially the SYK_4 model is unstable against spontaneous symmetry breaking. Or in other words, the SYK_4 model could be the parent state of ordered phases at the infrared [1].

3.4 Charting a map of the NFL phase: A Novel Pairing Instability

We now move to study a class of perturbations on the SYK_q models, in the hopes of understanding the relationship the NFL phase has with neighboring ordered states. Of particular interest to us is that the scaling dimension of the Majorana Fermion operator

---

[1]Here we use the standard Landau-Ginzburg's definition of an ordered phase: an order means some symmetry of the system is spontaneously broken, or in other words, an order parameter that transforms non-trivially under the symmetry acquires a long range correlation.

becomes $\Delta_f = 1/q$ in the SYK$_q$ model. Simple a simple tree-level scaling analysis then shows that any SYK$_q$ model is inherently unstable to perturbation by a SYK$_p$ term for $p < q$; in fact, under renormalization, a SYK$_q$ model will, in the absence of fine-tuning, *generate* such terms generically.

Given this, the non-Fermi liquid at the SYK$_4$ fixed point should be unstable to any SYK$_2$ perturbation. However, the SYK$_4$ has a time-reversal symmetry, under which all fermion bilinears are odd; hence, the time-reversal symmetry $\mathcal{T}$ forbids the generation of these perturbations. By tuning the system to ensure that the SYK$_2$ terms are absent from the bare action, we may restrict our attention to the four-fermion terms which are symmetric under $\mathcal{T}$. As we will show, the non-Fermi liquid SYK$_4$ model is unstable against a series of four-fermion interactions that preserve all the symmetries, and the system flows to a state with spontaneous breaking of $\mathcal{T}$.

A similar analysis can be generalized to the SYK$_q$ non-Fermi liquid with $q > 4$ perturbed by the four-Fermion interactions we design. Interestingly, the four fermion interactions can drive the SYK$_q$ model to a series of new stable fixed points with conformal symmetry.

3.5 A perturbed $q = 4$ SYK model

Following the above discussion, one finds that the following symmetry-allowed perturbation is marginally relevant:

$$H = \frac{J_{ijkl}}{4!}\chi_i\chi_j\chi_k\chi_l + \frac{u}{2}C_{ij}C_{kl}\chi_i\chi_j\chi_k\chi_l \qquad (3.18)$$
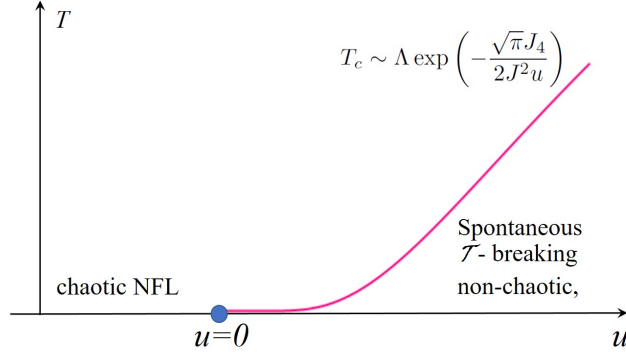
Figure 3.2: The phase diagram of Eq. 3.18.

Both J_{ijkl} and C_{ij} are anti-symmetric random tensors drawn from a gaussian distribution. We choose the following normalization for J_{ijkl} and C_{ij}:

$$
\begin{aligned}
\overline{J_{ijkl}} &= 0, & N^3\overline{J_{ijkl}^2} &= 3!J_4^2 \\
\overline{C_{ij}} &= 0, & N^2\overline{C_{ij}C_{kl}} &= J^2(\delta_{ik}\delta_{jl} - \delta_{il}\delta_{jk}).
\end{aligned}
\tag{3.19}
$$

Note that J_4 has the dimension of energy, while J has the dimension of (energy)$^{1/2}$. The results of this section is summarized in phase diagram Fig. 3.2.

The two terms in Eq. 3.18 have the same symmetry: the time-reversal symmetry $\mathcal{T}$ which acts as $\chi_j \to \chi_j$, $i \to -i$ (it is the same time-reversal symmetry of the boundary states of the topological superconductor in the BDI class [50, 88, 82]), and a statistical O(N) symmetry. We will demonstrate that, by tuning u from negative to positive, the system goes through a continuous phase transition from a chaotic phase to a non-chaotic phase. The critical properties of this transition are analogous to that of the Kosterlitz-Thouless transition, with exponent $\nu = +\infty$.

3.5.1 The $u-$term

Before we study Eq. 3.18, let us start with the Hamiltonian with only the second term:

$$H' = \frac{u}{2} C_{ij} C_{kl} \chi_i \chi_j \chi_k \chi_l. \tag{3.20}$$

This Hamiltonian can be written as $H' = -u\hat{b}^2/2$, with $\hat{b} = iC_{jk}\chi_j\chi_k$. Since $\hat{b}$ commutes with H', it is a conserved quantity. Thus every eigenstate of H' is an eigenstate of $\hat{b}$ with eigenvalue b. When $u > 0$, the ground state of H' has the maximum eigenvalue of $\hat{b}$.

Now we can view $\hat{b}$ as a quadratic fermion Hamiltonian with random hopping. To maximize $\hat{b}$, the system fills all the negative (or positive) eigenvalues of the single fermion energy level ε_l, and $\text{Max}[|b|] = |\sum \varepsilon_l|$ with $\varepsilon_l < 0$.

The single particle energy levels ε_l are the eigenvalues of the random Hermitian matrix iC. Based on the semi-circle law, the average number of eigenvalues of iC in $(\varepsilon, \varepsilon + d\varepsilon)$ is given by $\rho(\varepsilon)d\varepsilon$ with

$$\rho(\varepsilon) = \frac{N^2}{2\pi J^2} \sqrt{\frac{4J^2}{N} - \varepsilon^2}. \tag{3.21}$$

Then we can obtain the average value of $\text{Max}[|b|]$ as

$$\text{Max}[|b|] = \left| \int_{\varepsilon<0} d\varepsilon \varepsilon \rho(\varepsilon) \right| = \frac{4JN^{\frac{1}{2}}}{3\pi}. \tag{3.22}$$

Therefore, the average ground state energy of H' is $E_0(H') = -\frac{16uJ^2N}{9\pi^2}$. Thus just like the ordinary SYK model, H' normalized as in Eq. 3.19 is an order-N term.

For $u < 0$, all states with $b = 0$ are ground states, and $b = 0$ is a very "loose" condition. We will argue that H' with $u < 0$ behaves like a completely free system with

zero Hamiltonian. The (many-body) spectrum of $\hat{b}$ is given by $b = \sum_{\varepsilon_l > 0} \varepsilon_l n_l$, where the

occupation number $n_l = \pm 1$. This expression of b is similar to an $\frac{N}{2}$-step random walk

centered around 0. The distribution of b should therefore be Gaussian. The standard

deviation σ_b of this "random walk" is given by

$$\sigma_b^2 = \sum_{\varepsilon_l > 0} \varepsilon_l^2 = \frac{1}{2} \text{Tr} \left((iC)^\dagger (iC) \right) = \sum_{i<j} |C_{ij}|^2 = \frac{N-1}{2N} J^2. \tag{3.23}$$

The (many-body) density of states of $\hat{b}$ can be then approximated by

$$\rho(b) = 2^{\frac{N}{2}} \sqrt{\frac{N}{\pi(N-1)J^2}} e^{-\frac{Nb^2}{(N-1)J^2}}, \tag{3.24}$$

namely the number of eigenvalues of $\hat{b}$ in $(b, b+db)$ is given by $\rho(b)db$. The expression

$\rho(b)$ of the density of states $\hat{b}$ is most accurate near $b = 0$, which is exactly the region of

interest when $u < 0$. We can now calculate the partition function

$$\mathcal{Z} = \int db \rho(b) e^{\beta u b^2} = 2^{\frac{N}{2}} \frac{1}{\sqrt{1 + \beta |u| \frac{N-1}{N} J^2}}. \tag{3.25}$$

The entropy density $\mathcal{S}$ can be written as $\mathcal{S} = \frac{1}{N} \left(\log \mathcal{Z} - \beta \frac{\partial}{\partial \beta} \log \mathcal{Z} \right)$. Interestingly, we

notice that, for any fixed β,

$$\lim_{N \to \infty} \mathcal{S} = \frac{1}{2} \log 2. \tag{3.26}$$

Therefore, if we take the large N limit first before we take $\beta \to \infty$, we will conclude that

the "ground state" entropy density is given by $\frac{1}{2} \log 2$. Such an entropy density is exactly

the same as the system with zero Hamiltonian. Therefore, we argue that the system with

$u < 0$ behaves like a completely free system with zero Hamiltonian. Using the partition
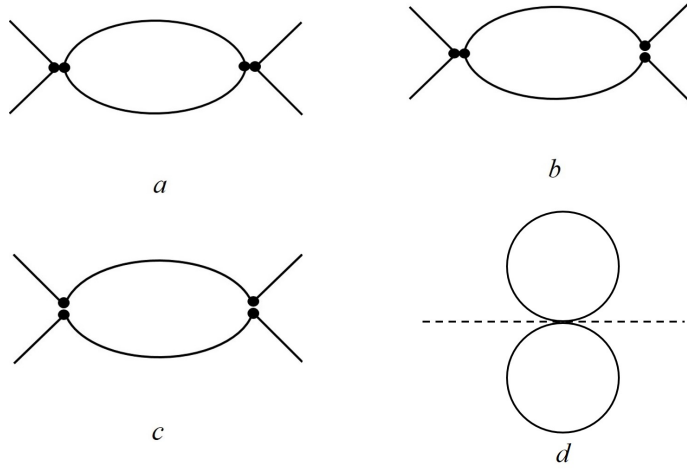
66

Figure 3.3: (a), (b), (c), the diagrams that we consider for the leading order RG for the coupling constant u in Eq. 3.18. Only diagram (a) contributes in the large$-N$ limit. (d), the leading order RG for u in Eq. 3.33, which is equivalent to (a), the solid and dashed lines are fermion and boson Green's functions.

function, we can also calculate the specific heat of H' with $u < 0$:

$$c_v = -\beta \frac{dS}{d\beta} = \frac{1}{2N} \left(\frac{\frac{N-1}{N}|u|J^2\beta}{1 + \frac{N-1}{N}|u|J^2\beta} \right)^2. \tag{3.27}$$

3.5.2 Renormalization Group of u

When u is treated as a perturbation in Eq. 3.18, power counting indicates that it is a marginal perturbation at the SYK$_4$ fixed point. Now we perform a perturbative renormalization group calculation for u. We evaluate the fermion Green's function at the SYK$_4$ fixed point:

$$G(\tau) = \left(\frac{1}{4\pi} \right)^{1/4} \frac{\mathrm{sgn}(\tau)}{|J_4\tau|^{1/2}}, \qquad G(i\omega) = \pi^{1/4} \frac{i\mathrm{sgn}(\omega)}{|J_4\omega|^{1/2}}. \tag{3.28}$$

The diagram Fig. 4.46a leads to the following beta function for u:

67

$$\beta(u) = \frac{du}{d\ln l} = \frac{2}{\sqrt{\pi}} \frac{1}{J_4} \sum_{i,j} |C_{ij}|^2 u^2 = \frac{2J^2}{\sqrt{\pi}J_4} u^2. \tag{3.29}$$

Here we have replaced $\sum_{i,j} |C_{ij}|^2$ by J^2, which is consistent with the distribution of C_{ij}, in the large N limit.

Diagrams Fig. 4.46b and c will contribute at the sub-leading order of $1/N$. For example, Fig. 4.46b will generate a term $\sim \sum_{m,n} C_{im}C_{mn}C_{nj}C_{kl}u^2\chi_i\chi_j\chi_k\chi_l$. This term is sub-leading in $1/N$ counting after disorder average.

The beta function indicates that the H' perturbation with $u > 0$ ($u < 0$) is marginally relevant (marginally irrelevant) at the SYK_4 fixed point. If we start with a small perturbation $u > 0$, the RG equation implies that it will become order 1 at the energy scale $\tilde{\Lambda}$ where

$$\tilde{\Lambda} \sim \Lambda \exp\left(-\frac{\sqrt{\pi}J_4}{2J^2u}\right). \tag{3.30}$$

Λ is the UV cut-off of the RG that we can roughly take as $\Lambda \sim J_4$. The standard scaling relation between the energy scale (mass gap) and the tuning parameter r away from a critical point r_c is $\tilde{\Lambda} \sim |r - r_c|^\nu$, thus the quantum phase transition led by tuning u across zero has exponent $\nu = +\infty$, which is analogous to the Kosterlitz-Thouless transition [53].

This RG analysis predicts that the SYK model, although describes a non-Fermi liquid state, actually has similar instabilities as the ordinary Fermi liquid: there exists symmetry allowed four fermion terms that are marginally relevant/irreleavant depending on their sign. When u is marginally relevant, our mean field solution in the next subsection (and

the analysis of H' in the previous subsection) suggests that the fate of the SYK model is also similar to the ordinary Fermi liquid: the system develops long range correlation $\langle \hat{b}(0) \; \hat{b}(\tau) \rangle$, where $\hat{b}$ is the fermion-bilinear operator defined in the previous subsection. The physics here is analogous to the condensation of Cooper pair of the ordinary Fermi liquid theory.

The effective action of Eq. 3.18 after a Hubbard-Stratonovich transformation reads

$$
\begin{aligned}
\mathcal{S}_{eff} &= \int d\tau \frac{1}{2} \sum_i \chi_i \partial_\tau \chi_i + \sum_{ijkl} \left\{ \frac{J_{ijkl}}{4!} \chi_i \chi_j \chi_k \chi_l + \frac{u}{2} C_{ij} C_{kl} \chi_i \chi_j \chi_k \chi_l \right\} \quad (3.31) \\
&= \int d\tau \left(\frac{1}{2} \chi_i \partial_\tau \chi_i + \frac{u}{2} b^2 - iu C_{jk} b \chi_j \chi_k \right) + \frac{J_{ijkl}}{4!} \chi_i \chi_j \chi_k \chi_l \quad (3.32)
\end{aligned}
$$

The Hubbard-Stratonovich field b is a real field. Einstein summation convention is assumed in all the equations. The indices are summed from 1 to N with the constraint that different indices cannot take the same value. Now we can perform disorder average on J_{ijkl} and C_{jk} with the distribution Eq. 3.19. Assuming everything is replica diagonal (justification of this assumption will be given in section IV), the disorder-averaged action is equivalent to the following form:

$$
\begin{aligned}
\mathcal{S}_{eff} &= \int d\tau \frac{1}{2} \chi_i \partial_\tau \chi_i + \frac{u}{2} b^2 - u^2 \frac{J^2}{N^2} \int d\tau_1 d\tau_2 \; (b(\tau_1) \; b(\tau_2)) (\chi_j(\tau_1) \chi_j(\tau_2))^2 \\
&\quad - \frac{J_4^2}{8N^3} \int d\tau_1 d\tau_2 \; (\chi_i(\tau_1) \chi_i(\tau_2))^4. \quad (3.33)
\end{aligned}
$$

This disorder-averaged action has an explicit $O(N)$ symmetry, the fermion carries a vector representation of the $O(N)$. The beta function for u can also be computed based on Eq. 3.33. Fig. 4.46d based on Eq. 3.33 makes the same contribution to the beta
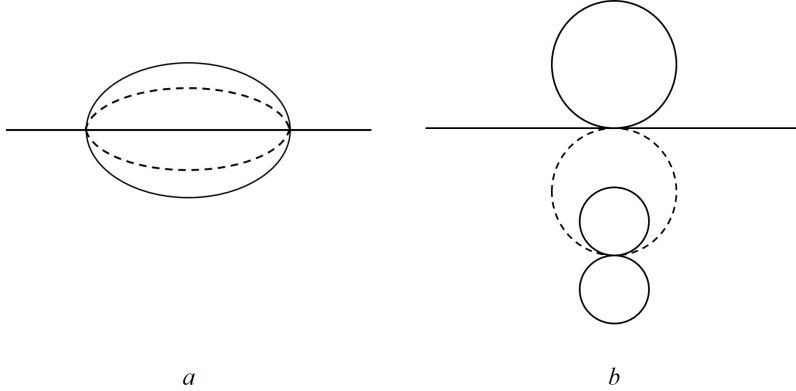
Figure 3.4: The fermion wave function renormalization based on Eq. 3.18 and Eq. 3.33 respectively. These diagrams correspond to a u^3 term in the beta function, and it carries a factor of $1/N$.

function as Fig. 4.46a. In the large$-N$ limit, the beta function Eq. 3.29 is actually exact. The higher order terms of the beta function can be ignored in the large$-N$ limit even when u grows beyond order-1 (and hence becomes dominant) under the RG flow. For example the fermion wave function renormalization in Fig. 3.4 corresponds to a u^3 term in the beta function, and it carries a coefficient $1/N$. Other diagrams, such as the ladder diagrams for the four-point functions computed in Ref. [122], also contribute at the sub-leading $1/N$ order compared with Fig. 4.46a,d.

3.5.3 Mean field solution

We can introduce fermion Green's function and Self-energy function G and Σ by inserting the following integral in the action (G and Σ are real fields):

$$\int \mathcal{D}\Sigma \mathcal{D}G \exp\left\{-\frac{N}{2}\Sigma(\tau_1,\tau_2)\left(G(\tau_1,\tau_2)-\frac{1}{N}\sum_i \chi_i(\tau_1)\chi_i(\tau_2)\right)\right\} \qquad (3.34)$$

Then the action S_{eff} is equivalent to:

$$\begin{aligned}
\mathcal{S}_{eff} &= -N \log \mathrm{Pf}\,(\partial_\tau - \Sigma) + \int d\tau\, \frac{u}{2}b^2 - u^2 J^2 \int d\tau_1 d\tau_2\,(b(\tau_1)b(\tau_2))(G(\tau_1,\tau_2))^2 \\
&\quad -N\frac{J_4^2}{8}\int d\tau_1 d\tau_2\,(G(\tau_1,\tau_2))^4 + N\int d\tau_1 d\tau_2\,\frac{1}{2}\Sigma(\tau_1,\tau_2)G(\tau_1,\tau_2)
\end{aligned} \tag{3.35}$$

Since the H' term itself has long range correlation of $\hat{b}$, we expect that the phase with relevant u perturbation also develops the long range correlation of $b(\tau)$. Since the ground state of H' has $b \sim N^{1/2}$, let us assume $\langle b(\tau_1)b(\tau_2)\rangle = Nw^2$, where w takes order-1 value with no time dependence. Then we can derive the mean field equation for the Green's function, the self-energy, and also w:

$$G(i\omega_n)^{-1} = -i\omega_n - \Sigma(i\omega_n) \tag{3.36}$$

$$\Sigma(\tau) = J_4^2 G(\tau)^3 + 4u^2 J^2 w^2 G(\tau) \tag{3.37}$$

$$\int d\tau \left(uJ^2 G(\tau)^2 - \frac{1}{2}\delta(\tau) \right) uw = 0 \tag{3.38}$$

The saddle point Eq. 3.38 has two possible solutions: $w = 0$ or

$$\int d\tau\, G(\tau)^2 = \frac{1}{2uJ^2}. \tag{3.39}$$

For the $w = 0$ saddle point, these equations return to the saddle point equations for the pure $q = 4$ SYK model. The system is in the chaotic non-Fermi liquid phase. However, when $w \neq 0$, in the low energy, the second term in Eq. 3.37 becomes dominant, and the system is effectively described by a random two fermion interaction and it is in a non-chaotic phase [2]. In this phase, $G(\tau)$ will depend on the values of w, and we can

---

[2]The random four-fermion interaction, though irrelevant with the presence of a random two-body interaction, still has perturbative effect, and may lead to non-maximal chaos at finite temperature. This effect was discussed in Ref. [77]. Here we still call this phase as non-chaotic phase, for conciseness.

self-consistently determine w from Eq. 3.39. The chaotic-nonchaotic transition happens when u is tuned from negative to positive through 0. When u is negative, Eq. 3.39 has no solution and w has to be 0. For any positive u, at zero temperature there is always a solution with finite w. The state with long range correlation $\langle b(0)b(\tau) \rangle$ spontaneously breaks the time-reversal symmetry $\mathcal{T} : \chi_j \to \chi_j$.

3.5.4 Estimation of w as function of model parameters

There are two time scales in our problem, $\tau_2^{UV} \sim (uwJ)^{-1}$ and $\tau_4^{UV} \sim J_4^{-1}$. In the small u limit, namely $\tau_2^{UV} \gg \tau_4^{UV}$, the contribution of the integral in Eq. 3.39 mainly comes from the region $\tau \in [\tau_4^{UV}, \tau_2^{UV}]$, and in this region $G(\tau)$ takes the form of the ordinary SYK model:

$$\int d\tau \, G(\tau)^2 \simeq \int_{\tau_4^{UV}}^{\tau_2^{UV}} d\tau \frac{2}{\sqrt{\pi}} \frac{1}{J_4 \tau} = \frac{2}{\sqrt{\pi} J_4} \log(\frac{J_4}{uwJ}) \tag{3.40}$$

Together with Eq. 3.39, we have

$$w \simeq \frac{J_4}{uJ} \exp\left(-\frac{\sqrt{\pi} J_4}{4uJ^2} \right). \tag{3.41}$$

This result is consistent with the observation that a positive u is only marginally relevant. The size of the condensate is analogous to the superconductor gap of the BCS theory.

At finite u, the scale $\tilde{\Lambda}$ in Eq. 3.30 can be viewed as the critical temperature T_c below which the system develops nonzero w and hence spontaneously breaks time-reversal $\mathcal{T}$. Our numerical solution of the mean field equations Eq. 3.36,3.37,3.38 confirms the scaling between T_c and u (Fig. 4.25). In the numerical solution we have taken $J^2/J_4 = 1$. Our RG Eq. 3.30 predicts that $T_c \sim \exp(-\frac{\sqrt{\pi}}{2} \frac{1}{u}) = \exp(-0.886/u)$, and our mean field solution
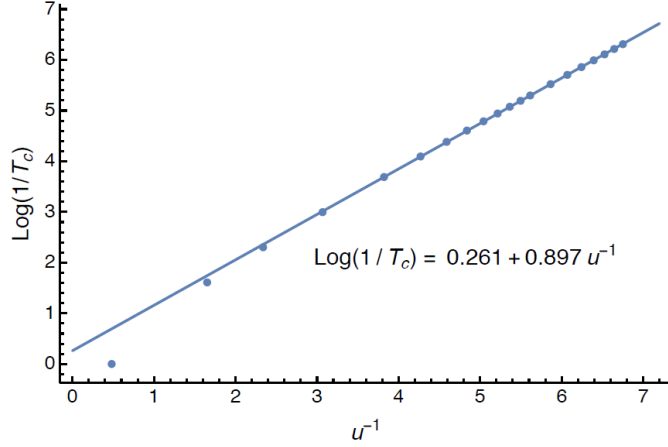
Figure 3.5: Transition temperature T_c as a function of u by numerically solving the mean field equations (3.36-3.38). This confirms the scaling relation in Eq. 3.30.

gives $T_c \sim \exp(-0.897/u)$.

3.5.5 Further generalized perturbations

Now let us consider a series of generalized Hamiltonians:

$$H = \text{SYK}_q + H', \qquad H' = \frac{u}{2} \sum_{a=1}^{M} C_{ij}^a C_{kl}^a \chi_i \chi_j \chi_k \chi_l, \tag{3.42}$$

with $M \sim N^A$. SYK_q is the generalized SYK model with a random $q-$fermion interaction, and $A \geq 0$. We first choose the following normalization of C_{ij}^a

$$N^2 \, \overline{C_{ij}^a C_{kl}^b} = J^2 \delta_{ab}(\delta_{ik}\delta_{jl} - \delta_{il}\delta_{jk}). \tag{3.43}$$

We still start with the beta function of u. If we evaluate the Green's functions at the SYK_q fixed point, the beta function of u reads

$$\beta(u) = \frac{du}{d\ln l} = (1 - \frac{4}{q})u + Cu^2 + \tilde{c}_3 \frac{M}{N} u^3 + \cdots \tag{3.44}$$

73

where $C > 0$ is an order-1 constant.

Cases with $A < 1$

For $A < 1$, we can keep just the linear and quadratic terms of the beta function, as all the higher order terms vanish in the large$-N$ limit, when u is order-1 or smaller. For $A < 1$ and $u > 0$, u is relevant at the SYK fixed point for $q > 4$, and marginally relevant for $q = 4$. We expect the system to behave similarly as the case with $M = 1$ and $q = 4$, namely the relevant u perturbation drives the system into a nonchaotic phase with spontaneous $\mathcal{T}$ breaking: $\lim_{\tau \to \infty} \sum_a \langle b^a(0)\ b^a(\tau) \rangle \neq 0$, where $\hat{b}^a = iC^a_{jk}\chi_j\chi_k$. The same set of equations as Eq. 3.36,3.37,3.38 can be derived, and in this case $\sum_{a=1}^M \langle b^a(0)\ b^a(\tau) \rangle = Nw^2$, and w is given by Eq. 3.41.

Exact diagonalization of the H' term in this case confirms our expectations. To detect the long range correlation of $\langle b^a(0)b^a(\tau) \rangle$, we measure the zero-frequency component of the boson spectral function. The spectral function is defined as

$$D(\omega) = \frac{1}{M} \sum_{a=1}^M \sum_n \left| \langle 0|\hat{b}^a|n \rangle \right|^2 \delta(\omega - E_n + E_0), \qquad (3.45)$$

where E_n and $|n\rangle$ are eigenenergies and corresponding eigenstates of the Hamiltonian H', obtained from the exact diagonalization $H'|n\rangle = E_n|n\rangle$ $(n = 0, 1, 2, \cdots)$. $n = 0$ labels the ground state. The C^a_{ij} normalization in Eq. 3.43 ensures that $\overline{\hat{b}^{a\dagger}\hat{b}^a} = 1$ (the identity matrix) in the large N limit, so that $D(\omega)$ has a well-defined thermodynamic limit. If the static correlation $D(\omega = 0)$ remains finite in the thermodynamic limit $N \to \infty$,

74

then the system will develop long range correlation and spontaneously break $\mathcal{T}$. The Fig. 3.6 shows the result of the static correlation $D(\omega = 0)$ (in logarithmic scale) for different N at $A = 0.2$ and $u > 0$. $\ln D(0)$ oscillates with N in an eight-fold period due to the systematic change of random-matrix ensemble of H' as discussed in Ref. [123]. Apart from the oscillation, $D(\omega = 0)$ remains at and converges to a finite level (roughly indicated by the dashed line in Fig. 3.6). Therefore our finite-sized calculation indeed supports a nonchaotic phase with spontaneous $\mathcal{T}$ breaking for the $A < 1$ and $u > 0$ case. By contrast, for either $A > 1$, or $A < 1$ while $u < 0$, ED shows $D(0)$ decreases rapidly with increasing N (Fig. 3.7).
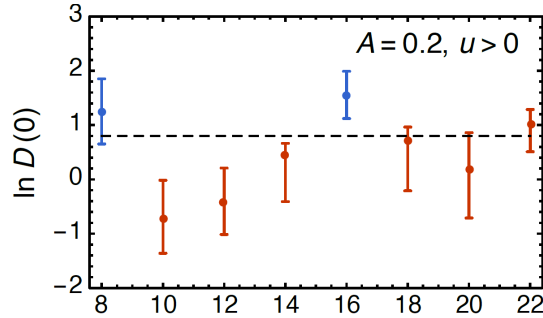

Figure 3.6: The logarithmic static correlation $\ln D(0)$ v.s. the fermion number N for the case of $u > 0$ and $A = 0.2$. The error bar shows the statistical deviation over different random realizations of the coefficient C_{ij}^a. When N mod $8 = 0$, $D(\omega = 0)$ vanishes exactly, so we use the finite frequency extrapolation to obtain the static correlation $D(0) = \lim_{\omega \to 0} D(\omega)$ in these cases.

For $A < 1$ and $u < 0$, the u term flows to a stable fixed point $u^* \sim -(1 - 4/q)/C$. At this fixed point, since u^* is an order-1 number, the fermion self-energy correction Fig. 3.4 is at the M/N order, which vanishes in the large$-N$ limit for $A < 1$. Thus the fermion scaling dimension remains the same as the SYK$_q$ model: $\Delta_f = 1/q$. But at this stable fixed point, the boson field $b^a \sim iC_{jk}^a \chi_j \chi_k$ acquires a correction, and has
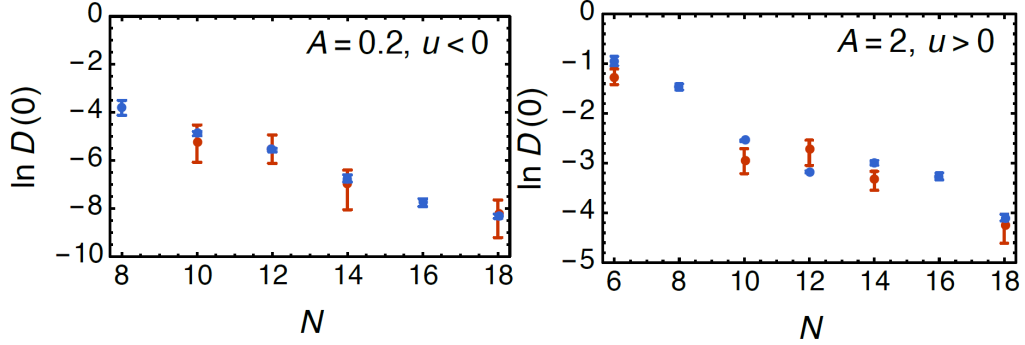
Figure 3.7: The logarithmic static correlation $\ln D(0)$ v.s. the fermion number N for the case of $A = 0.2$, $u < 0$ (left), and $A = 2$, $u > 0$ (right). Neither case shows long range correlation of the bosonic field b^a. Both $D(\omega = 0)$ (red) and $\lim_{\omega \to 0} D(\omega)$ (blue) are plotted in the figures.

scaling dimension $\Delta_b = 1 - 2/q$ in the large$-N$ limit. Starting with a SYK$_q$ model with $q > 4$, changing the sign of u will drive a chaotic-nonchaotic transition with exponent $\nu = q/(q - 4)$.

Cases with $A > 1$

For $A > 1$, the RG equation is uncontrolled because the higher order terms in the beta function dominate in the large$-N$ limit. However, we can understand the model by taking the limit $M \to +\infty$ first. One intuitive way to think about this case is that according to the central limit theorem $\sum_{a=1}^{M} C_{ij}^a C_{kl}^a$ with $M \to +\infty$ follows the Gaussian distribution. So for either sign of u, Eq. 3.42 should behave the same as the $q = 4$ SYK model. In order to explicitly demonstrate this statement, it is more convenient to use a different normalization of C_{ij}^a:

$$N^{(3+A)/2} \, \overline{C_{ij}^a C_{kl}^b} = J^2 \delta_{ab}(\delta_{ik}\delta_{jl} - \delta_{il}\delta_{jk}). \tag{3.46}$$

We can perform the disorder average and integrating out C_{ij}^a, the leading order term in the large$-N$ limit is an eight-fermion interaction term $\sim \frac{u^2 J^4}{N^3} \int \int d\tau d\tau' (\chi_i(\tau)\chi_i(\tau'))^4$, just like the disorder averaged $q = 4$ SYK model, while all higher order $8n$-fermion interaction terms $\mathcal{S}^{(8n)}$ are suppressed $\sim \frac{(u^2 J^4)^n}{N^{3n+A(n-1)}} \left(\int \int d\tau d\tau' (\chi_i(\tau)\chi_i(\tau'))^4 \right)^n$. Thus for $A > 1$, the $u-$term actually behaves the same as the SYK model in the large$-N$ limit. This conclusion is consistent with the previous study of a similar generalization of the SYK model [20].

3.5.6 The H' term with $A = 1$

$A = 1$ is the critical situation, and the H' term itself (equivalent to taking $q = +\infty$ in Eq. 3.42) is already interesting enough when $A = 1$. With the H' term only, we numerically solve the following coupled Schwinger-Dyson equations with the normalization from Eq. 3.46:

$$\tilde{G}_f(i\omega_n)^{-1} = -i\omega_n - \tilde{\Sigma}_f(i\omega_n), \quad \Sigma_f(\tau) = 4\sqrt{\frac{M}{N}} u^2 J^2 G_b(\tau) G_f(\tau) \qquad (3.47)$$

$$\tilde{G}_b(i\omega_n)^{-1} = u - \tilde{\Sigma}_b(i\omega_n), \quad \Sigma_b(\tau) = 2\sqrt{\frac{N}{M}} u^2 J^2 G_f^2(\tau) \qquad (3.48)$$

Alternatively, by assuming that $G_b(\tau) \sim B/|\tau|^{2\Delta_b}$ and $G_f(\tau) \sim F \, \text{sgn}(\tau)/|\tau|^{2\Delta_f}$ in the infrared limit, Eq. 3.47,3.48 reduce to the following equation for Δ_b for each ratio M/N:

$$\frac{M}{N} = \left(\frac{1 - 2\Delta_f}{1 - 4\Delta_f} \right) \frac{1}{\cot(\pi\Delta_f)^2 - 1}. \qquad (3.49)$$
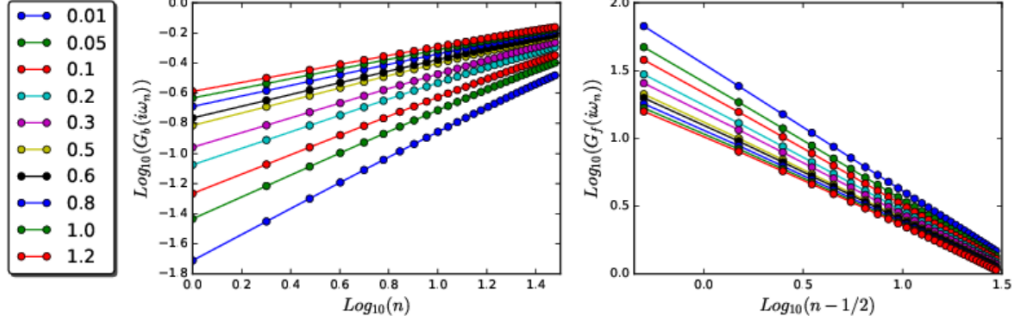
77

Figure 3.8: The numerical solution of Eq. 3.47,3.48, for $u = -1$, $J = 1$, $\beta = 300$ with different M/N, without assuming a conformal solution from the beginning. Both the boson and fermion Green's functions have nice power-law scaling with the frequency, whose scaling dimensions depend on M/N.
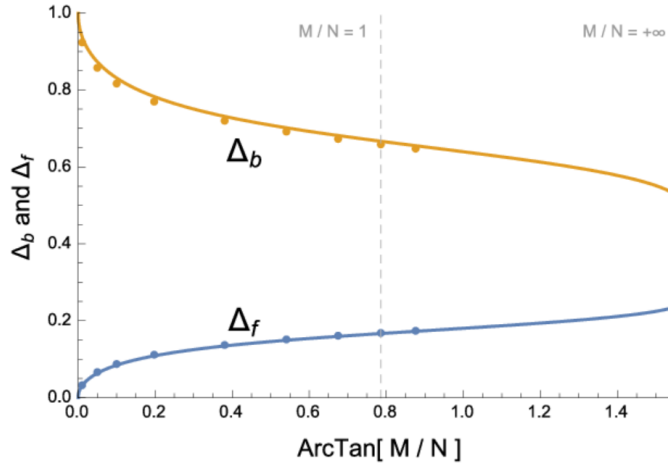
Figure 3.9: We numerically solve the Schwinger-Dyson equations (3.47-3.48) for $u = -1, J = 1, \beta = 300$ and fit the low frequency part as a power law. The scaling dimensions are continuous function of M/N, and for all the data points, the relation $2\Delta_f + \Delta_b = 1$ is held. The solid curves plot the solution of the scaling dimensions based on Eq. 3.49. In particular, for $M/N = 1$ (the dashed line), the scaling dimensions obtained from both the numerical and analytical solutions match with the prediction from the SUSY SYK model. [32]

Δ_b can be determined by $\Delta_b = 1 - 2\Delta_f$. In particular, for $M/N = 1$, our solution matches with the result of the SUSY SYK model [32], where the model also has $M/N = 1$ and $u < 0$. The numerical solutions of Eq. 3.47,3.48 and analytical solution of Eq. 3.49 are both plotted in Fig. 3.9. With small M/N, Δ_f is approximately $\Delta_f \sim 1/\pi\sqrt{M/N}$.

3.5.7 Discussion of Instabilities

We have demonstrated, through various methods, that the non-Fermi liquid fixed point of the SYK$_4$ model is unstable to a class of marginally relevant four fermion perturbations, and these perturbations drive the system into a non-chaotic state with zero ground state entropy, and spontaneous time-reversal symmetry breaking. Because these perturbations are only marginally relevant, this effect occurs at exponentially low energy scale for a fixed strength of the perturbation. Spontaneous time-reversal symmetry breaking in experimental systems can be probed through Kerr rotation, which has been successfully applied to various condensed matter systems [49, 98, 97, 117]. Similar perturbations (with an opposite sign) can drive the SYK$_q$ model with $q > 4$ to a series of fixed points with continuously varying scaling dimensions.

So far we have ignored the replica index, for instance in Eq. 3.33. We will provide a self-consistent justification for this procedure. The usual argument for ignoring the replica index after disorder averaging the SYK interaction J_{ijkl} is that, the replica off-diagonal terms are subleading in $1/N$ expansion [37]. Here we will investigate the replica index introduced after disorder averaging C_{jk}^a, and we only need to consider the case with

$A \leq 1$, since as we have argued before, the case with $A > 1$ is equivalent to the SYK_4 model.

Starting with the boson-fermion interaction term, $-iuC_{jk}^a b_a \chi_j \chi_k$, reinstating the replica index after disorder-average will lead to the following term

$$\sim -\frac{u^2 J^2}{N^2} \sum_{\alpha, \beta} \int d\tau \int d\tau' \sum_{a=1}^{M} b_\alpha^a(\tau) b_\beta^a(\tau') \left(\chi_j^\alpha(\tau) \chi_j^\beta(\tau') \right)^2. \tag{3.50}$$

In the phase where b_α^a does not condense (corresponds to $u < 0$ in our case), the usual perturbation argument like Ref. [37] will conclude that the replica off-diagonal terms will always make subleading contribution to the partition function compared with the diagonal terms. In the phase with b^a condenses ($A < 1$, $u > 0$), the mean field solution tells us that $\sum_{a=1}^{M} \langle b_\alpha^a(\tau) b_\beta^a(\tau') \rangle$ in Eq. 3.50 is at order of N. Then the perturbation argument will tell us when $u > 0$ and $A < 1$, the contribution from the replica off-diagonal terms is still subleading. Thus for all the main conclusions of this work, we can always make the replica diagonal assumption, and hence ignore the replica index. However, it should be noted that recent work by Ish and Srednicki [42] has provided strong evidence that this argument may not hold for the fermion Greens function. However, even with replica symmetry breaking, they find a spin-glass order that agrees with the predicted properties of our broken $\mathcal{T}$ phase at finite positive u.

3.6   Closing Comments

To summarize, in this chapter we explored the SYK model of a NFL — one of the few solvable models of a NFL phase. We were able to derive and identify numerous interesting features which may generalize to realistic materials. Furthermore, we review the important work published in our paper [7] on the NFL instabilities. Because of the tractability of the SYK model, we were able to identify specific instabilities to broken $\mathcal{T}$ phases at low temperature in the presence of interactions which resemble BCS pair-instabilities. Our work supports the growing set of evidence that some of the exotic and poorly understood characteristics of HTSC are captured by NFL, and potentially SYK-like, physics.

Beyond the details presented in this chapter, we note that the SYK model has lead to multiple interesting theoretical works, exploring constructions of more "realistic" Hamiltonians that aim to embed the features of the NFL phase into finite dimensional, translationally invariant systems. One such class of models are the "Cluster Models", which consider $d-$dimensional lattices whose sites have interacting SYK models. In a work by Song et. al., it was found that a lattice theory of complex fermion SYK models connected by a hopping term resulted in an incoherent metal exhibiting linear temperature resistivity [95] — a defining and theoretically contentious feature of HTSC. Similarly, a Majorana SYK cluster model by Jian et. al. [45] found that the translation ally invariant lattice $u-$perturbed model with inter-site interactions lead to a continuous metal to insulator transition under breaking of $\mathcal{T}$ symmetry.

There have also been a number of works focusing on theoretical exposès of the SYK model, especially on the topic of holography in high energy physics. One interesting result relevant to the breadth of this thesis is the characterization Chaos in the SYK model. It was shown by Maldecena *et. al* [62] that the SYK model saturates the theoretical upper bound of the quantum lypanov exponent $\lambda \leq 2\pi k_n T/\hbar$. The physical interpretation of this result is that SYK-like models are perfect "thermalizers", hence experiencing the fastest possible decoherence at any finite temperature. This result echos the intuition we have about real NFL materials — for example, the strongly dissipative dynamics of HTSCs above the superconducting transition in the strange metal regime.

The insights offered by the SYK model have been enriching for the strongly correlated matter community. It is likely that future work on this model will produce interesting directions of research across a number of disciplines, similar to the seminal and universally acclaimed SK model in classical spin systems.

Chapter 4

Tunable Emergence

So far, we have covered two examples corresponding to special limits of toy correlated fermionic systems — transport and interaction dominated microscopic theories — where, in these cases, small perturbations have lead to phase instabilities of various complexity. The trouble with theory is that small variations in methodological rigor may lead to diverging results, and overlooked details can entirely invalidate applicability. Without verification, a theory has no physical importance. In essence, well-developed quantitative fields of science must have continual feedback between mathematical models that capture the significant aspects of a phenomenon and high-quality experimental data which can differentiate between them. As physicists working in the testable regime of material properties, the importance of experiments cannot be understated– the existence of experiments allows for phenomenology; rather than chase mathematical rigor, an extremely difficult and often fruitless way to work, we can instead make evidence-based guesses

about the mathematical description of a phenomenon and verify our intuition in actual systems.

With this as motivation, in this chapter we will explore the physics of an exciting new class of materials, Magic-Angle Moire Materials (MAMM's), which allow for the probing of strongly correlated fermionic systems to unprecedented depth. Succinctly, MAMMs are van der Waals heterostructures – comprised of two or more vertically stacked monolayers – with relative in-plane twist angles, resulting in a large-scale Moire Pattern. In the regime of small angles and low energy the approximate periodic structure of the Moire superlattice modifies the original band structure by a folding of the Brillouin Zone into minibands, which, at and around a material-dependent "magic-angle", θ_M, become nearly flat. In a simplistic tight-binding picture the bandwidth is roughly proportional to the hopping strength, and therefore these magic-angles correspond to weak transport; hence, such devices exhibit interaction-dominated physics.

In practice, what distinguishes MAMM's from other materials is their tunability: by varying gate voltages, a single sample's phase diagram may be probed across a large region of its parameter space non-destructively. Moreover, as we will discuss, the recent advancement of fabrication techniques for these materials not only allow for the creation of "clean" samples – as confirmed by high carrier mobilities– but also modularity, so that any number of potential components can be assembled into a multilayered system using the same technique. Since phenomenology has proved to be similar across these devices, it becomes possible distinguish material specific effects from universal behavior by sheer

variety.

4.1   A Brief History

Twisted Bilayer Graphene (tBLG) was the first MAMM of wide interest to the correlated electron community. Following the 2004 discovery that graphene monolayers can be obtained from adhesive peeling — first popularized in the use of "scotch tape" on graphite, which later earned the 2010 Nobel prize — a surge of interest in the material lead to experimental and theoretical work on the properties of its monolayered, bilayered, and multilayered derivatives. Exploration of twisted layers first appeared in the literature around 2007; A notable paper by Santos et. al [24], motivated by the empirical observation that Bernal-stacked fabrication methods often resulted in a slightly twisted top layer, gave the first prediction of a reduced fermi-velocity at small twist angles. In 2011 Rafi Bistritzer and Allan MacDonald of University of Texas at Austin published the first theoretical work detailing the plausible existence of flat bands at the charge neutrality point in a small parameter regime of tBLG[8]. Their results were obtained using simple arguments and a continuum model, and they were largely ignored until experimental verification in 2017 by Cao *et. al.* [11]Since then, there has been an explosion of activity into MAMM's both theoretically and experimentally, with over 500 papers on arXiv on the topic.

4.2   Material Details

Twisted Bilayer Graphene was found to be a single material in a class systems, Magic-Angle Moire Materials (MAMM), which share a similar phenomenology: Twisted Bilayer Graphene (TBG), Twisted Double Bilayer Graphene (TDBG), and Trilayer Graphene aligned on one side to hexagonal Boron Nitride (TG/hBN). These materials, and the variations to be discussed, have excellent fabrication yield and tunability. Typical MAMM's are constructed from multiple layers of high-quality graphene monolayers stacked in parallel, capped on one or both ends by flakes of hexagonal Boron Nitride (hBN). The use of hBN is relatively new, being favored for its demonstrated increase in carrier mobility compared to traditional substrates such as silicon dioxide (SiO_2) whose disordering tendencies impact transport via structural inhomogeneity. Unlike typical epitaxially grown crystals, monolayers of MAMM's are held together by weak van der Waals (vdW) forces rather than chemical or ionic bonds. Hence, in practice, experimentalists have direct analogue control over structure and orientation, which is often determined by competing thermodynamic processes over long time-scales in the former. Similarly, during each step of the fabrication process, sample selection and verification by spectroscopic analysis provides a route to stringent quality control as compared to other solid-state material synthesis pathways of complex materials, such as electrochemical crystallization used in organic or high-temperature direct reactions of pressed powder pellets in ceramics and low-dimensional metal oxides.

While MAMM's represent a pinnacle of experimental achievement, it remains impor-

tant to understand the subtleties and limitations of these materials from a conceptual standpoint. For this reason, the remainder of the section will review and summarize seemingly important aspects of MAMM fabrication, structure and probing. Throughout the rest of this section, we will identify possible device imperfections of theoretical interest with an emphasis on details suspect to the literature.

4.2.1 Fabrication Overview

The current standard procedure for fabrication is referred to in the literature as the "dry transfer method", and allows for the creation of clean, precisely aligned multi-layered materials from quality monolayered flakes. For graphene-based structures, the process begins with micro-cleavage by the mechanical exfoliation of graphite and hBN crystals onto SiO_2 substrates. The resulting flakes, which are typically far less than $100\mu m$ in length, are evaluated and selected optically for quality: flake thickness(monolayered), lattice regularity and flake area are the most important factors for selection. Following identification, a commensurately sized non-newtonian polymer stamp attached to a glass base is used to flay hBN flakes from the substrate by vdW forces. After adhering to the surface of the polymer stamp, these are then positioned directly onto the graphene flakes in the desired orientation by a variety of techniques of varying accuracy and scalability. A contact force is applied onto the graphene flake to strengthen the inter-layer vdW adhesion between hBN and graphene. When there is no risk of angular relaxation, the system is heated during this process. Once set, the graphene flake can be peeled
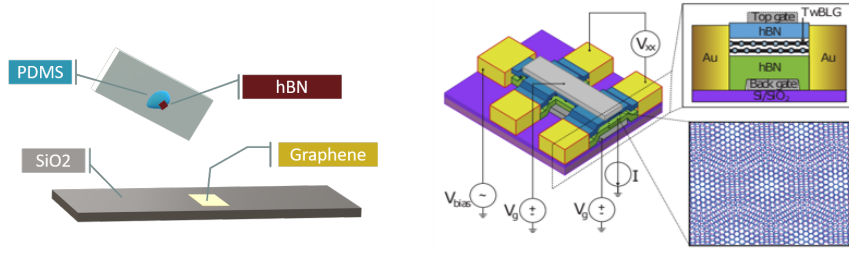
Figure 4.1: Rotations in the BZ mirror the realspace lattice rotations. The result in the case of TBG (above) is that the hybridized bands become flattened in the vicinity of the band crossing points. At magic angles, the band structure becomes almost perfectly flat

from the substrate and the process is repeated as desired. In this way, graphene flakes remain contamination free – they never contact the polymer, thereby limiting the major source of systemic disorder – ultimately allowing for the fabrication of exceptionally clean samples. Once the intended geometry and layer composition has been achieved, additional layers of hBN and/or graphite may be added. The graphite layers not only screen environmental disorder, but also function as a gate electrode to tune electronic densities and displacement fields. The completed stack is then deposited onto a SiO_2 wafer where acid and plasma etching is utilized to shape the sample into a Hall Bar and, if graphite is not applied, expose graphene edges for metal deposition.

The orientation of graphene flakes can be difficult to determine optically– it relies on the identification of typically jagged flake edges as either arm-chair or zigzag. To avoid this issue a further augmentation of this process to aid in precise angular alignments, the so-called "Tear-and-Stack" technique, is now commonly used by many groups. In this version of the procedure, a large, regular, graphene flake is identified after exfoliation. The hBN/polymer stack is then used to tear a region of the flake, while keeping the

relative orientation fixed. Once removed, assuming the stack and original flake have the same orientation, rotating the stack by the desired angle and repeating the process should allow for precise control over relative angles between the monolayers. This angle is verified against theoretical calculations which predict that, at the magic angle, there should be an induced charge density of 4 electrons per moire unit cell [121]

The Hall Bar geometry for the final device is chosen to allow for gate doping of the chemical potential. The four-lead geometry allows for the independent variation of both chemical potential and external displacement field, via the relative strengths of the transverse and in-plane bias volatages, without damaging material integrity.

4.2.2 Twist Angle: Structure and Electronic Properties

When aligned by a relative twist angle θ, two hexagonal lattices can form a periodic Moire superlattice if the twist represents a commensurate rotation. Such angles satisfy the relation

$$\cos(\theta) = \frac{n^2 + 4nm + m^2}{2\left(n^2 + nm + m^2\right)} \tag{4.1}$$

for any integers n, m. The resultant superlattice is described by its superlattice vectors $\vec{t}_1 = n\vec{a}_1 + m\vec{a}_2$ and $\vec{t}_2 = -m\vec{a}_1 + (n + m)\vec{a}_2$, where the $\vec{a}_n$ are the original lattice vectors. The emergent length scale is hence characterized by the wavelength λ_M, is given by the general expression

$$\lambda_M = \frac{a(1 + \delta)}{\sqrt{2(1 + \delta)(1 - \cos\theta) + \delta^2}} \tag{4.2}$$
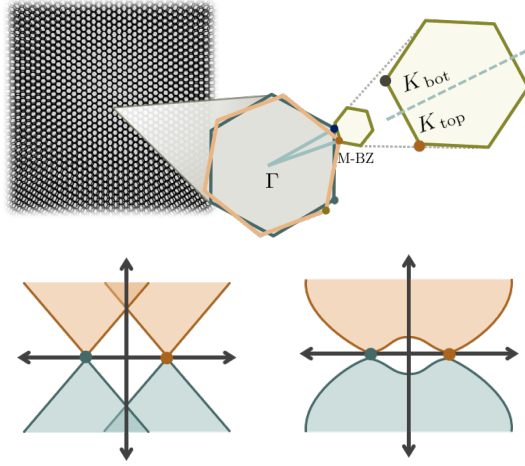
Figure 4.2: Rotations in the BZ mirror the realspace lattice rotations. The result in the case of TBG (above) is that the hybridized bands become flattened in the vicinity of the band crossing points. At magic angles, the band structure becomes almost perfectly flat

where δ is the magnitude of lattice mismatch ($= 0$ for two identical monolayers) and a is the lattice constant of one monolayer, typically chosen to be graphene's [121]. In the case of TBG, $\lambda_M \approx 14$ nm. The periodicity of the superlattice results in minibands that allow for scattering processes between Moire unit cells. More precisely, the Moiré wavevector folds the original wavevectors into the superlattice BZ, resulting in hybridized orbitals as shown in Fig. 4.2. Near the magic angle, the hybridized bands become extremely flat and isolated from the remaining band structure by gaps of approximately 30 meV. In all materials except for TBG, a small gap on the order of a few eV opens between these flat bands.

4.2.3 Known Materials and Properties

We we now attempt to summarize some of the important experimental results in MAMM devices. In this section we will discuss the three most prominent materials in terms of their band structures and their empirically observed phases. A summary of these results is given in Fig 4.3

4.2.4 Twisted Bilayer Graphene (TBG)

Twisted Bilayer Graphene (TBG) was the first MAMM discovered, and thus has the most complete characterization. The band structure of TBG involves the participation of hybridized Dirac cones near the symmetry point of the emergent superlattice, leading to a pair of weakly flat bands near charge neutrality. These bands, while exhibiting no mutal gap, are isolated from the rest of the spectrum by a large gap of approximately 30 meV.

The topology of TBG has been investaged both theoretically as well as experimentally. It has been found that the band topology is trivial in both upper and lower flat bands in ordinary TBG. More recent studies have shown that when TBG is aligned to hBN on one side, thus breaking the out-of-plane mirror symmetry, these bands pick up equal and opposite Chern number $C = \pm 1$ [126]

Experimental studies have provided evidence for multiple strongly correlated phases at various tunings. About charge neutrality, the presence of Mott insulating phases is revealed for fractional filling $\delta_f = \pm\frac{1}{2}$. More Mott states can be found at $\delta_f = +\frac{1}{4}, -\frac{3}{4}$
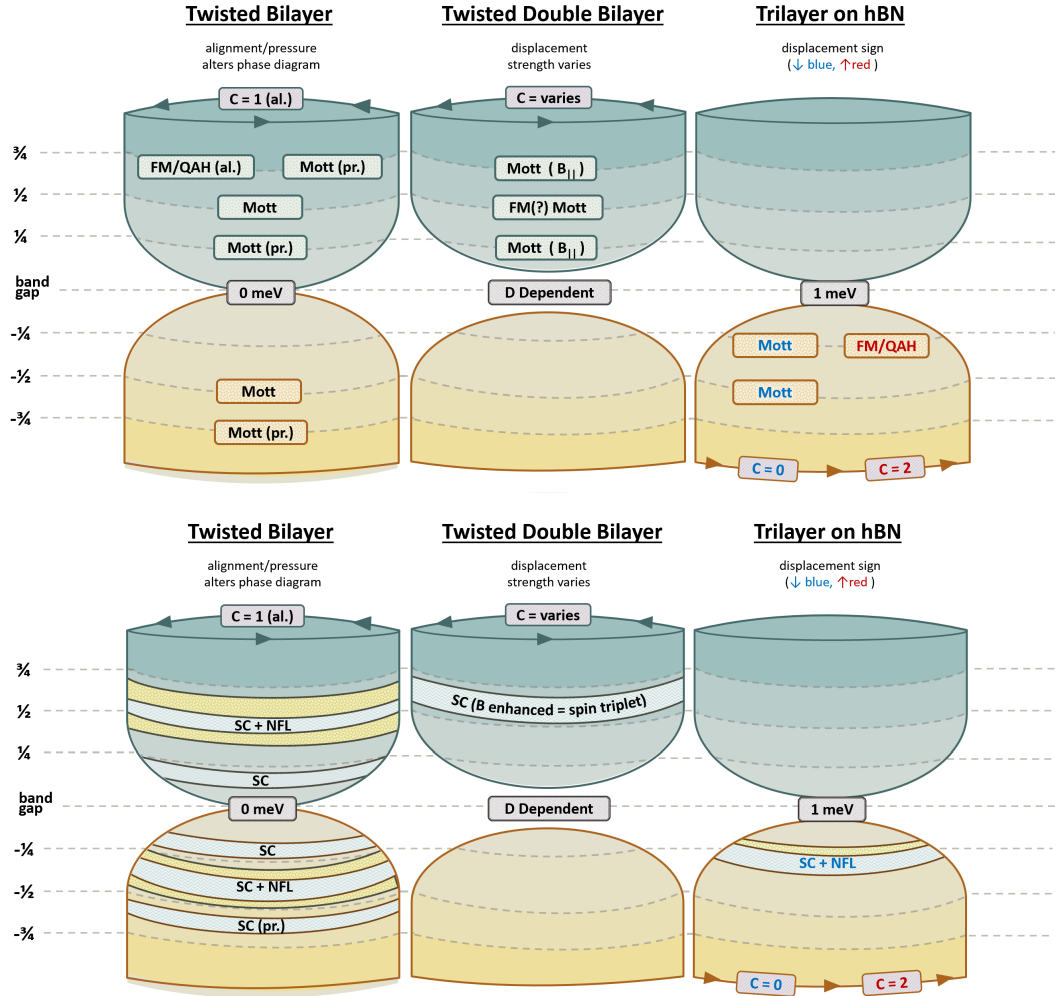
Figure 4.3: A Summary of Notable results in MAMM systems. Despite differences in the geometry, symmetry and construction of each device, we see similar phenomenology across the phase diagrams. All three material classes have correlated insulator phases that have low temperature instabilities to Superconductivity and other exotic correlated states. All three devices share the common feature of exceptionally flat bands about charge neutrality which are separated from the remainder of the band structure by large gaps.

under the application of pressure to TBG [120]. Interestingly, these insulating phases seem to neighbor unconventional superconducting orders at low temperatures, with such transitions happening near the fractional fillings $\delta_f = \pm\frac{1}{2} \pm \epsilon, +\frac{1}{4} - \epsilon, -\frac{1}{4} + \epsilon$ for ϵ a small perturbation of the chemical potential. Similarly, aligned TBG/hBN has additional

phases including an apparent Quantum Anomalous Hall at $\delta_f = +\frac{3}{4}$ [92]

4.2.5 Twisted Double Bilayer Graphene (TDBG)

Twisted Double Bilayer Graphene (TDBG) typically involves a two Bernal-stacked bilayer graphene layers rotated by a relative angle. Since these systems have a quadratic band crossing point, their hybridized band structure results in much flatter bands without fine tuning. They also have an additional dependence on external displacement field, which biases the relative doping between upper and lower flat bands. These devices are characterized by flat isolated bands around charge neutrality, with a small, displacement dependent mutual gap on the order of 1-5 eV. Furthermore, it is unclear if the upper and lower bands carry a finite Chern number, which is expected to depend on the size of the applied displacement field.

Evidence of spin-triplet pairing (predicted previously [118] in a model to be reviewed in section 4.3) was found in TDBG [74, 58]. The insulating phase appearing near $\delta_f = +\frac{1}{2}$ appears to be a ferromagnetic correlated insulator at half filling away from charge neutrality was discovered in the same system [93].

In TDBG, besides clear ferromagnetism signature observed at the 1/2-filling insulator [74, 93, 58], it was also observed that correlated insulators at 1/4 and 3/4 fillings emerge under in-plane magnetic field [58], whose main effect is likely a spin-polarizing Zeeman effect. This observation implies that the TDBG at 1/4 and 3/4 filling is rather close to a ferromagnetic correlated insulator, and a Zeeman field would drive a metal-insulator

transition. Near the Mott insulating phase, superconducting order was discovered at $\delta_f = +\frac{1}{2} + \epsilon$, with the strange property of being enhanced, rather than suppressed by an in-plane magnetic field. This observation support the previous evidence of a FM insulator at half-filling, and prompts immediate investigation into the possible mechanism leading to this highly unconventional pairing.

4.2.6 Trilayer Graphene on hBN (TTG)

Unlike the previously mentioned materials in this section, Trilayer graphene on hBN (TLG/hBN) is not a "twisted" material, but exhibits many of the same properties as TBG and TDBG — namely, flat band physics giving rise to a series of correlated insulator states neighboring low-temperature transport dominated orders. TLG/hBN's bandstructure, in addition to the large isolating gap, features a mutual gap of approximately 1 meV about charge-neutrality. Due to the hBN, it does not retain the out-of-plane mirror symmetry, and the emergent physics depends on the sign of the external displacement field applied.

The correlated insulator phases are found in the hole-doped band below charge neutrality, where unidentified Mott insulating phases have been found at $\delta_f = -\frac{1}{4}, -\frac{1}{2}$ under a negative signed displacement field. When the direction of the displacement field is reversed, there has been evidence that the correlated insulator found at $\delta_f = -\frac{1}{4}$ is again a Quantum Anomalous Hall, similar to the reported findings of TBG/hBN above. These observations appear to match theoretical predictions of band topology, which have suggested that under a positive-signed displacement the lower band develops a nontrivial

$C = 2$ [15].

4.2.7 Possible Issues

We now make some cautionary comments about the nature of these materials prior to theoretical discussion. Despite the exellent mobility and yeild of the fabrication method, there are a number of effects that should be, in the very least, considered when constructing models to understand the growing collection of data about these devices.

In the case of TBG, when the sublattice symmetry of the underlying graphene lattice is not broken, naive analysis results in additional secondary Dirac points in the conduction and valence bands at $E = 2\pi\hbar v_f / \sqrt{3}\lambda_M$. However, especially in hetero-structures containing hBN layers, it has been reported that sublattice symmetry is in fact broken by structural relaxation, such as trigonal warping. Such out-of-plane straining ultimately opens band gaps at the primary and secondary Dirac Points in the valence band (with reported values at the primary Dirac Point up to 40meV). Additionally, broken mirror symmetry due to hBN on one side leads to complex dependence on external displacement fields, as observed TBG/hBN and TLG/hBN.

Furthermore, the "twist angle" is not an exact quantity — it is a spatially averaged representation of the relative angle of the two layers at all points in space. It has been argued in a theoretical work that as little as 10% twist angle disorder can fill the isolating gap [112], hence reducing the strength of the insulating phase (it increases miniband width t). Similar accounts of this disorder have appeared in numerous experimental

works where it was found that the superconducting transition had an onset similar to a disorder induced percolation transition [120], as well as resistance which scales with temperature following a variable-ranged hopping law $R \sim A \exp(kT^{-1/3})$

Ignoring disorder, the macroscopic twist angle itself is difficult to verify spectroscopically. Indirect verification of this angle are model dependent, typically relying on charge density measurements. This issue is amplified in materials where there are nearby rotational configurations, such as a Bernal Stacked geometry, which are thermodynamically preferred.

4.3   A Minimal Theory

Even in the ideal limit of a disorder and strain free lattice, a first principles derivation of MAMM band structures are incredibly difficult. As mentioned, the Moire unit cell contains on the order of 10^8 electrons, with spatially varying inter-layer coupling constants. That MacDonald's phenomenological calculation was able to reveal the existence of flat bands in the small twist angle regime, with a precision of ± 0.05deg is ubiquitously considered miraculous. This calculation, however, which analyzes *only* only electronic transport properties of TBG in a continuum model cannot be easily extended to treat the interactions that become increasingly important as the miniband-width $\sim t$ shrinks near θ_M. In order to develop a more complete theory of MAMM's, models must be developed that allow for electron-electron interactions which respect the important properties of these systems. While there are numerous papers which have approached a

first-principles construction of appropriate Wannier orbitals for advanced theory, we will not discuss their details and direct the interested reader to these publications.

To circumvent complexity, it is easier to concentrate on the mesoscopic physics using phenomenology derived from empirical observations about MAMMs. In early experiments on TBG, it was shown that electron density localizes about the AA stacking regions, which represent a triangular super-sublattice on the scale of $\lambda_M(\theta_M)$. Interested primarily in the band-enhanced interactions, we note that they will be most significant in spatial regions of high electron density. Furthermore, given the empirically observed localization, the weak transport terms must become most important at these AA regions. It then seems reasonable to assume that the interesting physics likely arises from the scattering and interaction of charge carriers between these regions. Using this intuition, one can consider a phenomenological effective model on the triangular lattice that is appropriate near θ_M and charge-neutrality.

Such an effective theory was proposed by Xu and Balents [118], and it will represent the starting point of the remaining works presented. In their construction, they made three further assumptions:

1. Valley mixing is prohibited, which is expected given their large momentum separation in comparison to inter-site scattering.

2. At very low temperatures, the relevant bandwidth is very small and it is appropriate to represent each region by a single "site". Given the weakness of the transport, in the absence of inter-band mixing, a tight binding model need only consider

nearest-neighbor hopping between distant AA regions. In this regime valley symmetry is preserved, as can be shown by combinations of reflection and time-reversal symmetries in the mini-Brillouin Zone (mBZ).

3. Hopping and interaction have a four-fold flavor degeneracy with respect to single-particle states– these flavors arise from a two-fold valley degeneracy from the hybridization of the bilayer cones and a spin degeneracy enforced by spin-rotation invariance.

Their proposed model is an $SU(4)$ invariant Hubbard Model on the triangular sublattice of tBLG:

$$H = -t \sum_{\langle ij \rangle} c_{i\alpha}^\dagger c_{i\alpha} + U \sum_i \left(\sum_\alpha^4 n_{i\alpha} \right)^2 \tag{4.3}$$

where t is the hopping strength, U the Hubbard repulsion and the greek subscripts sum over the 4 fermion flavors(2 spin and 2 valley degrees of freedom) Like the $SU(2)$ case, we expect that at large U/t and fractional filling, the system should become a Mott insulator. In this limit, one may use standard perturbation theory in powers of t/U to derive an effective $SU(4)$ Heisenberg Hamiltonian:

$$H_J = J \sum_{\langle ij \rangle} \sum_{a=1}^{15} \hat{T}_i^a \hat{T}_j^a \tag{4.4}$$

where we have employed the $SU(N)$ spin representation of fermions,$\hat{T}_i^a = c_{i\alpha}^\dagger \hat{T}_{\alpha\beta}^a c_{i\beta}$, detailed in Chapter 2. The matrix generators of SU(4), T^a, have the normalization $\mathrm{Tr} T^a T^b = 4\delta^{ab}$. Following the same reasoning presented in Chapter 3, we will again

rewrite this model in terms of particle-particle channels using Fierz Transformations:

$$H_J = J \sum_{\langle ij \rangle} \left[-\frac{5}{4} \left(\vec{\Delta}_{ij} \right)^\dagger \cdot \vec{\Delta}_{ij} + \frac{3}{4} \left(\Delta_{ij}^- \right)^\dagger \cdot \Delta_{ij}^- \right] \tag{4.5}$$

The Feirz transformation results in two vector order parameters which can be classified by their symmetry under site exchange. The symmetric $\vec{\Delta}_{ij} = \vec{\Delta}_{ji}$ is a 6-component vector is of the form:

$$\vec{\Delta}_{ij} = c_i^t (\sigma^3 \tau^2, i\sigma^0 \tau^2, \sigma^1 \tau^2, i\sigma^2 \tau^3, \sigma^2 \tau^0, i\sigma^2 \tau^1) c_j. \tag{4.6}$$

We see that three terms correspond to valley-singlet spin-triplet pairings, and the remaining three valley-triplet spin-singlet. The anti-symmetric $\vec{\Delta}_{ij}^- = -\vec{\Delta}_{ij}^-$ are 10 component vectors which may be ignored for our concerns; the form of (4.5) favors condensation of $\vec{\Delta}_{ij}$, so that the symmetric fields should strongly control the physics near half-filling. In this form, we see that the $SU(4)$ symmetry is broken down to $SU(2) \times SU(2)$ in the valley and spin subspaces. We now consider a physically relevant perturbation which will further reduce the effective symmetry of the model. Let us write down the simplest Hund's coupling interaction in the system, which acts between two AA sites:

$$H_h = -V \sum_j \left(\vec{S}_j \right)^2 \tag{4.7}$$

One may check that this term favors the spin-triplet pairing fields. Given the reduced model, one can now analyze the properties of the superconducting phase. Within the BCS framework, we may write down a general ansatz for the order parameter:

$$\vec{\Delta}_k = \left(u_k \vec{\Phi}_1 + v_k \vec{\Phi}_2 \right) \cdot i\sigma^2 \vec{\sigma} \tau^2 \tag{4.8}$$

$$u_k = \cos(k_x) - \cos(k_x/2)\cos(\tfrac{\sqrt{3}}{2}k_y) \text{ and } v_k = \sqrt{3}\sin(k_x/2)\sin(\tfrac{\sqrt{3}}{2}k_y)$$

$$\begin{aligned} A: \quad & \vec{\Phi}_2 = i\vec{\Phi}_1 = i\phi e^{i\theta} \\ B: \quad & \vec{\Phi}_1 = \phi_1 e^{i\theta}, \quad \vec{\Phi}_2 = \phi_2 e^{i\theta} \end{aligned} \tag{4.9}$$

It can be shown that both type A and B superconductors are topological. Type A results in a $\mathcal{T}$ broken half-vortex excitation and carries a quantized magnetic flux $\Phi_0 = \frac{hc}{4e}$, undergoing an order-to-disorder transition — via vortex unbinding — at any finite temperature due to the Mermin-Wagner theorem. Because of this, the phase has no true long-range order, and is instead characterized by powerlaw correlations of a spin-singlet charge $4 - e$ quasiparticle. When comparing the relative strengths of the these order parameters, they found that spin-triplet superconductivity was favored. Type B preserves $\mathcal{T}$ and is also disordered by any finite temperature, with the ordered phase leading to four counter-propagating non-chiral Majorana edge states. These channels imply the lack of a thermal Hall effect and a low-temperature spin-triplet $d\pm id$ topological superconducting state. By mean-field analysis, it was argued that the type B order parameter, and hence, a spin-triplet superconducting state, would be favored. This was later evidenced by multiple experiments in TDBG, and is the topic of the next section.

4.4   Ferromagnetism and Spin-Valley Liquids

Continuing the discussion on experimental results, in 2019 multiple experiments on TDBG found evidence of a ferromagnetic correlated insulator at half-filling away from

charge neutrality. Under an in-plane magnetic field, signatures of correlated insulator physics where also observed at 1/4 and 3/4 filling. Similar signatures of ferromagnetism were found in Trilayer Graphene earlier that year. Moreover, the superconducting state of TDBG was found ot be enhanced by a perpendicular field, indicating the possibility that the SC state is spin-triplet itself, as predicted by the model of Balents and Xu.

Motivated by these experiments, in this work we investigate a quantum spin-valley model on the triangular lattice with one fermion per site, which corresponds to either 1/4 filling or 3/4 filling on the Moir$\vec{e}$ superlattice. The Hamiltonian of this model reads

$$H = \sum_{<i,j>} \sum_{a,b=1}^{3} J T_i^{ab} T_j^{ab} + J^s \sigma_i^a \sigma_j^a + J^v \tau_i^b \tau_j^b, \tag{4.10}$$

where σ^a and τ^b are Pauli operators in the spin and valley spaces, and $T^{ab} = \sigma^a \otimes \tau^b$. When $J^s = J^v = J$, this model becomes the SU(4) quantum antiferromagnetic model with fundamental representation on each site. The SU(4) symmetry is broken by the Hund's coupling [118], which in general makes $J^v > J > J^s$, if we choose the standard sign of the Hund's coupling which favors large spin on each site. But we assume that the SU(4) breaking effect is not strong enough to change the sign of J^s, J^v and J, namely we keep all three coupling constants positive, *i.e.* antiferromagnetic. Indeed, since the Hund's coupling originates from the exchange coupling which involves overlap between wave functions at the two valleys, the Hund's coupling should be a relatively weak effect since the inter-valley wave function overlap is expected to be small because large momentum transfer between the two valleys is suppressed by the long wavelength

modulation of the Moiré superlattice. For simplicity we ignore other mechanisms that break the SU(4) symmetry, such as valley-dependent hopping [79], hence in the spin-valley model Eq. 4.10 the valley space has its own $SU(2)^v$ symmetry.

A consensus of the mechanism for the observed insulator and superconductor has not yet been reached. The minimal two-orbital extended Hubbard model on the triangular lattice reviewed above Ref. [118], at least describes the trilayer graphene and hexagonal BN heterostructure (TLG/h-BN) [14, 16], as well as the twisted double bilayer graphene (TDBG) [74, 93, 58] with certain twisted angle and out-of-plane electric field (displacement field), since in these cases there is no symmetry protected band touching below the fermi energy, and the isolated narrow band has trivial quantum valley topological number [79, 125, 127, 17, 59, 57]. This minimal model would then naturally predict either a spin-triplet [118] or spin-singlet [23] $d + id$ topological superconductor, depending on the sign of the on-site Hund's coupling.

4.4.1 The Spin-Valley model

A reasonable question to ask is how a microscopic Hamiltonian with fully anti-ferromagnetic couplings may give rise to ferromagnetism, a phenomenon which is surprising rare in real materials. To investigate the possible origin, we may start from the model detailed in section 4.3, where it was shown that Hund's coupling should favor a spin-triplet pairing by general arguments. To strengthen the proposed scheme, we can perform pertubation theory in t with full consideration of this Hund's term. Hence, we now study the full

Hamiltonian:

$$H_{\text{tot}} = -t \sum_{\langle ij \rangle} c_{i\alpha}^\dagger c_{i\alpha} + U \sum_i \left(\sum_\alpha^4 n_{i\alpha} \right)^2$$
$$- V \sum_j \left[\left(c_j^\dagger \vec{\sigma} c_j \right) \cdot \left(c_j^\dagger \vec{\sigma} c_j \right) \right]^2 - \left[\left(c_j^\dagger \vec{\tau} c_j \right) \cdot \left(c_j^\dagger \vec{\tau} c_j \right) \right]^2 \qquad (4.11)$$

We follow the standard approach of degenerate perturbation theory. At quarter-filling, the ground state of $H_U + H_V$ has precisely one electron per site, and the projection operator to the ground state manifold reads

$$\mathcal{P} = \prod_j (-1) \frac{1}{6} n_j (n_j - 2) (n_j - 3) (n_j - 4). \qquad (4.12)$$

Considering any pair of nearest neighbor sites on the Moiré superlattice, the ground state manifold can be further divided into four sectors which correspond to spin-singlet/triplet and valley-singlet/triplet states. We can write

$$\mathcal{P} = \mathcal{P}_{ss} + \mathcal{P}_{st} + \mathcal{P}_{ts} + \mathcal{P}_{tt}, \qquad (4.13)$$

where (for example) $\mathcal{P}_{st}$ means the projection to spin-single/valley-triplet states. The effective Hamiltonian can be calculated as

$$H_{\text{eff}} = \mathcal{P} H_t \frac{1}{E_0 - H_U - H_V} H_t \mathcal{P}, \qquad (4.14)$$

where E_0 is the ground state energy for the two-site problem. A detailed analysis of the intermediate states considering the virtual hopping process can be found in Ref. [118]. We find that only $\mathcal{P}_{st}$ and $\mathcal{P}_{ts}$ contribute to the effective Hamiltonian which takes a

diagonal form in this basis

$$H_{\text{eff}} = -\frac{2t^2}{U+4V}\mathcal{P}_{st} - \frac{2t^2}{U-4V}\mathcal{P}_{ts}.$$ (4.15)

Rewritten in terms of the SU(4) generators on the nearest neighbor sites, the effective Hamiltonian is equivalent to the spin-valley model Eq. 4.10 with the coupling constants given by

$$
\begin{aligned}
J^s &= J - \frac{t^2}{U}\left(\frac{2V}{U} + O\left(\frac{V}{U}\right)^2\right), \\
J^v &= J + \frac{t^2}{U}\left(\frac{2V}{U} + O\left(\frac{V}{U}\right)^2\right), \\
J &= \frac{t^2}{4U}\left(1 + O\left(\frac{V}{U}\right)^2\right).
\end{aligned}
$$ (4.16)

There is a Z_2 symmetry regarding the sign of the Hund's coupling. The coupling constants transform as $J^s/J \leftrightarrow J^v/J$ when we change $V \leftrightarrow -V$, as is naturally expected from the form of the Hund's coupling.

The final result gives

$$H = \sum_{\langle ij \rangle} J T_i^{ab} T_j^{ab} + J^s \sigma_i^a \sigma_j^a + J^v \tau_i^a \tau_j^a$$ (4.17)

with

$$
\begin{aligned}
J &= \frac{t^2}{4U}\left[1 + O\left(\frac{V^2}{U^2}\right)\right] \\
J^s &= \frac{t^2}{4U}\left[1 - \frac{8V}{U} + O\left(\frac{V^2}{U^2}\right)\right] \\
J^v &= \frac{t^2}{4U}\left[1 + \frac{8V}{U} + O\left(\frac{V^2}{U^2}\right)\right]
\end{aligned}
$$ (4.18)

4.4.2 The $\text{FM} \otimes 120°$ state

The above derivation should be considered a proof of principle for the form of the Hamiltonian rather than a rigorous derivation. The model of section 4.3 is itself a phenomenological one, who's coupling constants and interaction form is not immediately related to the underlying microscopic theory. In fact, many simplifying assumptions, including the importance of further hopping terms, are still unresolved. Similarly, in this model, it is best to forget the symbolic origins of J^s and J^v, since in a real material system many factors could contribute to their values. This derivation serves only to point out that given the basic ingredients of a Hubbard-like model and a symmetry breaking Hund's term that favors triplet formation, this effective model can be justified.

Having stated our priors, we now treat J^v, J^s and J as quasi-independent, only noticing that Hund's coupling favors a weaker spin interaction and a stronger valley interaction. Under the stronger assumption that $J^v \gg J \gg J^s$, it is simple to argue that the ground state should be a $\text{FM} \otimes 120$ state. At least in certain limit, $i.e.$ $J^v \gg J \gg J^s > 0$, it is fairly easy to see why ferromagnetism would emerge in model Eq. 4.10 with all antiferromagnetic coupling constants. First of all, the following state will always be an eigenstate of the Hamlitonian:

$$|\Psi_{\text{FM}}\rangle = \left(\prod_i |\sigma_i^z = +1\rangle \right) \otimes |\text{AF of } \vec{\tau}_{\{i\}} \, \rangle. \tag{4.19}$$

This state is a direct product of two parts: the first part is a fully-polarized ferromagnetic state of the spin $\vec{\sigma}_i$ space; the second part is the ground state of the nearest-neighbor antiferromagnetic quantum Heisenberg model on the triangular lattice in the $\vec{\tau}_i$ space. Although we cannot write down the explicit form of the exact microscopic wave-function |AF of $\vec{\tau}_{\{i\}}$ ⟩, we do know that this state has a 120° antiferromagnetic order with reduced moment due to quantum fluctuation and geometric frustration. This state Eq. 4.19 is always the eigenstate of Eq. 4.10 because a fully polarized ferromagnetic spin state is the eigenstate of operator $\vec{\sigma}_i \cdot \vec{\sigma}_j$ on every link $< i, j >$. Then in the limit of $J^v \gg J \gg J^s > 0$, this eigenstate $|\Psi_{\mathrm{FM}}\rangle$ is also the ground state, because intuitively on every link the spin $\vec{\sigma}_i$ will see a background "effective" ferromagnetic coupling

$$J_{\mathrm{eff}} = J^s + J\langle \vec{\tau}_i \cdot \vec{\tau}_j \rangle. \qquad (4.20)$$

Because $\langle \vec{\tau}_i \cdot \vec{\tau}_j \rangle < 0$ for the 120° state of $\vec{\tau}_i$, for large enough J the spins will see an effective ferromagnetic coupling, even though in the original model Eq. 4.10 all the couplings are antiferromagnetic.

With a fixed large J^v, while increasing J^s, eventually $J\langle \vec{\tau}_i \cdot \vec{\tau}_j \rangle$ will not be strong enough to overcome the antiferromagnetic coupling J_s, hence we expect to see a transition from the "FM $\otimes$ 120°" state to another state without ferromagnetic order. Numerically [6], $\langle \vec{\tau}_i \cdot \vec{\tau}_j \rangle$ is found to be ~ -0.73 for the triangular lattice quantum antiferromagnet. If we evaluate the energy of $|\Psi_{\mathrm{FM}}\rangle$ in Eq. 4.19, while increasing J_s/J, this state is no longer the ground state when $J_s/J > 0.73$. Hence the intuitive argument gives an upper bound for the transition point of J^s/J.
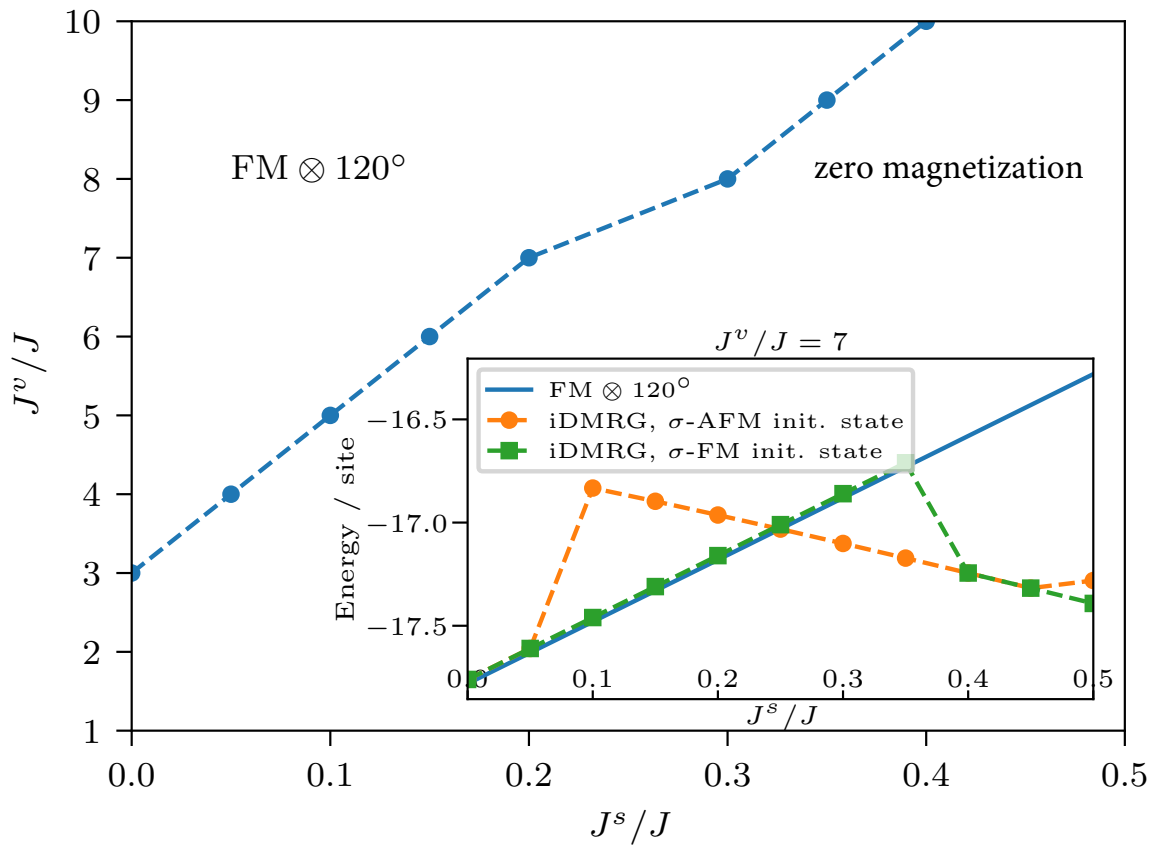
Figure 4.4: Phase boundary of the FM ⊗ 120° state obtained using DMRG on infinite cylinders with circumference $L_y = 6$. The inset shows the energy per site obtained for $J^v/J = 7$ as function of J^s/J. Green squares (orange circles) indicate the energies obtained using iDMRG when the spins are initialized in a FM (AFM) product state. The solid blue line indicates the energy expected for the FM ⊗ 120° state.

4.4.3 DMRG simulation of the spin-valley model

We now provide numerical evidence for the fact that the FM $\otimes$ 120° state is the ground state in the $J^v \gg J \gg J^s$ limit and obtain the phase boundary of this state. To this end we use the density matrix renormalization group (DMRG) method [111, 89]. We note that in finite systems, boundaries can introduce strong oscillations in the expectation value of $\langle \vec{\tau}_i \cdot \vec{\tau}_j \rangle$ on nearest-neighbor bonds (which are expected to be uniform when the valley degree of freedom is in the 120° state), and thus affect the effective coupling seen by the spins. To avoid such boundary effects we use infinite DMRG [63]. To observe uniform bond expectation values when the valley degree of freedom is in the 120° state wide enough cylinders have to be considered. We perform our analysis on cylinders of circumference $L_y = 6$, for which we obtain mean bond expectation value $\langle \vec{\tau}_i \cdot \vec{\tau}_j \rangle \approx -0.74$, consistent with Ref. [6], with spatial variations below one percent.

For our numerical simulations we use the ITensor library [1]. We assume a 3-site unit cell along the cylinder to allow for the formation of a 120° state in the valley and/or spin degrees of freedom. The valley degree of freedom is initialized in the total $\tau^z = 0$ sector and τ^z quantum number conservation is used. The spin degree of freedom is initialized either in the fully polarized state, or a classical anti-ferromagnetic state with total $\sigma^z = 0$. The maximal bond dimension in our simulations is $M = 1000$.

We find that at large J^v and small J^s, the system indeed converges to a *fully polarized* spin-FM and a 120°-valley ordered state, independent of the initial conditions. At larger J^s we observe a state *without any net magnetization*. At this stage we cannot conclude as

to the nature of the entire region with zero magnetization (with larger J^s and $J^s < J$, for the total $\sigma^z = 0$ sector and going to bond dimensions of up to 4000 we have not identified a clear order for the spin degree of freedom), but in the next section we will propose some possible interesting liquid states and topological orders for this region of phase diagram. The ground state energy obtained using iDMRG for a fixed $J^v/J = 7$ as function of J^s, for the two initial states, is shown in the inset of Fig. 4.4. The solid blue line on the same plot indicates the energy expected for the FM $\otimes$ 120° state, calculated using a uniform bond expectation value $\langle \vec{\tau}_i \cdot \vec{\tau}_j \rangle \approx -0.74$ that we obtain for the 120° state on infinite cylinders of circumference $L_y = 6$ as mentioned above. We estimate the position of the phase boundary for each J^v/J to be at the J^s/J for which the lowest energy obtained using iDMRG drops below the one expected for the FM$\otimes$120° state. The resulting phase boundary as function of J^v/J and J^s/J is shown in the main Fig. 4.4. Our results for the ground state energy and the magnetization across the phase boundary both suggest that the transition between the ferromagnetic order and the paramagnet is a first order level-crossing.

4.4.4 Schwinger boson analysis

We can also construct the FM $\otimes$ 120° state using the Schwinger boson formalism. We first define a four component Schwinger boson $b_{j,\alpha}$ on every site which forms fundamental representation under both the spin and valley SU(2) symmetry, and also a fundamental representation of the enlarged SU(4) symmetry. The Schwinger boson Hilbert space is

subject to a local constraint

$$\sum_{\alpha=1}^{4} b_{j,\alpha}^{\dagger} b_{j,\alpha} = \kappa. \tag{4.21}$$

Physically $\kappa = 1$, but in the Schwinger boson mean field calculation κ is often treated as a tuning parameter. The Hamiltonian Eq. 4.10 can be reorganized into the following form:

$$
\begin{aligned}
H &= J_{ts} \left(\vec{\Delta}_{ij}^{ts\dagger} \cdot \vec{\Delta}_{ij}^{ts} \right) + J_{ss} \left(\Delta_{ij}^{ss\dagger} \Delta_{ij}^{ss} \right) \\
&+ J_{st} \left(\vec{\Delta}_{ij}^{st\dagger} \cdot \vec{\Delta}_{ij}^{st} \right) + J_{tt} \mathrm{tr} \left(\Delta_{ij}^{tt\dagger} \cdot \Delta_{ij}^{tt} \right).
\end{aligned}
\tag{4.22}
$$

The operator $\vec{\Delta}_{ij}^{ts}$ and $\vec{\Delta}_{ij}^{st}$ are the spin-triplet/valley-singlet, and spin-singlet/valley-triplet pairing operator between Schwinger boson b_{α} on site i, j:

$$\left(\vec{\Delta}_{ij}^{ts}, \vec{\Delta}_{ij}^{st} \right) = b_i^t \left(\mathrm{i}\sigma^{32}, \sigma^{02}, \mathrm{i}\sigma^{12}, \sigma^{23}, \mathrm{i}\sigma^{20}, \sigma^{21} \right) b_j, \tag{4.23}$$

where $\sigma^{ab} = \sigma^a \otimes \tau^b$, $\sigma^0 = \tau^0 = \mathbf{1}_{2\times2}$. Then Δ^{ss} and Δ^{tt} are the singlet/singlet, and triplet/triplet pairing respectively, for example $\Delta_{ij}^{ss} = b_i^t \sigma^{22} b_j$.

In Eq. 4.22,

$$
\begin{aligned}
J_{ts} &= -\frac{1}{4}(3J_v + 3J - J_s), \quad J_{st} = -\frac{1}{4}(3J + 3J_s - J_v), \\
J_{ss} &= \frac{3}{4}(3J - J_s - J_v), \quad J_{tt} = \frac{1}{4}(J + J_s + J_v).
\end{aligned}
\tag{4.24}
$$

With the most natural parameter region $J_v > J > J_s > 0$, J_{ts} is always negative, and it corresponds to the strongest mean field channel, while none of the other parameters are guaranteed to be negative (for example J_{tt} is always positive). Thus for the purpose of

110

mean field analysis, we will just keep the first term of Eq. 4.22, and ignore all the rest three terms of Eq. 4.22. The mean field Hamiltonian reads

$$
\begin{aligned}
H_{\text{MF}} &= \sum_{ij} J_{ts} \left(\vec{\phi} \cdot \vec{\Delta}_{ij}^{ts} + H.c. \right) - J_{ts} |\vec{\phi}|^2 \\
&+ \sum_{j} \mu (\sum_{\alpha=1}^{4} b_{j,\alpha}^{\dagger} b_{j,\alpha} - \kappa),
\end{aligned}
\tag{4.25}
$$

where $\vec{\phi}$ is a complex vector under $\text{SU}(2)^s$. Here we choose a uniform ansatz of $\vec{\phi}$ on the entire lattice, and all the links i, j are included in the sum with the convention $j = i + \hat{e}$ with $\hat{e} = (1, 0), (-1/2, \pm\sqrt{3}/2)$, $i.e.$ the mean field ansatz explicitly preserves the translation and rotation by $2\pi/3$ symmetry of the triangular lattice, while all the crystal symmetries are preserved as projected symmetry group (PSG). μ is another variational parameter of the mean field calculation which guarantees that the filling of Schwinger boson is fixed at κ on every site.

The $\text{FM} \otimes 120°$ ordered state corresponds to the mean field ansatz with $\vec{\phi} = \vec{\phi}_1 + i\vec{\phi}_2$, and the real vectors $\vec{\phi}_1$ and $\vec{\phi}_2$ *orthogonal* with each other. For example, when $\vec{\phi} = \phi(1, i, 0)$, only the spin-up ($\sigma^3 = +1$) Schwinger bosons participate in this mean field analysis. The ferromagnetic order parameter corresponds to the following gauge invariant quantity:

$$
\vec{M} \sim i\vec{\phi} \times \vec{\phi}^* \sim \vec{\phi}_1 \times \vec{\phi}_2.
\tag{4.26}
$$

With only spin-up Schwinger bosons, the mean field calculation reduces precisely to the $\text{SU}(2)$ spin-1/2 Heisenberg model on the triangular lattice [83] with Heisenberg

coupling $J_{ij} = -4J_{ts}$ (The $\mathrm{Sp}(N)$ Heisenberg model defined in Ref. [83] has Hamiltonian $H = \sum_{i,j} -\frac{1}{2N} J_{ij} \Delta_{ij}^\dagger \Delta_{ij}$ where Δ_{ij} is the $\mathrm{Sp}(N)$ singlet pairing between Schwinger bosons on sites i, j):

$$
\begin{aligned}
H_{\mathrm{MF}} &= \sum_{ij} J_{ts} \left(2\phi \, b_{\uparrow,i}^t \mathrm{i}\tau^2 b_{j,\uparrow} + H.c. \right) - 2J_{ts}\phi^2 \\
&+ \sum_j \mu (\sum_{\alpha=1}^2 b_{j,\uparrow,\alpha}^\dagger b_{j,\uparrow,\alpha} - \kappa).
\end{aligned}
\tag{4.27}
$$

Because the spin-down Schwinger bosons do not contribute to the mean field decomposition when $\vec{\phi} \sim (1, \mathrm{i}, 0)$, we replace the constraint in Eq. 4.21 by $\sum_{\alpha=1}^2 b_{j,\uparrow,\alpha}^\dagger b_{j,\uparrow,\alpha} = \kappa$ in Eq. 4.27. Now technically the mean field theory Eq. 4.27 corresponds to the "zero-flux state" in Ref. [110], which has lower mean field energy than other mean field ansatz [110] for this nearest neighbor model, and it makes the minima of the Schwinger boson band structure locate at the corner of the Brillouin zone $\vec{Q} = (\pm 4\pi/3, 0)$. The mean field solution gives $\mu > 0$, which is consistent with the fact that we set $\sum_{\alpha=1}^2 b_{j,\downarrow,\alpha}^\dagger b_{j,\downarrow,\alpha} = 0$. And at the mean field level, when the filling of the Schwinger boson κ is greater than 0.34 [83], b_α condenses, which leads to a fully polarized FM in the spin space, and also 120° state in the valley space.

If the mean field value of $\vec{\phi}$ is real (or equivalently if $\vec{\phi}_1$ is parallel to $\vec{\phi}_2$, for example, $\vec{\phi} \sim \phi(0, 0, 1)$, both spin-up and spin-down Schwinger bosons participate in the mean field analysis, and the mean field analysis is technically equivalent to the calculations in Ref. [83] for the $\mathrm{Sp}(2) \sim \mathrm{SO}(5)$ antiferromagnet on the triangular lattice also with Heisenberg coupling $J_{ij} = -4J_{ts}$, because $\left(\vec{\Delta}_{ij}^{ts}, \vec{\Delta}_{ij}^{st} \right)$ together form a $\mathrm{SO}(6)$ vector, and

condensing each component of the vector breaks the SO(6) down to SO(5) $\sim$ Sp(2). Each component of $\vec{\Delta}_{ts}$ can be viewed as the Sp(2) singlet introduced in Ref. [83]:

$$
\begin{aligned}
H_{\mathrm{MF}} &= \sum_{ij} J_{ts} \left(\phi \ b_i^t i\sigma^{12} b_j + H.c. \right) - J_{ts}\phi^2 \\
&+ \sum_j \mu(\sum_{\alpha=1}^4 b_{j,\alpha}^\dagger b_{j,\alpha} - \kappa),
\end{aligned} \tag{4.28}
$$

Quoting the results in Ref. [83], the FM $\otimes$ 120° state with the previous mean field ansatz with $\phi_1 \perp \phi_2$ has a lower mean field ground state energy density, which is consistent with our analytical observation and also numerical simulation.

4.4.5 Zeeman field driven Metal-Insulator transition

Since the insulator has a fully polarized ferromagnetic order, its energy can be tuned by an external Zeeman field. An inplane magnetic field, whose main effect is the Zeeman coupling can drive a first order metal-insulator transition (a level-crossing) between the unpolarized metal and the fully polarized ferromagnetic insulator, as was observed experimentally at the 1/4 and 3/4 filling of TDBG [74, 58].

There is another possible mechanism of metal-insulator transition driven by a Zeeman field. At the metalic side at the transition, the system is likely described by a $t - J$ model with a similar J, J^s, J^v terms as Eq. 4.10. The Zeeman field tends to polarize the spin, which effectively increases the antiferromagnetic coupling in the valley space $J_{eff}^v = J^v + J\langle \vec{\sigma}_i \cdot \vec{\sigma}_j \rangle$. Thus at certain temperature, the magnitude of the 120° order in the valley space is tunable and enhanced by an external Zeeman field. If the insulating

behavior of the system is a consequence of the finite momentum valley order which folds the Brillouin zone and partially gaps out the Fermi surface, an increasing magnitude of the 120° order in the valley space can gap out larger portion of the Fermi surface, decrease the charge carrier density, and hence eventually drive a *continuous* metal insulator transition.

4.4.6 Liquids and topological phases

When $J^v \sim J^s \sim J$, it would be rather difficult for the system to form any semiclassical order due to "double frustration": the J^s and J^v term of Eq. 4.10 are both already frustrated due to the geometry of the triangular lattice, while the J term further frustrates/disfavors the simultaneous 120° semiclassical order of $\vec{\sigma}_i$ and $\vec{\tau}_i$. Since there is an obvious Lieb-Shultz-Matthis theorem which forbids a completely trivial disordered phase, we expect this "double frustration" effect to lead to either a completely disordered spin-valley liquid state, or a partially ordered state with certain topological order. In this section we explore several possible spin-valley liquids or topological orders in the region $J^v \sim J^s \sim J$.

Spin nematic Z_2 Topological phase

Let us get back to the mean field Hamiltonian Eq. 4.25. As we discussed before, if the mean field value of $\vec{\phi}$ is real (or equivalently if $\vec{\phi}_1$ is parallel to $\vec{\phi}_2$, for example, $\vec{\phi} \sim (0, 0, 1)$, both spin-up and spin-down Schwinger bosons participate in the mean field analysis, and the mean field analysis is technically equivalent to the calculations in Ref. [83] for the Sp(4) antiferromagnet on the triangular lattice. And with large spin

symmetry, the quantum fluctuation makes it more difficult for b_α to condense. If b_α is not condensed, the mean field order parameter $\vec{\phi}$ already breaks the SU(2)^s, and also break the U(1) gauge symmetry down to Z_2 gauge degree of freedom.

The nature of the state with condensed $\vec{\phi}$ but uncondensed b_α depends on the nature of $\vec{\phi}$ under time-reversal. The transformation of b_α under time-reversal can be inferred by the fact that $\vec{\sigma} \to -\vec{\sigma}$, $(\tau^1, \tau^2, \tau^3) \to (\tau^1, \tau^2, -\tau^3)$:

$$\mathcal{T} : b_j \to \mathrm{i}\sigma^{21} b_j, \quad \vec{\Delta}_{ij}^{ts} \to \vec{\Delta}_{ij}^{ts}, \tag{4.29}$$

as long as $\vec{\phi}$ is a real vector (or $\vec{\phi}_1$ parallel with $\vec{\phi}_2$), time-reversal is preserved, and this state is a spin nematic Z_2 topological order. By contrast, if $\vec{\phi}_1 \perp \vec{\phi}_2$ the time-reversal is broken.

$Z_2 \times Z_2$ Spin-valley liquid

More states can be constructed by introducing two flavors of Schwinger bosons $b_{j,\alpha}^s$ and $b_{j,\alpha}^v$ for the spin and valley space on each site respectively, which are subject to the constraint

$$\sum_{\alpha=1,2} b_{j,\alpha}^{s,\dagger} b_{j,\alpha}^s = b_{j,\alpha}^{v,\dagger} b_{j,\alpha}^v = 1. \tag{4.30}$$

These two constraints introduces two U(1) gauge symmetries. It is fairly straightforward to construct the FM $\otimes$ 120° state using this type of Schwinger bosons: b_α^s condenses at zero momentum, while simultaneously b_α^v condenses at the corner of the Brillouin zone.

In fact, due to the "double frustration" effect, both the spin and valley space can

form a Z_2 topological order (overall speaking the system is in a $Z_2 \times Z_2$ spin-valley liquid state), whose e particles carry the fundamental representation of SU(2)^s and SU(2)^v respectively, as long as neither $b^s_{j,\alpha}$ nor $b^v_{j,\alpha}$ introduced in Eq. 4.31 condenses when the mean field parameters break both U(1) gauge symmetries down to Z_2.

More states can be constructed by introducing two flavors of Schwinger bosons $b^s_{j,\alpha}$ and $b^v_{j,\alpha}$ for the spin and valley space on each site respectively, which are subject to the constraint

$$\sum_{\alpha=1,2} b^{s,\dagger}_{j,\alpha} b^s_{j,\alpha} = b^{v,\dagger}_{j,\alpha} b^v_{j,\alpha} = 1. \tag{4.31}$$

These two constraints introduces two U(1) gauge symmetries. It is fairly straightforward to construct the FM $\otimes$ 120° state using this type of Schwinger bosons: b^s_α condenses at zero momentum, while simultaneously b^v_α condenses at the corner of the Brillouin zone.

In fact, due to the "double frustration" effect, both the spin and valley space can form a Z_2 topological order (overall speaking the system is in a $Z_2 \times Z_2$ spin-valley liquid state), whose e particles carry the fundamental representation of SU(2)^s and SU(2)^v respectively, as long as neither $b^s_{j,\alpha}$ nor $b^v_{j,\alpha}$ introduced in Eq. 4.31 condenses when the mean field parameters break both U(1) gauge symmetries down to Z_2.

Starting from the $Z_2 \times Z_2$ spin-valley liquid state, one can also construct a spin-valley liquid with only one Z_2 topological order. This can be formally obtained by forming bound state of the "visons" (the m excitations) of both Z_2 topological orders, and condense the bound state. This condensate will confine b^s_α and b^v_α separately, but their bound state is still deconfined, and becomes the e particle of the new Z_2 topological

order. This final Z_2 topological order preserves all the symmetries of the system, and it can also be constructed using the same mean field formalism as Eq. 4.22, as long as one condenses the spin-singlet/valley-singlet pairing operator Δ_{ij}^{ss} in Eq. 4.22.

$U(1) \times U(1)$ **Dirac spin-valley liquid**

More exotic spin-valley liquid states can be constructed by introducing fermionic slave particles $f_{j,\alpha}^s$ and $f_{j,\alpha}^v$ which are subject to the constraints

$$\sum_{\alpha=1,2} f_{j,\alpha}^{s,\dagger} f_{j,\alpha}^s = f_{j,\alpha}^{v,\dagger} f_{j,\alpha}^v = 1. \tag{4.32}$$

In Ref. [61], a Dirac spin liquid with U(1) gauge field and $N_f = 4$ flavors of Dirac fermions was constructed for spin-1/2 systems on the triangular lattice. And this Dirac spin liquid is the parent state of both the 120° ordered state and the valence bond solid state [61, 94, 96], and it could be a deconfined quantum critical point between these two different ordered states [46].

In our case, both spin and valley space can form the Dirac liquid phase mentioned above, due to the double frustration effect. Thus in total there are eight flavors of Dirac fermions and two U(1) gauge fields.

$SU(4)$ **Point**

At the point $J^v = J^s = J$, this model has a SU(4) $\sim$ SO(6) symmetry. Although semiclasical approach such as nonlinear sigma model were studied before for SU(N) antiferromagnet with other representations [81], with a fundamental representation on

every site, this model has no obvious semiclassical limit to start with, and it is expected to be a nontrivial spin liquid or topological order. At this point, it is most convenient to define a four component Schwinger boson $b_{j,\alpha}$ on every site which forms fundamental representation under both the spin and valley $SU(2)$ symmetry, and there is a constraint $\sum_{\alpha=1}^{4} b_{j,\alpha}^{\dagger} b_{j,\alpha} = 1$.

Unlike a $SU(2)$ spin system, one can prove that at the $SU(4)$ point there cannot be a fully symmetric Z_2 spin liquid whose e particle is the b_α slave particle. The reason is that all the local spin excitations can be written as $b_{j,\alpha}^{\dagger} b_{j,\beta}$ with different $\alpha, \beta = 1 \cdots 4$, hence all the local spin excitations are invariant under the Z_4 center of the $SU(4)$ group. In a Z_2 topological order, two of the e particles should merge into a local excitations, while two b_α slave particle cannot fuse into a representation that is invariant under the Z_4 center. This argument also shows that a Z_2 topological order whose e particle is a $SO(6)$ vector is allowed.

On the other hand, using the slave particle b_α one can construct a Z_2 topological order with certain spontaneous $SU(4)$ symmetry breaking. At the $SU(4)$ point, the model Eq. 4.10 can be written as

$$H = \sum_{ij} J \left(-\frac{5}{4} (\vec{\Delta}_{ij}^{\dagger}) \cdot (\vec{\Delta}_{ij}) + \cdots \right), \tag{4.33}$$

where $\vec{\Delta}_{ij}$ is a six component vector pairing between b_α. One can introduce a six component complex $SO(6)$ vector mean field parameter $\vec{\phi}$:

$$H_{\text{MF}} = \sum_{ij} J \left(-\frac{5}{4} \vec{\phi} \cdot \vec{\Delta}_{ij} + H.c. \right) + \frac{5}{4} J |\vec{\phi}|^2. \tag{4.34}$$

The complex vector $\vec{\phi} = \vec{\phi_1} + \mathrm{i}\vec{\phi_2}$, where its real and imaginary parts $\vec{\phi_1}$ and $\vec{\phi_2}$ can be either parallel or orthogonal to each other. If the Schwinger boson does not condense, both mean field theories would lead to a Z_2 topological order on top of the spontaneous SU(4) symmetry breaking.

Our DMRG simulation actually suggest that the SU(4) point of the spin-valley model is a spin-valley liquid state with a Fermi surface of fermionic slave particles, which will be presented in detail in another work.

4.4.7   Conclusion

In this work we demonstrated both analytically and numerically that a quantum spin-valley model with all antiferromagnetic interaction can have a fully polarized ferromagnetic order in its phase diagram. We propose possible mechanism for an inplane Zeeman field to drive a metal-insulator transition, as was observed experimentally at the 1/4 and 3/4 filling of TDBG. We also discussed various possible nontrivial spin-valley liquid state and topological order of this model.

We would like to acknowledge several previous theoretical works that studied the ferromagnetism in Moir$\vec{e}$ systems using different approaches and different models [48, 90, 9, 114]. For example, in Ref. [90], a spin-valley model with *ferromagnetic couplings* on an effective honeycomb Moir$\vec{e}$ lattice was derived for the twisted bilayer graphene system. While our work (which aims to understand a different Moir$\vec{e}$ system, *i.e.* the twisted double bilayer graphene) demonstrated that ferromagnetism can emerge from the

spin-valley model on a triangular lattice with *fully antiferromagnetic interaction.*

Within our framework, under doping, again the system is likely described by the $t-J$ model with the similar J, J^s, J^v terms as Eq. 4.10. Then the analysis in Ref. [118] still applies: the spin-triplet/valley-singlet pairing channel between electrons would become the strongest pairing channel. Due to a strong on-site Hubbard interaction, the system would still prefer to become a $d+id$ topological superconductor with spin triplet pairing.

4.4.8   Emergent Superconductivity in the Mott Insulator Phase

While we have discussed the likely FM correlated insulator behavior of MAMM materials, we have yet to discuss the many observations of transitions into superconducting states in their vicinity.

While it is believed that the nearly flat mini bands of the system [109, 69, 27, 21] play a major role in the phenomena observed so far, the physics we discuss in the current section will be largely independent of the details of the microscopic model, despite the increasing number of works in this area: beyond the work summarized in section 4.3, another work by Kievelson et. al. Ref. [23] similarly described the system with an effective two-orbital extended Hubbard model on a triangular lattice near half-filling. The prediction of Ref. [118] has been checked with numerical methods [28]; Ref. [79, 124, 119] described the system with a tight binding model on a honeycomb lattice, while the electron Wannier functions strongly peak at the triangular lattice sites. The main difference between these two classes of models is that the latter models capture the physics related to

Dirac band crossings between a *pair* of flat mini-bands. While at the doping where the SC and MI were observed, *i.e.* near half-filling within one of the mini-bands, it is not clear that any symmetry protected Dirac point away from the band plays a major role, unless one assumes a specific type of valley order, which leads to extra Dirac crossings within the mini flat band [79, 119]. But without compelling evidence of this particular valley ordering in the MI phase, the qualitative physics at the most relevant doping can potentially be captured by the (simpler) effective triangular lattice models introduced in Ref. [118, 23]. Especially since the activation energy of the insulating phase is very low (4K) [11] even compared with the narrow bandwidth and the effective Hubbard interaction, this Mott insulator is rather weak and it is conceivable that its insulating behavior can be understood based solely on the electrons near the Fermi surface.

We instead focus on two peculiar and qualitative phenomena observed in TBG [12].

1. The resistivity $R_{xx}(T)$ in Ref. [12] shows that at the Mott insulator doping, $R_{xx}(T)$ first increases with lowering temperature below $T_m \sim 4 - 5$K (as one would expect for an insulator), while rapidly drops to zero below another temperature scale $T_c \sim 1$K. This feature means that quite surprisingly the MI phase at very low energy scale still has a superconductivity instability.

2. Once the SC is suppressed by a weak external magnetic field, the system becomes a normal MI with $R_{xx}(T)$ growing without saturation at low temperature.

As we have mentioned the insulator phase in this system must be a "weak" one, its activation gap is about the same as $k_B T_m$, which is much lower than the estimated

Hubbard interaction, even with the large unit cell of the moiré structure. A weak Mott insulator can be naturally understood based on physics around the Fermi surface only. The electrons on the Fermi surface can be gapped out by an order parameter at finite momentum through folding of the Brillouin zone. When the amplitude of the order parameter is weak, i.e. when the system is close to the order-disorder quantum phase transition, only the "hot spots" on the Fermi surface connected by the momentum of the order parameter are gapped out; but with a sufficiently strong order parameter and its coupling to the electrons, the entire Fermi surface is gapped out, and the system becomes an insulator, which can usually be adiabatically connected to a strong Mott insulator at strong coupling without any phase transition.

The simplest analogue of the physics described above is the Hubbard model on the square lattice with nearest neighbor hopping at exactly half filling. A weak Hubbard interaction will induce the antiferromagnetic order at momentum (π, π) and drive the system into an insulator due to the Brillouin zone folding and nesting of Fermi surface. And the insulator with weak Hubbard U can be adiabatically connected to the insulator with large U, where all the electrons are well localized on every site.

4.4.9 Mechanism for weak MI and emergent SC

Ref. [118, 23] both started with a two orbital extended Hubbard model to understand the main experimental observations of the moiré superlattice of twisted bilayer graphene. The site of the triangular lattice is a patch of the bilayer graphene with AA stacking. The

two effective orbitals correspond to the two valleys at the corners of the Brillouin zone of the original honeycomb lattice. Both models in Ref. [118, 23] have a SU(4) symmetry at the leading order, and the SU(4) symmetry is broken by other interactions such as the Hund's interaction. Ref. [118, 23] chose a different sign for the Hund's coupling, hence the former prefers a spin triplet and valley singlet on every triangular lattice site, while the latter prefers a spin singlet and valley order.

Here we first argue that the phenomena (1) and (2) mentioned above can be both naturally explained within the framework of Ref. [118]. A Hund's coupling chosen as Ref. [118] will favor the two electrons on every site in the Mott insulator phase to form a spin-1, with an antiferromagnetic coupling between neighboring sites. The frustrated nature of the triangular lattice will likely drive the system into a spin density wave order. Even if we start with a geometrically unfrustrated honeycomb lattice, the weakness of the Mott insulator will also generate further neighbor spin interaction and even multi-spin interactions which frustrate the collinear magnetic order, and may as well lead to a spin density wave (SDW). This SDW order connects different parts of the Fermi surface through Brillouin zone folding. Phenomenon (2) suggests that when a "competing order" is suppressed and the SDW is stabilized, the entire Fermi surface should be gapped out by the SDW, i.e. there is no residual Fermi pocket left at the Fermi surface, hence the amplitude of the SDW and its coupling to the electrons are sufficiently strong. But let us not forget that the system is purely two dimensional, hence with a full spin SU(2) symmetry, the spins can never form a true long range order at infinitesimal temperature.

This situation is different from a magnetic order close to its quantum critical point, in the sense that close to a quantum critical point, both the amplitude and direction of the magnetic order parameter will fluctuate strongly; while in our case the amplitude of the SDW does not fluctuate strongly, it is the direction of the order parameter that modulates over a long correlation length scale $\xi(T)$.

A finite but long correlation length $\xi(T)$ implies that within a thin momentum shell around the Fermi surface with $|\boldsymbol{p} - \boldsymbol{k}_F| < \Lambda(T) \sim \hbar/\xi(T)$, the fermions will not feel the background SDW order parameter with finite correlation length. Rather than demonstrate this effect by detailed calculations based on a microscopic model, one can visualize this effect by simply coarse-graining the system, until $\hbar/\xi$ becomes the ultraviolet (UV) cut-off (thickness) of the momentum shell around the Fermi surface following the standard renormalization group picture of Fermi surface [91], and within this shell the electrons only see a very short range correlated SDW, whose effects can be neglected. The electrons within the thin shell are still "active" and can transport electric charge, or even form Cooper pairs (Fig. 4.5); while the electrons outside this momentum shell will effectively view the background SDW as a true long range order, and hence are effectively "gapped out". Based on the phenomenon (2), we know that the gap induced by the SDW is strong enough when the SDW is stabilized by an external field.

The active fermion density is proportional to the thickness of the momentum shell $\Lambda(T) \sim \hbar/\xi(T)$. The correlation length $\xi(T)$ of a SDW with a full SU(2) spin symmetry can be estimated from the standard renormalization group calculation. Let us take

the noncollinear SDW as an example, which happens very often in frustrated magnet (the experimental phenomena would also be consistent with a collinear SDW at finite momentum). A noncollinear SDW would break the entire SO(3) spin rotation group. The standard way of describing such SDW is to parameterize its configuration manifold with two orthogonal vectors $\boldsymbol{n}_1$, $\boldsymbol{n}_2$. It is convenient to introduce a SU(2) spinor field $z = (z_1, z_2)^t$ [18], and

$$\boldsymbol{n}_1 \sim \text{Re}[z^t i\sigma^y \boldsymbol{\sigma} z], \quad \boldsymbol{n}_2 \sim \text{Im}[z^t i\sigma^y \boldsymbol{\sigma} z] \tag{4.35}$$

$z = (z_1, z_2)^t$ are complex bosonic fields at certain momentum $\boldsymbol{Q}$, and subject to constraint $|z_1|^2 + |z_2|^2 = 1$. The two component complex field z_α lives in a target manifold: the three dimensional sphere S^3, and it must couple to a $\mathbb{Z}_2$ gauge field [18], and when z_α condenses the ground state manifold is $S^3/\mathbb{Z}_2$, which is identical to the ground state manifold of a noncollinear SDW.

The finite temperature physics of the SDW is well described by the nonlinear sigma model (NLSM) defined with the spinor z_α field:

$$Z = \int Dz_\alpha(x) \exp\left(-\int d^2x \, \frac{1}{2g} \sum_\alpha |\boldsymbol{\nabla} z_\alpha|^2\right), \tag{4.36}$$

where $g = k_B T/\rho_s$, and again ρ_s is the spin stiffness at zero temperature. The 2nd order renormalization group (RG) equation of the coupling constant g is

$$\frac{dg}{d\ln l} = \frac{1}{\pi}g^2 + O(g^3). \tag{4.37}$$

For small g (low temperature), the correlation length scales as:

$$\xi(T) \sim a_0 \exp\left(\frac{\pi \rho_s}{k_B T}\right), \tag{4.38}$$

with an extra less important power-law function of T/ρ_s in the prefactor [116, 22]. a_0 is the lattice constant of the moir$\vec{e}$ superlattice, ρ_s is the spin stiffness at zero temperature. This means that the energy width of the momentum shell $v_f \Lambda(T)$ is much smaller than the thermal energy $k_B T$ at low enough temperature T, hence the electrons in this shell are fully thermally excited. Thus the transport properties of these electrons can be captured by the most classical theory of transport, such as the Drude theory. For instance, the electric conductivity of the system is

$$\sigma(T) \sim \frac{n(T) e^2 \tau}{m^*}, \tag{4.39}$$

where $n(T)$ is the density of electrons within this momentum shell, and it is proportional to $\Lambda(T)$. Thus we can see that although there is no true magnetic order at any finite temperature, due to the rapidly decreasing density of active electrons within the momentum shell, the resistivity $R_{xx}(T)$ will still rise with lowering temperature, before the system becomes a SC.

At low temperature, the active electrons within the momentum shell can still form a SC, which is consistent with the phenomenon (1) mentioned above. But since the correlation length $\xi(T)$ grows rapidly with lowering temperature, there are less and less active electrons available for pairing, which is a sign of strong competition between SC and the SDW. The SC transition temperature T_c for the active electrons can be estimated
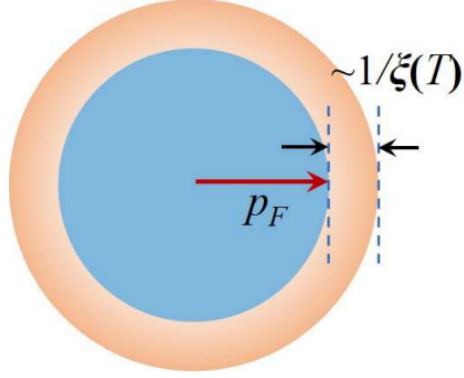
126

Figure 4.5: The "active" electrons within the thin momentum shell around the Fermi surface with $|\boldsymbol{p} - \boldsymbol{p}_F| < \Lambda \sim \hbar/\xi(T)$, which are insensitive to the background SDW with finite correlation length $\xi(T)$, and hence can transport electric charge and potentially form a SC.

through the standard BCS theory, under the assumption of a uniform gap function around the Fermi surface (which is the case for almost all the superconductors predicted in this system so far):

$$\frac{1}{J} = \int_0^{v_f \Lambda(T)} d\varepsilon \frac{N}{\sqrt{\varepsilon^2 + \Delta^2}} \tanh\left(\frac{\sqrt{\varepsilon^2 + \Delta^2}}{k_B T} \right), \qquad (4.40)$$

where J represents the Heisenberg interaction on the effective triangular lattice, which is the "gluing force" for superconductivity [118]. In Eq. 4.40 we have replaced the UV cut-off of the standard BCS theory by $v_f \Lambda(T)$. As always N is the density of states around the Fermi surface, which has been taken to be a constant. As we explained, at very low temperature $v_f \Lambda(T)$ is much smaller than $k_B T$, hence at T_c ($\Delta = 0$), this equation can be simplified as

$$\frac{1}{NJ} = \frac{v_f \Lambda(T_c)}{k_B T_c}. \qquad (4.41)$$

127

This equation does not always have a solution, it only supports a nonzero T_c when $NJ \gtrsim \pi \rho_s a_0/(\hbar v_f)$. Hence the system no longer has a BCS instability against infinitesimal attractive interaction, the interaction J needs to be stronger than a critical strength.

4.4.10   With weak anisotropy

Once an external magnetic field is turned on (either inplane or out-of-plane), the magnetic order will be more "stabilized" at low temperature because the spin symmetry is reduced to U(1), which supports a quasi long range order with infinite correlation length. In this case, the size of the momentum shell (and the density of the active electrons) vanishes to zero, and there is no room for SC.

The way a uniform Zeeman field couples to the spinor field z_α depends on the symmetry of the noncollinear SDW, but it will at least break the SO(3) symmetry down to U(1). A weak Zeeman field h will be renormalized to $h(l)$ at length scale l: $l/a_0 \sim (h(l)/h)^{1/\delta}$, where δ is the scaling dimension of h in the NLSM; while at the same length scale the coupling constant g is renormalized according to Eq. 4.37. Comparison between the RG flow of $h(l)$ and $g(l)$ defines a critical temperature T_c':

$$\left(\frac{\rho_s}{h}\right)^{1/\delta} \sim \exp\left(\frac{\pi \rho_s}{k_B T_c'}\right). \tag{4.42}$$

When $T \ll T_c'$, the coupling constant $g(l)$ will still be small and perturbative when h becomes nonperturbative compared with ρ_s, hence $g(l)$ stops growing at a small value, and the system is in a quasi long range ordered SDW phase; while when $T \gg T_c'$, the
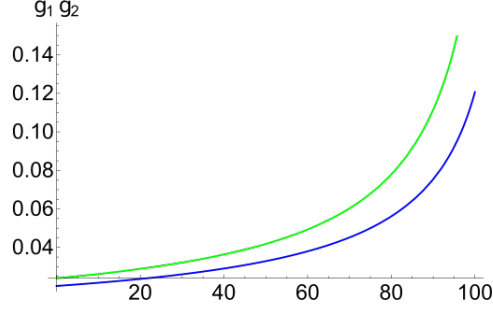
Figure 4.6: The RG flow of g_1 and g_2 described by Eq. 4.46, with initial values $g_1 = 0.24$, $g_2 = 0.02$, and their difference is amplified under RG. The horizonal axis is the RG scale l.

coupling constant $g(l)$ becomes nonpeturbative before $h(l)$ could affect the RG flow of Eq. 4.37, and the system is in the disordered phase. Thus T'_c can be viewed as the critical temperature of the O(2) SDW (the Kosterlitz-Thouless transition critical temperature), which depends on the external Zeeman field h as

$$T'_c \sim \frac{\rho_s}{\log(\rho_s/h)}, \tag{4.43}$$

which is consistent with previous studies with magnetic systems with weak anisotropy [41].

As an illustration of the physics discussed above, let us consider a simple case without reflection symmetry (the reflection symmetry takes $z_\alpha \to \epsilon_{\alpha\beta} z_\beta^*$ in Ref. [18]), where an external field leads to the following anisotropic NLSM:

$$\int d^2x \ \frac{1}{2g_1}|\boldsymbol{\nabla} z_1|^2 + \frac{1}{2g_2}|\boldsymbol{\nabla} z_2|^2 + \frac{m^2}{k_B T}|z_1|^2, \tag{4.44}$$

$g_i = k_B T/\rho_i$. We take $\rho_2 > \rho_1$ for $m^2 > 0$, *i.e.* the anisotropy favors the condensate of z_2, but penalizes condensate of z_1.

Starting with $m = 0$, the RG flow of g_i is described by the Ricci flow [30, 31]:

129

$$\beta(g_{ab}) = -\frac{1}{2\pi}\mathcal{R}_{ab}, \tag{4.45}$$

where g_{ab} is the metric tensor of the target manifold of the NLSM, and $\mathcal{R}_{ab}$ is the Ricci tensor (see appendix for more details). Expanded at the ordered state with $z_1 = 0$, $z_2 \neq 0$, the Ricci flow of the metric tensor translates into the RG flow of g_1 and g_2 in the field theory Eq. 4.44

$$\begin{aligned}
\frac{dg_1}{d\ln l} &= \frac{1}{2\pi}\left(g_1^2 + \frac{g_1^3}{g_2}\right) + O(g_i^3), \\
\frac{dg_2}{d\ln l} &= \frac{1}{\pi}g_1 g_2 + O(g_i^3).
\end{aligned} \tag{4.46}$$

The RG equations Ref. 4.46 can be solved exactly for arbitrary initial values of g_1, g_2 with a complicated form (see appendix). If we start with a choice of different g_1 and g_2, their difference will be amplified under RG flow (Fig. 4.6). Intuitively, as long as g_i are small enough (for low enough temperature or the spin stiffness is sufficiently strong), once m^2 is renormalized strong, z_1 will be explicitly gapped, and z_2 becomes an O(2) order parameter, and enters a quasi long range algebraic phase where g_2 stops growing under RG. The general physics discussed in this section becomes manifest in model Eq. 4.44.

With increasing magnetic field h, the Mott insulator phase will eventually be destroyed, so will the SDW order. With strong field, the order-disorder transition of the SDW is likely a quantum phase transition with dynamical exponent 2, due to the precession of the inplane SDW order parameter under an external field.

4.4.11 Connections to more experimental phenomena, and comparison with other theories

In our picture the weak Mott insulator is a consequence of a SDW at finite momentum, which significantly reduces the density of "active" fermions around the Fermi surface with lowering temperature. Thus the SDW is a competing order of the SC. We expect this to be still true under small doping away from the Mott insulator. Experimentally the Hall density of charge carriers in the hole-doped Mott insulator is indeed proportional to the dopant density away from the Mott insulator, suggesting the persistence of the SDW under hole doping. And with an external field, either inplane or out-of-plane, the SDW will be stabilized (the effect of a weak magnetic field will be strongly amplified due to the logarithmic dependence of h in Eq. 4.43), thus the SC (even a spin triplet SC) will be significantly weakened due to its competition with the magnetic order.

We would also like to point out that the main phenomena (1) and (2) mentioned in the introduction are less likely to be simultaneously consistent with other theories proposed so far. Ref. [23] proposed a nematic order which spontaneously breaks the symmetry of the valley space in the Mott insulator phase, while Ref. [119] proposed a valence bond solid (VBS) order in the Mott insulator. The valley space does not have a SU(2) symmetry, hence at low temperature it would form either a true long range order (which spontaneously breaks a discrete symmetry) or a quasi long range order (which spontaneously breaks the approximate U(1) valley symmetry). In either case, it seems difficult to reconcile phenomena (1) and (2): since the system is clearly an insulator when

131

the SC is suppressed, there must be no Fermi pockets left with the valley order; but the correlation length of the valley order remains infinite after the field is removed due to the lower symmetry of the valley space, hence the density of "active fermions" is still zero, and there seems no natural way to explain the emergence of SC inside the MI. The VBS order proposed in Ref. [119] has the similar issue.

4.4.12 Summary

In summary we have proposed a phenomenological understanding of the unusual emergent superconductivity inside a weak Mott insulator observed recently in the bilayer Graphene Moir$\vec{e}$ superlattice. In our picture this peculiar phenomenon is due to the pure two dimensional nature of the system, and also the symmetry of the order parameter that leads to the MI. We expect this to be a quite generic mechanism, and similar behaviors can be found in other two dimensional systems.

4.5 Other works and Closing Remarks

In summary, we've reviewed some of the important aspects of a new class of materials which, unlike many previous solid state devices, may be non-destructively tuned into a strongly-correlated phase through the application of gate voltages. Such control over a device is, historically speaking, unprecedented. With the mysteries that surround the behavior of strongly correlated electron systems, this material class, as well as other similar experimental platforms likely to emerge, will give the community improved clarity

into the nature of strongly interacting electron systems.

Such progress has already been made in TBG, for example. In a 2019 publication, Cao et. al [10] demonstrated evidence for "strange metal" NFL liquid behavior at and near fractional fillings that exhibited Superconducting Phases. They found Plankian scattering and strongly dissipative dynamics in the intermediate tempeature regime above the superconducting transition — a situation provocatively similar to the phase diagrams of e.g. HTSC materials. This exciting development again ties into the larger picture of correlated electron systems, whose quantum critical regime remains both universal and, yet, poorly understood.

We briefly mention that a similar behavior in the R v.s. T plot has been observed in $La_{1.875}Ba_{0.125}CuO_4$ subject to disorder induced by radiation [56]. A similar argument can be made for this material, such that the disorder weakens the strength of the underlying CDW phase, allowing the SC to emerge at higher Temperatures.

Appendix A

Detailed Work on Quadratic Band Crossing

A.1 General Solutions to the Flow Equations

In order to evaluate the flow equations for the couplings and the source terms, we shall make use of the following integral:

$$
\begin{aligned}
\int \frac{d\omega}{2\pi} \int_{\Lambda(1-d\ell)}^{\Lambda} &\frac{d^2k}{(2\pi)^2} \hat{G}_0(i\omega, \mathbf{k}) \otimes \hat{G}_0(\pm i\omega, \pm\mathbf{k}) = \\
&\frac{m}{4\pi} d\ell \left[\mp A^{ph,pp} 1_4 \otimes 1_4 + \frac{1}{2} B^{ph,pp} \sigma_3 1 \otimes \sigma_3 1 + \frac{1}{2} C^{ph,pp} \sigma_1 1 \otimes \sigma_1 1 \right],
\end{aligned}
\tag{A.1}
$$

where $\hat{G}_0(i\omega, \mathbf{k})$ is the bare Green function following from (2.2). The upper and lower signs on the left hand side of (A.1) correspond to the labels ph and pp on the right hand side, respectively. The coefficients on the right hand side of (A.1) are given by
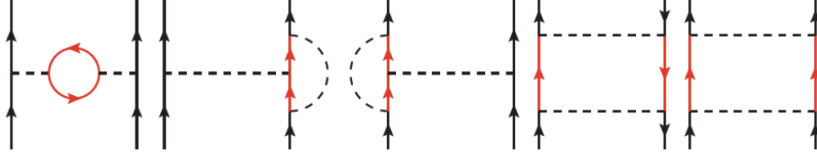
Figure A.1: Feynman diagrams contributing to the flow of the couplings g_i. The solid lines correspond to fermions; the dashed lines correspond to interactions. The internal fermion lines (colored red) have "fast" momenta $\Lambda(1 - d\ell) < |\mathbf{k}| < \Lambda$, while the external legs have "slow" momenta $|\mathbf{k}| < \Lambda(1 - d\ell)$.

$$
\begin{aligned}
A^{ph} &= -\frac{\sqrt{2}}{\pi} \frac{K(1 - \cot^2 \eta)}{|\sin \eta|} \\
B^{ph} &= \frac{2\sqrt{2}[E(1 - \cot^2 \eta) - \cot^2 \eta K(1 - \cot^2 \eta)]}{\pi|\sin \eta|(1 - \cot^2 \eta)} \\
C^{ph} &= \frac{2\sqrt{2}[K(1 - \cot^2 \eta) - E(1 - \cot^2 \eta)]}{\pi|\sin \eta|(1 - \cot^2 \eta)}.
\end{aligned} \tag{A.2}
$$

and

$$
\begin{aligned}
A^{pp} &= \frac{\sqrt{2}}{\pi|\sin \eta|} \left[K(1 - \cot^2 \eta) + \frac{\lambda^2}{\sin^2 \eta - \lambda^2} \Pi \left(\frac{\sin^2 \eta - \cos^2 \eta}{\sin^2 \eta - \lambda^2}, 1 - \cot^2 \eta \right) \right], \\
B^{pp} &= \frac{2^{3/2}}{\pi|\sin \eta|(\tan^2 \eta - 1)} \left[-K(1 - \cot^2 \eta) + \Pi \left(\frac{\sin^2 \eta - \cos^2 \eta}{\sin^2 \eta - \lambda^2}, 1 - \cot^2 \eta \right) \right], \\
C^{pp} &= \frac{2^{3/2}}{\pi|\sin \eta|(1 - \cot^2 \eta)} \left[K(1 - \cot^2 \eta) - \frac{\cos^2 \eta - \lambda^2}{\sin^2 \eta - \lambda^2} \Pi \left(\frac{\sin^2 \eta - \cos^2 \eta}{\sin^2 \eta - \lambda^2}, 1 - \cot^2 \eta \right) \right].
\end{aligned} \tag{A.3}
$$

Note that the coefficients in (A.2), which correspond to particle-hole scattering processes, are independent of the particle-hole asymmetry λ. The functions K, E, and Π are complete elliptic functions. In the limit of particle-hole symmetry ($\lambda = 0$) and rotational invariance ($\eta = \pi/4$), (A.2) and (A.3) reduce to $A^{ph,pp} = B^{ph,pp} = C^{ph,pp} = 1$.

From evaluating the one-loop diagrams shown in Figure A.1, one obtains the coefficients $A_{ijk} = \sum_{m=1}^{5} A_{ijk}(m)$ in the flow equation for the couplings [(2.6) in the main text], where m labels the five diagrams in Figure A.1. One gets only diagonal contributions

from the first diagram:

$$A_{iii}(1) = \left[-4A^{ph} + C^{ph} \text{ Tr}((\sigma_1\sigma_j)^2) + B^{ph} \text{ Tr}((\sigma_3\sigma_j)^2) \right] \frac{m}{4\pi}. \tag{A.4}$$

From the second and third diagrams combined:

$$A_{iij}(2) + A_{iij}(3) = \left[A^{ph} \text{ Tr}(\sigma_i\sigma_j\sigma_i\sigma_j) - \frac{1}{2}C^{ph} \text{ Tr}(\sigma_i\sigma_j\sigma_1\sigma_i\sigma_1\sigma_j) \right. \\ \left. - \frac{1}{2}B^{ph} \text{ Tr}(\sigma_i\sigma_j\sigma_3\sigma_i\sigma_3\sigma_j) \right] \frac{m}{4\pi}. \tag{A.5}$$

From the fourth diagram:

$$A_{ijk}(4) = \frac{1}{8} \left[2A^{ph} \text{ Tr}(\sigma_k\sigma_j\sigma_i) \text{ Tr}(\sigma_j\sigma_k\sigma_i) - C^{ph} \text{ Tr}(\sigma_k\sigma_1\sigma_j\sigma_i) \text{ Tr}(\sigma_j\sigma_1\sigma_k\sigma_i) \right. \\ \left. - B^{ph} \text{ Tr}(\sigma_k\sigma_3\sigma_j\sigma_i) \text{ Tr}(\sigma_j\sigma_3\sigma_k\sigma_i) \right] \frac{m}{4\pi}. \tag{A.6}$$

Finally, from the fifth diagram:

$$A_{ijk}(5) = -\frac{1}{8} \left[2A^{pp} \left(\text{Tr}(\sigma_k\sigma_j\sigma_i) \right)^2 + C^{pp} \left(\text{Tr}(\sigma_k\sigma_1\sigma_j\sigma_i) \right)^2 + B^{pp} \left(\text{Tr}(\sigma_k\sigma_3\sigma_j\sigma_i) \right)^2 \right] \frac{m}{4\pi}. \tag{A.7}$$

The flows of the source terms introduced in (2.8) are computed by evaluating the diagrams shown in Figure A.2. Evaluating these diagrams and using (A.1) gives the following expressions for the coefficients appearing in the main text:
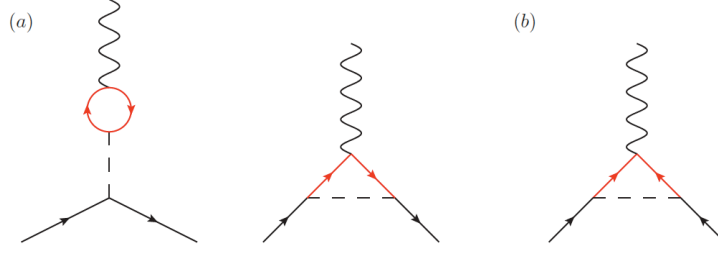
Figure A.2: Feynman diagrams contributing to the flow of the source terms $\Delta_i^{c,s,pp}$. The solid lines correspond to fermions; the dashed lines correspond to interactions. The two diagrams in (a) give contributions to the particle-hole source terms, while the diagram in (b) contributes to the particle-particle source term. The internal fermion lines (colored red) have "fast" momenta $\Lambda(1-d\ell) < |\mathbf{k}| < \Lambda$, while the external legs have "slow" momenta $|\mathbf{k}| < \Lambda(1-d\ell)$.

$$B_{ij}^{(c,s)}(1) = \frac{m}{4\pi}\{-A^{ph}\text{Tr}[(\sigma_j 1)M_i^{(c,s)}] + \frac{1}{2}B^{ph}\text{Tr}[(\sigma_j 1)(\sigma_3 1)M_i^{(c,s)}(\sigma_3 1)]$$
$$+ \frac{1}{2}C^{ph}\text{Tr}[(\sigma_j 1)(\sigma_1 1)M_i^{(c,s)}(\sigma_1 1)]\},$$

$$B_{ij}^{(c,s)}(2) = -\frac{m}{16\pi}\{-A^{ph}\text{Tr}[((\sigma_j 1)M_i^{(c,s)})^2] + \frac{1}{2}B^{ph}\text{Tr}[M_i^{(c,s)}(\sigma_j 1)(\sigma_3 1)M_i^{(c,s)}(\sigma_3 1)(\sigma_j 1)]$$
$$+ \frac{1}{2}C^{ph}\text{Tr}[M_i^{(c,s)}(\sigma_j 1)(\sigma_1 1)M_i^{(c,s)}(\sigma_1 1)(\sigma_j 1)]\}, \qquad \text{(A.8)}$$

$$B_{ij}^{(pp)} = -\frac{m}{16\pi}\{A^{pp}\text{Tr}[(\sigma_j 1)M_i^{(pp)}(\sigma_j 1)^T M_i^{(pp)}]$$
$$+ \frac{1}{2}B^{pp}\text{Tr}[M_i^{(pp)}(\sigma_j 1)(\sigma_3 1)M_i^{(pp)}(\sigma_3 1)(\sigma_j 1)^T]$$
$$+ \frac{1}{2}C^{pp}\text{Tr}[M_i^{(pp)}(\sigma_j 1)(\sigma_1 1)M_i^{(pp)}(\sigma_1 1)(\sigma_j 1)^T]\}.$$

Adding the contributions from the first two diagrams together then gives $B_{ij}^{(c,s)} = B_{ij}^{(c,s)}(1)+$

$B_{ij}^{(c,s)}(2)$. By differentiating the free energy with respect to the source terms, one obtains

the following expression for the particle-hole susceptibilities in the charge and spin chan-

nels:

$$\chi_i^{(c,s)}(\ell) = \frac{m}{4\pi}\int_0^\ell d\ell' e^{2\Omega_i^{(c,s)}(\ell')}\left\{-4A^{ph} + \frac{1}{2}B^{ph}\text{Tr}[(\sigma_3 1)M_i)^2] + \frac{1}{2}C^{ph}\text{Tr}[(\sigma_1 1)M_i)^2]\right\} \text{(A.9)}$$

where

$$\Omega_i^{(c,s)}(\ell) = \int_0^\ell d\ell' \sum_{j=0}^3 B_{ij}^{(c,s)} g_j(\ell').$$ (A.10)

The particle-particle susceptibilities are given by

$$\chi_i^{pp}(\ell) = \frac{m}{4\pi} \int_0^\ell d\ell' e^{2\Omega_i^{pp}(\ell')} \left\{ 4A^{pp} + \frac{1}{2} B^{pp} \text{Tr}[(\sigma_3 1) M_i)^2] + \frac{1}{2} C^{pp} \text{Tr}[(\sigma_1 1) M_i)^2] \right\}$$ (A.11)

where

$$\Omega_i^{pp}(\ell) = \int_0^\ell d\ell' \sum_{j=0}^3 B_{ij}^{pp} g_j(\ell').$$ (A.12)

A.2 Flow equation coefficients with finite μ

Let the bare part of the action be given by

$$
\begin{aligned}
S_0 = T \sum_n \int_0^{2\pi} \frac{d\theta_{\mathbf{k}}}{2\pi} \int_0^{\Lambda(\theta_{\mathbf{k}})} \frac{dk}{2\pi} k \\
\times \sum_\alpha \psi_{n\mathbf{k}\alpha}^\dagger [-(i\omega_n + \mu) 1_2 + \mathcal{H}_0(\mathbf{k})] \psi_{n\mathbf{k}\alpha},
\end{aligned}
$$ (A.13)

where we have taken the the UV cutoff to be dependent on the angle in $\mathbf{k}$-space. We can write this as $\Lambda(\theta_{\mathbf{k}}) = \Lambda f(\theta_{\mathbf{k}})$, and will choose $f(\theta_{\mathbf{k}})$ below. We shall assume in what follows that $\mu \geq 0$, so that the Fermi level is at positive energy. In performing an RG step, we decrease the cutoff magnitude as $\Lambda \to \Lambda e^{-\ell}$, without scaling the angle-dependent part $f(\theta_{\mathbf{k}})$. Similarly, we scale the magnitude of all momenta as $k \to k e^\ell$, while leaving $\theta_{\mathbf{k}}$ untouched. With the scaling for μ, ω_n, and $\psi_{n\mathbf{k}\sigma}$ remaining the same as before, one sees that the bare action (A.13) remains invariant.

The Green function obtained from (A.13) is

$$\hat{G}_0(i\omega, \mathbf{k}) = \frac{-(i\omega + \mu - \frac{\lambda}{\sqrt{2m}}k^2)1_2 - \frac{k^2}{\sqrt{2m}}(\sin\eta\sin 2\theta_\mathbf{k}\sigma_1 + \cos\eta\cos 2\theta_\mathbf{k}\sigma_3)}{(i\omega + \mu)^2 - \left(\frac{k^2}{2m}\right)^2\left(\sqrt{2}\lambda + \sqrt{1 + \cos(2\eta)\cos(4\theta_\mathbf{k})}\right)^2}. \quad (A.14)$$

The outer product that is required in evaluating the one-loop diagrams is given by (taking the limit $T \to 0$)

$$\int_> \hat{G}_0(+) \otimes \hat{G}_0(\pm) \equiv \int \frac{d\omega}{2\pi} \int_0^{2\pi} \frac{d\theta_\mathbf{k}}{2\pi} \int_{(1-d\ell)\Lambda f(\theta_\mathbf{k})}^{\Lambda f(\theta_\mathbf{k})} \frac{dk}{2\pi} k\hat{G}_0(i\omega, \mathbf{k}) \otimes \hat{G}_0(\pm i\omega, \pm\mathbf{k})$$

$$= \frac{\Lambda^2}{2\pi}d\ell \int \frac{d\omega}{2\pi} \int_0^{2\pi} \frac{d\theta_\mathbf{k}}{2\pi} f^2(\theta_\mathbf{k}) \frac{\sum_{i=0}^3 q_i\sigma_i \otimes \sigma_i}{\mathcal{G}_\Lambda(i\omega)\mathcal{G}_\Lambda(\pm i\omega)}. \quad (A.15)$$

where $\mathcal{G}_\Lambda(i\omega) = (i\omega + \mu - \frac{\lambda\Lambda^2}{\sqrt{2m}})^2 - \left(\frac{\Lambda^2}{2m}\right)^2(1 + \cos(2\eta)\cos(4\theta_\mathbf{k}))$ and

$$q_0 = \left(i\omega + \mu - \frac{\lambda\Lambda^2}{\sqrt{2m}}\right)\left(\pm i\omega + \mu - \frac{\lambda\Lambda^2}{\sqrt{2m}}\right)$$

$$q_1 = 2\left(\frac{\Lambda^2}{2m}\right)^2 \sin^2\eta\sin^2 2\theta_\mathbf{k} \quad (A.16)$$

$$q_3 = 2\left(\frac{\Lambda^2}{2m}\right)^2 \cos^2\eta\cos^2 2\theta_\mathbf{k}$$

. Below we consider (A.15) separately for the particle-hole and particle-particle cases, which correspond to the upper and lower signs in the above equation, respectively.

For the particle-hole case, we find that the dependence on μ, λ, and $f(\theta_\mathbf{k})$ disappears upon integrating over frequencies:

$$\int_> \hat{G}_0(+) \otimes \hat{G}_0(+) = \frac{m}{4\pi} d\ell \int \frac{d\theta_{\mathbf{k}}}{2\pi} \left\{ -\frac{1}{\sqrt{1 + \cos(2\eta)\cos(4\theta_{\mathbf{k}})}} 1_2 \otimes 1_2 \right.$$
$$\left. + 2 \frac{\cos^2(\eta)\cos^2(2\theta_{\mathbf{k}})\sigma_3 \otimes \sigma_3 + \sin^2(\eta)\sin^2(2\theta_{\mathbf{k}})\sigma_1 \otimes \sigma_1}{[1 + \cos(2\eta)\cos(4\theta_{\mathbf{k}})]^{3/2}} \right\} \quad \text{(A.17)}$$

The angular integrals in this expression can be performed using special functions, leading to the following result:

$$\int_> \hat{G}_0(+) \otimes \hat{G}_0(+) = \frac{m}{4\pi} d\ell \left[-A^{(ph)} 1_2 \otimes 1_2 + \frac{1}{2} B^{(ph)} \sigma_3 \otimes \sigma_3 + \frac{1}{2} C^{(ph)} \sigma_1 \otimes \sigma_1 \right], \quad \text{(A.18)}$$

where

$$A^{(ph)}(\tilde{\mu}, \lambda, \eta) = \frac{2}{\pi\sqrt{1+c_\eta}} K\left(\frac{2c_\eta}{1+c_\eta}\right) \quad \text{(A.19)}$$

$$B^{(ph)}(\tilde{\mu}, \lambda, \eta) = (1 + c_\eta) \left[{}_2F_1\left(\frac{3}{4}, \frac{5}{4}; 1; c_\eta^2\right) - \frac{3}{4} c_{\eta 2} F_1\left(\frac{5}{4}, \frac{7}{4}; 2; c_\eta^2\right) \right] \quad \text{(A.20)}$$

$$C^{(ph)}(\tilde{\mu}, \lambda, \eta) = (1 - c_\eta) \left[{}_2F_1\left(\frac{3}{4}, \frac{5}{4}; 1; c_\eta^2\right) + \frac{3}{4} c_{\eta 2} F_1\left(\frac{5}{4}, \frac{7}{4}; 2; c_\eta^2\right) \right]. \quad \text{(A.21)}$$

We now turn to the particle-particle version of (A.15), defining the following coefficients:

$$\int_> \hat{G}_0(+) \otimes \hat{G}_0(-) = \frac{m}{4\pi} d\ell$$
$$\left[A^{(pp)}(\tilde{\mu}, \lambda, \eta) 1_2 \otimes 1_2 + \frac{1}{2} B^{(pp)}(\tilde{\mu}, \lambda, \eta)\sigma_3 \otimes \sigma_3 + \frac{1}{2} C^{(pp)}(\tilde{\mu}, \lambda, \eta)\sigma_1 \otimes \sigma_1 \right]. \quad \text{(A.22)}$$

In the most general case, the angular integrals in (A.19) must be evaluated numerically, which greatly increases the computational cost of solving the flow equations. In light

of this, we consider two special cases. In the first case, we do not assume particle-hole symmetry but do assume rotational invariance, so that $\eta = \frac{\pi}{4}$, but λ is arbitrary. In this case we simply choose $f(\theta_{\mathbf{k}}) = 1$, so that the UV cutoff has no angular dependence. Performing the integrals in (A.19), one obtains

$$A^{(pp)}(\tilde{\mu}, \lambda, \frac{\pi}{4}) = B^{(pp)}(\tilde{\mu}, \lambda, \frac{\pi}{4}) = C^{(pp)}(\tilde{\mu}, \lambda, \frac{\pi}{4}) = \frac{1}{(1 + \sqrt{2}\lambda)^2 - \tilde{\mu}^2}. \tag{A.23}$$

In the second case we allow for angular anisotropy, but require particle-hole symmetry (λ=0). In order that the UV cutoff describes a contour of constant energy, we choose in this case $f(\theta_{\mathbf{k}}) = 1/[1 + \cos(2\eta)\cos(4\theta_{\mathbf{k}})]^{1/4}$, so that $\varepsilon_+(\mathbf{k})|_{\Lambda f(\theta_{\mathbf{k}})} = \Lambda^2/2m$, which is independent of $\theta_{\mathbf{k}}$. Then performing the angular integrals from (A.19), one obtains the following result:

$$A^{(pp)}(\tilde{\mu}, 0, \eta) = \frac{2}{\pi\sqrt{1 + c_\eta}} \frac{1}{1 - \tilde{\mu}^2} K\left(\frac{2c_\eta}{1 + c_\eta}\right) \tag{A.24}$$

$$B^{(pp)}(\tilde{\mu}, 0, \eta) = \frac{1 + c_\eta}{1 - \tilde{\mu}^2} \left[{}_2F_1\left(\frac{3}{4}, \frac{5}{4}; 1; c_\eta^2\right) - \frac{3}{4} c_{\eta 2} F_1\left(\frac{5}{4}, \frac{7}{4}; 2; c_\eta^2\right)\right] \tag{A.25}$$

$$C^{(pp)}(\tilde{\mu}, 0, \eta) = \frac{1 - c_\eta}{1 - \tilde{\mu}^2} \left[{}_2F_1\left(\frac{3}{4}, \frac{5}{4}; 1; c_\eta^2\right) + \frac{3}{4} c_{\eta 2} F_1\left(\frac{5}{4}, \frac{7}{4}; 2; c_\eta^2\right)\right]. \tag{A.26}$$

In the case where we assume rotational invariance and particle-hole symmetry such that $\eta = \frac{\pi}{4}$ and $\lambda = 0$, we obtain from (A.19) and either (A.24) or (A.23) the following
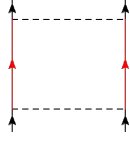
Figure A.3: Particle-particle diagram contributing to the one-loop flow equations for the couplings $g_i(\ell)$

coefficients:

$$A^{ph} = B^{ph} = C^{ph} = 1, \tag{A.27}$$

$$A^{pp} = B^{pp} = C^{pp} = \frac{1}{1 - \tilde{\mu}_\ell^2}, \tag{A.28}$$

which corresponds to the case analyzed in the main text.

With these results, we can proceed to calculate the coefficients in the flow equations. There are five marginally relevant one-loop diagrams which contribute to the coupling flows (2.6), shown in Figures **??** and A.3. Let $A_{ijk} = \sum_{d=1}^{5} A_{ijk}^5$, where d corresponds to one of these five diagrams.

The first diagram only gives diagonal contributions:

$$\begin{aligned}
A_{iii}^1 = \big[&- 4A^{ph} + C^{ph} \ \mathrm{Tr}((\sigma_1\sigma_j)^2) \\
&+ B^{ph} \ \mathrm{Tr}((\sigma_3\sigma_j)^2)\big] \frac{m}{4\pi}.
\end{aligned} \tag{A.29}$$

From the second and third diagrams combined:

$$\begin{aligned}
A_{iij}^2 + A_{iij}^3 = \frac{m}{4\pi}\bigg[&A^{ph} \ \mathrm{Tr}(\sigma_i\sigma_j\sigma_i\sigma_j) \\
&- \frac{1}{2}C^{ph} \ \mathrm{Tr}(\sigma_i\sigma_j\sigma_1\sigma_i\sigma_1\sigma_j) - \frac{1}{2}B^{ph} \ \mathrm{Tr}(\sigma_i\sigma_j\sigma_3\sigma_i\sigma_3\sigma_j)\bigg].
\end{aligned} \tag{A.30}$$

From the fourth diagram:

142

$$A_{ijk}^4 = \frac{m}{32\pi} \Bigg[2A^{ph} \, \mathrm{Tr}(\sigma_k\sigma_j\sigma_i) \, \mathrm{Tr}(\sigma_j\sigma_k\sigma_i)$$
$$- C^{ph} \, \mathrm{Tr}(\sigma_k\sigma_1\sigma_j\sigma_i) \, \mathrm{Tr}(\sigma_j\sigma_1\sigma_k\sigma_i) \qquad (A.31)$$
$$- B^{ph} \, \mathrm{Tr}(\sigma_k\sigma_3\sigma_j\sigma_i) \, \mathrm{Tr}(\sigma_j\sigma_3\sigma_k\sigma_i) \Bigg].$$

And from the fifth diagram:

$$A_{ijk}^5 = -\frac{m}{32\pi} \Bigg[2A^{pp} \left(\mathrm{Tr}(\sigma_k\sigma_j\sigma_i) \right)^2$$
$$+ C^{pp} \left(\mathrm{Tr}(\sigma_k\sigma_1\sigma_j\sigma_i) \right)^2 \qquad (A.32)$$
$$+ B^{pp} \left(\mathrm{Tr}(\sigma_k\sigma_3\sigma_j\sigma_i) \right)^2 \Bigg]$$

The flows of the source terms introduced in (2.8) are computed by evaluating the diagrams shown in Figure A.4. Evaluating these diagrams gives the following expressions for the coefficients :

$$B_{ij}^{(c,s)}(1) = \frac{m}{4\pi}\{-A^{ph}\mathrm{Tr}[(\sigma_j 1)M_i^{(c,s)}] + \frac{1}{2}B^{ph}\mathrm{Tr}[(\sigma_j 1)(\sigma_3 1)M_i^{(c,s)}(\sigma_3 1)]$$
$$+ \frac{1}{2}C^{ph}\mathrm{Tr}[(\sigma_j 1)(\sigma_1 1)M_i^{(c,s)}(\sigma_1 1)]\}, \qquad (A.33)$$

$$B_{ij}^{(c,s)}(2) = -\frac{m}{16\pi}\{-A^{ph}\mathrm{Tr}[((\sigma_j 1)M_i^{(c,s)})^2]$$
$$+ \frac{1}{2}B^{ph}\mathrm{Tr}[M_i^{(c,s)}(\sigma_j 1)(\sigma_3 1)M_i^{(c,s)}(\sigma_3 1)(\sigma_j 1)] \qquad (A.34)$$
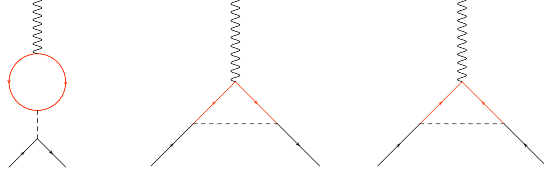$$+ \frac{1}{2}C^{ph}\mathrm{Tr}[M_i^{(c,s)}(\sigma_j 1)(\sigma_1 1)M_i^{(c,s)}(\sigma_1 1)(\sigma_j 1)]\},$$

Figure A.4: One-loop diagrams representing contributions to the source terms $\Delta_i^{c,s,pp}(\ell)$.

$$
\begin{aligned}
B_{ij}^{(pp)} = -\frac{m}{16\pi}\Big\{ &A^{pp}\mathrm{Tr}[(\sigma_j 1)M_i^{(pp)}(\sigma_j 1)^T M_i^{(pp)}] + \frac{1}{2}B^{pp}\mathrm{Tr}[M_i^{(pp)}(\sigma_j 1)(\sigma_3 1)M_i^{(pp)}(\sigma_3 1)(\sigma_j 1)^T] \\
&+ \frac{1}{2}C^{pp}\mathrm{Tr}[M_i^{(pp)}(\sigma_j 1)(\sigma_1 1)M_i^{(pp)}(\sigma_1 1)(\sigma_j 1)^T]\Big\}.
\end{aligned}
$$
(A.35)

Adding the contributions from the first two diagrams together then gives $B_{ij}^{(c,s)} = B_{ij}^{(c,s)}(1) + B_{ij}^{(c,s)}(2)$. By differentiating the free energy with respect to the source terms, one obtains the following expression for the particle-hole susceptibilities in the charge and spin channels:

$$
\begin{aligned}
\chi_i^{(c,s)}(\ell) = \frac{m}{4\pi}\int_0^\ell d\ell' e^{2\Omega_i^{(c,s)}(\ell')}\Big\{ &4A^{ph} \\
&- \frac{1}{2}B^{ph}\mathrm{Tr}[((\sigma_3 1)M_i)^2] - \frac{1}{2}C^{ph}\mathrm{Tr}[((\sigma_1 1)M_i)^2]\Big\},
\end{aligned}
$$
(A.36)

where

$$
\Omega_i^{(c,s)}(\ell) = \int_0^\ell d\ell' \sum_{j=0}^3 B_{ij}^{(c,s)} g_j(\ell').
$$
(A.37)

The particle-particle susceptibilities are given by

144

$$\chi_i^{pp}(\ell) = \frac{m}{4\pi} \int_0^\ell d\ell' e^{2\Omega_i^{pp}(\ell')} \left\{ 4A^{pp} \right.$$
$$\left. + \frac{1}{2} B^{pp} \mathrm{Tr}[((\sigma_3 1)M_i)^2] + \frac{1}{2} C^{pp} \mathrm{Tr}[((\sigma_1 1)M_i)^2] \right\},$$

(A.38)

where

$$\Omega_i^{pp}(\ell) = \int_0^\ell d\ell' \sum_{j=0}^3 B_{ij}^{pp} g_j(\ell').$$

(A.39)

Having determined the complete flow equations for the couplings and susceptibilites, we can proceed to solve the coupled differential flow equations given initial conditions $g_i(0)$ and $\mu(0)$. We assume that $-\frac{1}{\sqrt{2}} < \lambda < \frac{1}{\sqrt{2}}$, so that the bands do not cross the Fermi level away from the point $\mathbf{k} = 0$. The phase instability is taken to be the in the channel in which the susceptibility χ_i is the largest when the couplings reach values $|g_i(\ell)| \gtrsim 1$. The phase diagrams obtained in this way are shown in Figure A.5.

A.2.1 Anisotropic case

Let us now generalize the discussion by moving away from the rotationally invariant and particle-hole symmetric limit by including arbitrary η and λ in the flow calculations, which is done explicitly in the second portion of the Appendix. Solving these modified RG equations leads to the phase diagrams shown in Figure A.5. In calculating these phase diagrams, the leading instabilities are determined by taking the largest susceptibility when the couplings attain values $|g_i(\ell)| \gtrsim 1$. Another possible criterion for determining
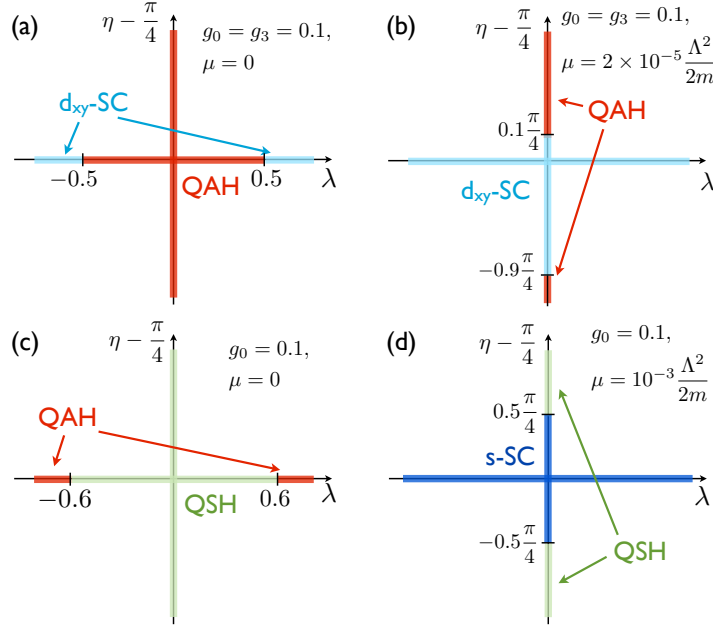
Figure A.5: Phase instabilities at various values of angular anisotropy $\eta - \frac{\pi}{4}$ and particle-hole asymmetry λ. Top row: Hubbard interaction (for a checkerboard lattice) at zero doping (a) and with doping (b), with instabilities to quantum anomalous Hall (QAH) and d-wave superconducting (d-SC) phases. Bottom row: longer-ranged forward scattering interaction at zero doping (c) and with doping (d), with instabilities to QAH, quantum spin Hall (QSH), and s-wave superconducting (s-SC) phases.

phases is to take the largest susceptibility exponent γ where the flows diverge. The phase diagrams resulting from this choice are qualitatively similar to those shown in Figure A.5, with the only significant differences appearing for forward scattering interaction, with an s-wave superconducting phase rather than QAH at $|\lambda| > 0.2$ at $\mu = 0$, and a superconducting phase with degenerate d_{xy} and $d_{x^2-y^2}$ order parameters (leading to a chiral, "$d + id$" superconducting state) appearing at $\mu = 10^{-3}\frac{\Lambda^2}{2m}$ and $\lambda < -0.6$.

Finally, let us consider the case of the kagome lattice as an example of a C_{6v}-symmetric system, in which case η is fixed to $\frac{\pi}{4}$. A tight-binding calculation with nearest-neighbor hopping leads to three energy bands, with a completely flat upper band touching a parabolically dispersing middle band at $\mathbf{k} = 0$, as shown in Figure A.6. Thus, the system
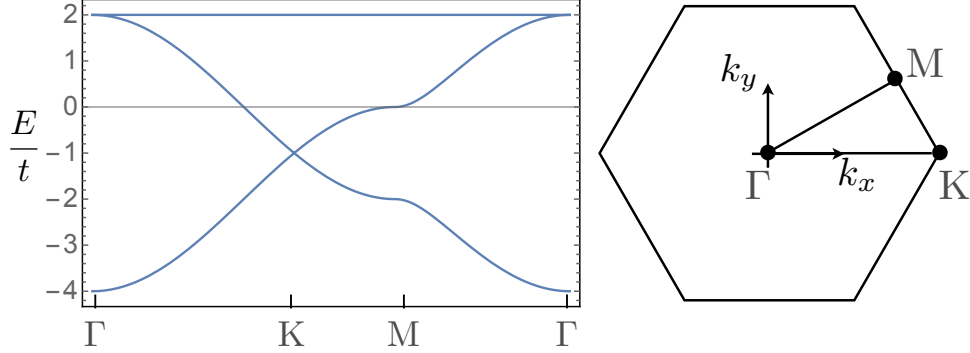
Figure A.6: Band structure for fermions on the kagome lattice with nearest-neighbor hopping t. A quadratic band touching point occurs between the upper and middle bands at the Γ point ($\mathbf{k} = 0$).

near $\frac{2}{3}$ filling corresponds to a QBC in the extreme particle-hole asymmetric case where $\lambda = -1/\sqrt{2}$. The two-band low energy effective theory introduced in the main text can be obtained by projecting out the completely filled lowermost band, after which the two components of the spinor ψ_σ correspond to different linear combinations of the three fermion operators defined on the three sublattices. Starting with a microscopic Hubbard interaction in the lattice model and performing the projection onto the low-energy effective theory leads to the Hubbard interaction shown in Table 2.1, which is distinct from the form of the Hubbard interaction on the checkerboard lattice. Thus, although the two systems are described by the same effective field theory (at least in the case where $t_x = t_z$), knowledge of the original lattice model is retained through the form of the interactions. In fact, this can even affect which phase is realized. For the C_{6v}-symmetric system at $\mu = 0$, Hubbard interaction leads to a QSH phase for $|\lambda| < 0.98/\sqrt{2}$ and QAH for $0.98/\sqrt{2} < |\lambda| < 1/\sqrt{2}$, which is very different from the behavior shown in Figure A.5(a). In the case with one nearly flat band ($|\lambda| \lesssim 1/\sqrt{2}$), the couplings $\tilde{g}_i(\ell)$ turn out to all remain positive until very large values of ℓ, with $C_1 \equiv \ell_1 g \gtrsim 10$.

147

According to the condition (2.22), then, superconductivity is only to be expected in a vanishingly small range of μ for any bare interaction strength $g \lesssim 1$. Rather than leading to superconductivity, the coupling flows terminate when the UV cutoff reaches the Fermi energy, and the resulting phase in this case is a Fermi liquid.

Appendix B

MAMMs

B.1 From Ricci flow to RG equation

In this appendix, we discuss the effect of anisotropy on the noncollinear spin density wave from a geometric point of view. As we argued in the main text, the ground state manifold of the noncollinear spin density wave is a three dimensional manifold, which will be deformed by the Zeeman field. Thus the noncollinear spin density wave can be generally described by the NLSM

$$\mathcal{S}\left[X\right] = \int \frac{1}{2} G_{ab}\left[X\right] dX^a \wedge \star dX^b + \dots \tag{B.1}$$

where the bosonic field X is introduced as

$$\begin{pmatrix} X^1 \\ X^2 \\ X^3 \\ \sqrt{1-|X|^2} \end{pmatrix} = \begin{pmatrix} \mathrm{Re} z_1 \\ \mathrm{Im} z_1 \\ \mathrm{Re} z_2 \\ \mathrm{Im} z_2 \end{pmatrix}, \tag{B.2}$$

and the metric G_{ab} should carry the information of the external Zeeman field which lowers the symmetry of the system. In our choice here, $X_i = 0$ corresponds to the ground state $|z_1|^2 = 0, |z_2|^2 = 1$.

To describe the geometric evolution of the target manifold more precisely, we need to introduce our conventions of geometric quantities. The affine connection is defined as

$$\Gamma^a_{\ bc} = \frac{1}{2} G^{ae} \left(-\partial_e G_{bc} + \partial_c G_{be} + \partial_b G_{ce}\right),$$ (B.3)

where $\partial_a = \frac{\partial}{\partial X^a}$ is the derivative with respect to the field X_i. This connection gives the Riemann curvature

$$R^a_{\ bcd} = \partial_c \Gamma^a_{\ db} - \partial_d \Gamma^a_{\ cb} + \Gamma^a_{\ ce} \Gamma^e_{\ db} - \Gamma^a_{\ de} \Gamma^e_{\ cb},$$ (B.4)

and its contraction

$$\mathcal{R}_{ab} = R^c_{\ acb}$$ (B.5)

is called the Ricci tensor. The action Eq. B.1 is invariant under coordinate transformations which preserve the distance $G_{ab} dX^a dX^b$.

Friedan [30, 31] proved that the one-loop beta function of G_{ab} corresponds to the Ricci flow

$$\frac{dG_{ab}}{d \ln l} = -\frac{1}{2\pi} \mathcal{R}_{ab} + \dots$$ (B.6)

Then the central task is to explore how the external Zeeman field affects the Ricci flow. Let us first consider the simpler case without the Zeeman field. The metric G_{ab} obtained

from the isotropic O(4) NLSM reads

$$G_{ab}[X] = \frac{1}{g}\left(\delta_{ab} + \frac{X^a X^b}{1 - |X|^2}\right), \tag{B.7}$$

The Ricci tensor is given by

$$\mathcal{R}_{ab}[X] = 2g G_{ab}[X], \tag{B.8}$$

which is proportional to the metric. Using Eq. B.6, we obtain the RG flow Eq. 4.37 of the coupling constant g.

After turning on the Zeeman term, the O(4) symmetry is broken, and the NLSM is modified as Eq. 4.44. The metric now becomes

$$G_{ab}[X] = \begin{pmatrix} \frac{1}{g_1} & 0 & 0 \\ 0 & \frac{1}{g_1} & 0 \\ 0 & 0 & \frac{1}{g_2} \end{pmatrix} + \frac{1}{g_2}\frac{X^a X^b}{1 - |X|^2}. \tag{B.9}$$

The complete expression of the Ricci tensor in this case is rather complicated. To read the RG flow of g_1, g_2 from the Ricci flow, we consider the Ricci tensor at point $X_i = 0$, which corresponds to the ordering of z_2 at zero temperature, and it is the order favored by the Zeeman field:

$$\mathcal{R}_{ab}[X \to 0] = \begin{pmatrix} 1 + \frac{g_1}{g_2} & 0 & 0 \\ 0 & 1 + \frac{g_1}{g_2} & 0 \\ 0 & 0 & \frac{2g_1}{g_2} \end{pmatrix}. \tag{B.10}$$

Combining with the value of $G_{ab}[X]$ at $X_i = 0$, we obtain the RG flow Eq. 4.46 of g_1 and g_2.

If we start with initial values $g_1 = g$ and $g_2 = (1 - \alpha)g$, the solution of the RG

151

equation Eq. 4.46 reads

$$
\begin{aligned}
g_1(l) &= \frac{\pi g}{\pi - g \ln l} \\
&+ \frac{g\pi^{3/2}\left(-\pi + g \ln l + \sqrt{\pi(\pi - g \ln l)}\right)\alpha}{(\pi - g \ln l)^{5/2}} + O(\alpha^2), \\[2ex]
g_2(l) &= \frac{\pi g}{\pi - g \ln l} \\
&+ \frac{g\left(\pi^2 - 2\pi^{3/2}\sqrt{\pi - g \ln l}\right)\alpha}{(\pi - g \ln l)^2} + O(\alpha^2).
\end{aligned}
\tag{B.11}
$$

Bibliography

[1]

[2] Alexander Altland, Dmitry Bagrets, and Alex Kamenev. Syk non fermi liquid correlations in nanoscopic quantum transport. *arXiv preprint arXiv:1908.11351*, 2019.

[3] Alexander Altland, Dmitry Bagrets, and Alex Kamenev. Syk non fermi liquid correlations in nanoscopic quantum transport. *arXiv preprint arXiv:1908.11351*, 2019.

[4] Francisco Barahona. On the computational complexity of ising spin glass models. *Journal of Physics A: Mathematical and General*, 15(10):3241, 1982.

[5] B Andrei Bernevig, Taylor L Hughes, and Shou-Cheng Zhang. Quantum spin hall effect and topological phase transition in hgte quantum wells. *science*, 314(5806):1757–1761, 2006.

[6] B Bernu, P Lecheminant, C Lhuillier, and L Pierre. N$\vec{e}$el order versus spin liquid in quantum heisenberg antiferromagnets on triangular and kagom$\vec{e}$ lattices. *Physica Scripta*, 1993(T49A):192, 1993.

[7] Zhen Bi, Chao-Ming Jian, Yi-Zhuang You, Kelly Ann Pawlak, and Cenke Xu. Instability of the non-fermi-liquid state of the sachdev-ye-kitaev model. *Physical Review B*, 95(20):205105, 2017.

[8] Rafi Bistritzer and Allan H MacDonald. Moir$\vec{e}$ bands in twisted double-layer graphene. *Proceedings of the National Academy of Sciences*, 108(30):12233–12237, 2011.

[9] Nick Bultinck, Shubhayu Chatterjee, and Michael P Zaletel. Anomalous hall ferromagnetism in twisted bilayer graphene. *arXiv preprint arXiv:1901.08110*, 2019.

[10] Yuan Cao, Debanjan Chowdhury, Daniel Rodan-Legrain, Oriol Rubies-Bigorda, Kenji Watanabe, Takashi Taniguchi, T Senthil, and Pablo Jarillo-Herrero. Strange metal in magic-angle graphene with near planckian dissipation. *Physical Review Letters*, 124(7):076801, 2020.

[11] Yuan Cao, Valla Fatemi, Ahmet Demir, Shiang Fang, Spencer L Tomarken, Jason Y Luo, Javier D Sanchez-Yamagishi, Kenji Watanabe, Takashi Taniguchi, Efthimios Kaxiras, et al. Correlated insulator behaviour at half-filling in magic-angle graphene superlattices. *Nature*, 556(7699):80, 2018.

[12] Yuan Cao, Valla Fatemi, Shiang Fang, Kenji Watanabe, Takashi Taniguchi, Efthimios Kaxiras, and Pablo Jarillo-Herrero. Unconventional superconductivity in magic-angle graphene superlattices. *Nature*, 556(7699):43–50, 2018.

[13] Cui-Zu Chang, Jinsong Zhang, Xiao Feng, Jie Shen, Zuocheng Zhang, Minghua Guo, Kang Li, Yunbo Ou, Pang Wei, Li-Li Wang, et al. Experimental observation of the quantum anomalous hall effect in a magnetic topological insulator. *Science*, 340(6129):167–170, 2013.

[14] Guorui Chen, Lili Jiang, Shuang Wu, Bosai Lyu, Hongyuan Li, Bheema Lingam Chittari, Kenji Watanabe, Takashi Taniguchi, Zhiwen Shi, Jeil Jung, et al. Evidence of gate-tunable mott insulator in trilayer graphene-boron nitride moir\'e superlattice. *arXiv preprint arXiv:1803.01985*, 2018.

[15] Guorui Chen, Aaron L Sharpe, Eli J Fox, Ya-Hui Zhang, Shaoxin Wang, Lili Jiang, Bosai Lyu, Hongyuan Li, Kenji Watanabe, Takashi Taniguchi, et al. Tunable correlated chern insulator and ferromagnetism in trilayer graphene/boron nitride moir\'e superlattice. *arXiv preprint arXiv:1905.06535*, 2019.

[16] Guorui Chen, Aaron L Sharpe, Patrick Gallagher, Ilan T Rosen, Eli Fox, Lili Jiang, Bosai Lyu, Hongyuan Li, Kenji Watanabe, Takashi Taniguchi, et al. Signatures of gate-tunable superconductivity in trilayer graphene/boron nitride moir\'e superlattice. *arXiv preprint arXiv:1901.04621*, 2019.

[17] Bheema Lingam Chittari, Guorui Chen, Yuanbo Zhang, Feng Wang, and Jeil Jung. Gate-tunable topological flat bands in trilayer graphene boron-nitride moir$\vec{e}$ superlattices. *Physical review letters*, 122(1):016401, 2019.

[18] Andrey V Chubukov, Subir Sachdev, and T Senthil. Quantum phase transitions in frustrated two-dimensional antiferromagnets. *arXiv preprint cond-mat/9402006*, 1994.

[19] Denis Dalidovich and Sung-Sik Lee. Perturbative non-fermi liquids from dimensional regularization. *Physical Review B*, 88(24):245106, 2013.

[20] Ippei Danshita, Masanori Hanada, and Masaki Tezuka. Creating and probing the sachdev–ye–kitaev model with ultracold gases: Towards experimental studies of quantum gravity. *Progress of Theoretical and Experimental Physics*, 2017(8), 2017.

[21] G Trambly De Laissardière, Didier Mayou, and Laurence Magaud. Numerical studies of confined states in rotated bilayers of graphene. *Physical Review B*, 86(12):125413, 2012.

[22] Fabien M Décaillot, Manija A Kazmi, Ying Lin, Sarmistha Ray-Saha, Thomas P Sakmar, and Pallavi Sachdev. Cxcr7/cxcr4 heterodimer constitutively recruits β-arrestin to enhance cell migration. *Journal of Biological Chemistry*, 286(37):32188–32197, 2011.

[23] John F Dodaro, Steven A Kivelson, Yoni Schattner, Xiao-Qi Sun, and Chao Wang. Phases of a phenomenological model of twisted bilayer graphene. *Physical Review B*, 98(7):075154, 2018.

[24] JMB Lopes Dos Santos, NMR Peres, and AH Castro Neto. Graphene bilayer with a twist: Electronic structure. *Physical review letters*, 99(25):256802, 2007.

[25] Vincent Dubost. Une initiation aux concepts et matériaux de la transition métal-isolant de mott. 2014.

[26] Julius Engelsöy, Thomas G Mertens, and Herman Verlinde. An investigation of ads 2 backreaction and holography. *Journal of High Energy Physics*, 2016(7):139, 2016.

[27] Shiang Fang and Efthimios Kaxiras. Electronic structure theory of weakly interacting bilayers. *Physical Review B*, 93(23):235153, 2016.

[28] Maciej Fidrysiak, Michal Zegrodnik, and Józef Spalek. Unconventional topological superconductivity and phase diagram for an effective two-orbital model as applied to twisted bilayer graphene. *Physical Review B*, 98(8):085436, 2018.

[29] Eduardo Fradkin, Steven A Kivelson, and John M Tranquada. Colloquium: Theory of intertwined orders in high temperature superconductors. *Reviews of Modern Physics*, 87(2):457, 2015.

[30] Daniel Friedan. Nonlinear models in 2+ ε dimensions. *Physical Review Letters*, 45(13):1057, 1980.

[31] Daniel Harry Friedan. Nonlinear models in 2+ ε dimensions. *Annals of Physics*, 163(2):318–419, 1985.

[32] Wenbo Fu, Davide Gaiotto, Juan Maldacena, and Subir Sachdev. Supersymmetric sachdev-ye-kitaev models. *Physical Review D*, 95(2):026009, 2017.

[33] Wenbo Fu and Subir Sachdev. Numerical study of fermion and boson models with infinite-range random interactions. *Physical Review B*, 94(3):035135, 2016.

[34] Wenbo Fu and Subir Sachdev. Numerical study of fermion and boson models with infinite-range random interactions. *Physical Review B*, 94(3):035135, 2016.

[35] Antonio M Garcı̄a-Garcı̄a and Jacobus JM Verbaarschot. Spectral and thermodynamic properties of the sachdev-ye-kitaev model. *Physical Review D*, 94(12):126010, 2016.

[36] David J Gross and Vladimir Rosenhaus. A generalization of sachdev-ye-kitaev. *Journal of High Energy Physics*, 2017(2):93, 2017.

[37] Yingfei Gu, Xiao-Liang Qi, and Douglas Stanford. Local criticality, diffusion and chaos in generalized sachdev-ye-kitaev models. *Journal of High Energy Physics*, 2017(5):125, 2017.

[38] F Duncan M Haldane. Model for a quantum hall effect without landau levels: Condensed-matter realization of the" parity anomaly". *Physical review letters*, 61(18):2015, 1988.

[39] FDM Haldane. Berry curvature on the fermi surface: anomalous hall effect as a topological fermi-liquid property. *Physical review letters*, 93(20):206602, 2004.

[40] John A Hertz. Quantum critical phenomena. *Physical Review B*, 14(3):1165, 1976.

[41] Shinobu Hikami and Toshihiko Tsuneto. Phase transition of quasi-two dimensional planar system. *Progress of Theoretical Physics*, 63(2):387–401, 1980.

[42] Daniel Ish and Mark Srednicki. The sachdev-ye-kitaev model and free majorana variational states, 2020.

[43] Kristan Jensen. Chaos in ads 2 holography. *Physical review letters*, 117(11):111601, 2016.

[44] Kristan Jensen. Chaos in ads 2 holography. *Physical review letters*, 117(11):111601, 2016.

[45] Chao-Ming Jian, Zhen Bi, and Cenke Xu. Model for continuous thermal metal to insulator transition. *Physical Review B*, 96(11):115122, 2017.

[46] Chao-Ming Jian, Alex Thomson, Alex Rasmussen, Zhen Bi, and Cenke Xu. Deconfined quantum critical point on the triangular lattice. *Physical Review B*, 97(19):195115, 2018.

[47] Charles L Kane and Eugene J Mele. Z 2 topological order and the quantum spin hall effect. *Physical review letters*, 95(14):146802, 2005.

[48] Jian Kang and Oskar Vafek. Strong coupling phases of partially filled twisted bilayer graphene narrow bands. *Physical review letters*, 122(24):246401, 2019.

[49] Aharon Kapitulnik, Jing Xia, Elizabeth Schemm, and Alexander Palevski. Polar kerr effect as probe for time-reversal symmetry breaking in unconventional superconductors. *New Journal of Physics*, 11(5):055060, 2009.

[50] A Kitaev. Aip conf. proc. 1134, 22. 2009.

[51] A Yu Kitaev. Fault-tolerant quantum computation by anyons. *Annals of Physics*, 303(1):2–30, 2003.

[52] Markus König, Steffen Wiedmann, Christoph Brüne, Andreas Roth, Hartmut Buhmann, Laurens W Molenkamp, Xiao-Liang Qi, and Shou-Cheng Zhang. Quantum spin hall insulator state in hgte quantum wells. *Science*, 318(5851):766–770, 2007.

[53] John Michael Kosterlitz and David James Thouless. Ordering, metastability and phase transitions in two-dimensional systems. *Journal of Physics C: Solid State Physics*, 6(7):1181, 1973.

[54] Chethan Krishnan, Sambuddha Sanyal, and PN Bala Subramanian. Quantum chaos and holographic tensor models. *Journal of High Energy Physics*, 2017(3):56, 2017.

[55] Sung-Sik Lee. Low-energy effective theory of fermi surface coupled with u (1) gauge field in 2+ 1 dimensions. *Physical Review B*, 80(16):165102, 2009.

[56] Maxime Leroux, Vivek Mishra, Jacob PC Ruff, Helmut Claus, Matthew P Smylie, Christine Opagiste, Pierre Rodière, Asghar Kayani, GD Gu, John M Tranquada, et al. Disorder raises the critical temperature of a cuprate superconductor. *Proceedings of the National Academy of Sciences*, 116(22):10691–10697, 2019.

[57] Jianpeng Liu, Zhen Ma, Jinhua Gao, and Xi Dai. Quantum valley hall effect, orbital magnetism, and anomalous hall effect in twisted multilayer graphene systems. *Physical Review X*, 9(3):031021, 2019.

[58] Xiaomeng Liu, Zeyu Hao, Eslam Khalaf, Jong Yeon Lee, Kenji Watanabe, Takashi Taniguchi, Ashvin Vishwanath, and Philip Kim. Spin-polarized correlated insulator and superconductor in twisted double bilayer graphene. *arXiv preprint arXiv:1903.08130*, 2019.

[59] Xiaomeng Liu, Zeyu Hao, Eslam Khalaf, Jong Yeon Lee, Kenji Watanabe, Takashi Taniguchi, Ashvin Vishwanath, and Philip Kim. Spin-polarized correlated insulator and superconductor in twisted double bilayer graphene. *arXiv preprint arXiv:1903.08130*, 2019.

[60] Hilbert v Löhneysen, Achim Rosch, Matthias Vojta, and Peter Wölfle. Fermi-liquid instabilities at magnetic quantum phase transitions. *Reviews of Modern Physics*, 79(3):1015, 2007.

[61] Yuan-Ming Lu. Symmetric z 2 spin liquids and their neighboring phases on triangular lattice. *Physical Review B*, 93(16):165113, 2016.

[62] Juan Maldacena, Stephen H Shenker, and Douglas Stanford. A bound on chaos. *Journal of High Energy Physics*, 2016(8):106, 2016.

[63] Ian P McCulloch. Infinite size density matrix renormalization group, revisited. *arXiv preprint arXiv:0804.2509*, 2008.

[64] Max A Metlitski, David F Mross, Subir Sachdev, and T Senthil. Cooper pairing in non-fermi liquids. *Physical Review B*, 91(11):115111, 2015.

[65] Max A Metlitski and Subir Sachdev. Quantum phase transitions of metals in two spatial dimensions. i. ising-nematic order. *Physical Review B*, 82(7):075127, 2010.

[66] Max A Metlitski and Subir Sachdev. Quantum phase transitions of metals in two spatial dimensions. ii. spin density wave order. *Physical Review B*, 82(7):075128, 2010.

[67] Marc Mézard, Giorgio Parisi, Nicolas Sourlas, Gérard Toulouse, and Miguel Virasoro. Replica symmetry breaking and the nature of the spin glass phase. *Journal de Physique*, 45(5):843–854, 1984.

[68] AJ Millis. Effect of a nonzero temperature on quantum critical points in itinerant fermion systems. *Physical Review B*, 48(10):7183, 1993.

[69] E Suárez Morell, JD Correa, P Vargas, M Pacheco, and Z Barticevic. Flat bands in slightly twisted bilayer graphene: Tight-binding calculations. *Physical Review B*, 82(12):121407, 2010.

[70] David F Mross, John McGreevy, Hong Liu, and T Senthil. Controlled expansion for certain non-fermi-liquid metals. *Physical Review B*, 82(4):045121, 2010.

[71] James M Murray and Oskar Vafek. Excitonic and superconducting orders from repulsive interaction on the doped honeycomb bilayer. *Physical Review B*, 89(20):205119, 2014.

[72] James M Murray and Oskar Vafek. Renormalization group study of interaction-driven quantum anomalous hall and quantum spin hall phases in quadratic band crossing systems. *Physical Review B*, 89(20):201110, 2014.

[73] AH Castro Neto, Francisco Guinea, Nuno MR Peres, Kostya S Novoselov, and Andre K Geim. The electronic properties of graphene. *Reviews of modern physics*, 81(1):109, 2009.

[74] Minh Ha Ngo, Takehisa Soma, Hwa-Young Youn, Kazuo Nishigaki, Hee Chun Chung, Nguyen Giap, Hyung-Joon Moon, Bong-Kyun Park, Genki Arikawa, Yoshinori Fujii, et al. Characteristics of reproduction of the water buffalo and techniques used to improve their reproductive performance. *Canadian journal of veterinary research*, 83(2):97–103, 2019.

[75] Johan Nilsson, AH Castro Neto, F Guinea, and NMR Peres. Electronic properties of bilayer and multilayer graphene. *Physical Review B*, 78(4):045405, 2008.

[76] Vadim Oganesyan, Steven A Kivelson, and Eduardo Fradkin. Quantum theory of a nematic fermi fluid. *Physical Review B*, 64(19):195109, 2001.

[77] SA Parameswaran and Romain Vasseur. Many-body localization, symmetry and topology. *Reports on Progress in Physics*, 81(8):082501, 2018.

[78] Kelly Ann Pawlak, James M Murray, and Oskar Vafek. Emergence of superconductivity in a doped single-valley quadratic band crossing system of spin-1 2 fermions. *Physical Review B*, 91(13):134509, 2015.

[79] Hoi Chun Po, Liujun Zou, Ashvin Vishwanath, and T Senthil. Origin of mott insulating behavior and superconductivity in twisted bilayer graphene. *Physical Review X*, 8(3):031089, 2018.

[80] Joseph Polchinski and Vladimir Rosenhaus. The spectrum in the sachdev-ye-kitaev model. *Journal of High Energy Physics*, 2016(4):1, 2016.

[81] N Read and Subir Sachdev. Some features of the phase diagram of the square lattice su (n) antiferromagnet. *Nuclear Physics B*, 316(3):609–640, 1989.

[82] Shinsei Ryu, Andreas P Schnyder, Akira Furusaki, and Andreas WW Ludwig. Topological insulators and superconductors: tenfold way and dimensional hierarchy. *New Journal of Physics*, 12(6):065010, 2010.

[83] Subir Sachdev. Kagom$\vec{e}$-and triangular-lattice heisenberg antiferromagnets: Ordering from quantum fluctuations and quantum-disordered ground states with unconfined bosonic spinons. *Physical Review B*, 45(21):12377, 1992.

[84] Subir Sachdev. Holographic metals and the fractionalized fermi liquid. *Physical review letters*, 105(15):151602, 2010.

[85] Subir Sachdev. Bekenstein-hawking entropy and strange metals. *Physical Review X*, 5(4):041025, 2015.

[86] Subir Sachdev and Jinwu Ye. Gapless spin-fluid ground state in a random quantum heisenberg magnet. *Physical review letters*, 70(21):3339, 1993.

[87] Subir Sachdev and Jinwu Ye. Gapless spin-fluid ground state in a random quantum heisenberg magnet. *Physical review letters*, 70(21):3339, 1993.

[88] Andreas P Schnyder, Shinsei Ryu, Akira Furusaki, and Andreas WW Ludwig. Advances in theoretical physics: Landau memorial conference. 1134(10), 2009.

[89] Ulrich Schollwöck. The density-matrix renormalization group. *Reviews of modern physics*, 77(1):259, 2005.

[90] Kangjun Seo, Valeri N Kotov, and Bruno Uchoa. Ferromagnetic mott state in twisted graphene bilayers at the magic angle. *Physical review letters*, 122(24):246402, 2019.

[91] Rev Shankar. Renormalization-group approach to interacting fermions. *Reviews of Modern Physics*, 66(1):129, 1994.

[92] Aaron L Sharpe, Eli J Fox, Arthur W Barnard, Joe Finney, Kenji Watanabe, Takashi Taniguchi, MA Kastner, and David Goldhaber-Gordon. Emergent ferromagnetism near three-quarters filling in twisted bilayer graphene. *Science*, 365(6453):605–608, 2019.

[93] Cheng Shen, Na Li, Shuopei Wang, Yanchong Zhao, Jian Tang, Jieying Liu, Jinpeng Tian, Yanbang Chu, Kenji Watanabe, Takashi Taniguchi, et al. Observation of superconductivity with tc onset at 12k in electrically tunable twisted double bilayer graphene. *arXiv preprint arXiv:1903.06952*, 2019.

[94] Xue-Yang Song, Yin-Chen He, Ashvin Vishwanath, and Chong Wang. From spinon band topology to the symmetry quantum numbers of monopoles in dirac spin liquids. *Physical Review X*, 10(1):011033, 2020.

[95] Xue-Yang Song, Chao-Ming Jian, and Leon Balents. Strongly correlated metal built from sachdev-ye-kitaev models. *Physical review letters*, 119(21):216601, 2017.

[96] Xue-Yang Song, Chong Wang, Ashvin Vishwanath, and Yin-Chen He. Unifying description of competing orders in two-dimensional quantum magnets. *Nature communications*, 10(1):1–12, 2019.

[97] S. Spielman, J. S. Dodge, L. W. Lombardo, C. B. Eom, M. M. Fejer, T. H. Geballe, and A. Kapitulnik. Measurement of the spontaneous polar kerr effect in $yba_2cu_3o_7$ and $bi_2sr_2cacu_2o_8$. *Phys. Rev. Lett.*, 68:3472–3475, Jun 1992.

[98] S Spielman, K Fesler, CB Eom, TH Geballe, MM Fejer, and A Kapitulnik. Test for nonreciprocal circular birefringence in yba 2 cu 3 o 7 thin films as evidence for broken time-reversal symmetry. *Physical review letters*, 65(1):123, 1990.

[99] Douglas Stanford. Many-body chaos at weak coupling. *Journal of High Energy Physics*, 2016(10):9, 2016.

[100] Kai Sun and Eduardo Fradkin. Time-reversal symmetry breaking and spontaneous anomalous hall effect in fermi fluids. *Physical Review B*, 78(24):245122, 2008.

[101] Kai Sun, Hong Yao, Eduardo Fradkin, and Steven A Kivelson. Topological insulators and nematic phases from spontaneous symmetry breaking in 2d fermi systems with a quadratic band crossing. *Physical review letters*, 103(4):046811, 2009.

[102] Uwe C Täuber, Martin Howard, and Benjamin P Vollmayr-Lee. Applications of field-theoretic renormalization group methods to reaction–diffusion problems. *Journal of Physics A: Mathematical and General*, 38(17):R79, 2005.

[103] Doug Toussaint and Frank Wilczek. Particle–antiparticle annihilation in diffusive motion. *The Journal of Chemical Physics*, 78(5):2642–2647, 1983.

[104] Gustavo J Turiaci and Herman Verlinde. Towards a 2d qft analog of the syk model. *Journal of High Energy Physics*, 2017(10):167, 2017.

[105] Stefan Uebelacker and Carsten Honerkamp. Instabilities of quadratic band crossing points. *Physical Review B*, 84(20):205122, 2011.

[106] Oskar Vafek. Interacting fermions on the honeycomb bilayer: From weak to strong coupling. *Physical Review B*, 82(20):205106, 2010.

[107] Oskar Vafek, James M Murray, and Vladimir Cvetkovic. Superconductivity on the brink of spin-charge order in a doped honeycomb bilayer. *Physical review letters*, 112(14):147002, 2014.

[108] Oskar Vafek and Kun Yang. Many-body instability of coulomb interacting bilayer graphene: Renormalization group approach. *Physical Review B*, 81(4):041401, 2010.

[109] Michael Vogl, Martin Rodriguez-Vega, and Gregory A Fiete. Tuning the magic angle of twisted bilayer graphene at the exit of a waveguide. *arXiv preprint arXiv:2001.04416*, 2020.

[110] Fa Wang and Ashvin Vishwanath. Spin-liquid states on the triangular and kagom$\vec{e}$ lattices: A projective-symmetry-group analysis of schwinger boson states. *Physical Review B*, 74(17):174423, 2006.

[111] Steven R White. Density matrix formulation for quantum renormalization groups. *Physical review letters*, 69(19):2863, 1992.

[112] Justin H Wilson, Yixing Fu, S Das Sarma, and JH Pixley. Disorder in twisted bilayer graphene. *arXiv preprint arXiv:1908.02753*, 2019.

[113] Edward Witten. An syk-like model without disorder. *Journal of Physics A: Mathematical and Theoretical*, 52(47):474002, 2019.

[114] Fengcheng Wu and Sankar Das Sarma. Identification of superconducting pairing symmetry in twisted bilayer graphene using in-plane magnetic field and strain. *Physical Review B*, 99(22):220507, 2019.

[115] Xiao-Chuan Wu, Anna Keselman, Chao-Ming Jian, Kelly Ann Pawlak, and Cenke Xu. Ferromagnetism and spin-valley liquid states in moiré correlated insulators. *Physical Review B*, 100(2):024421, 2019.

[116] Xiao-Chuan Wu, Kelly Ann Pawlak, Chao-Ming Jian, and Cenke Xu. Emergent superconductivity in the weak mott insulator phase of bilayer graphene moir\'e superlattice. *arXiv preprint arXiv:1805.06906*, 2018.

[117] Jing Xia, Yoshiteru Maeno, Peter T. Beyersdorf, M. M. Fejer, and Aharon Kapitulnik. High resolution polar kerr effect measurements of sr_2ruo_4: Evidence for broken time-reversal symmetry in the superconducting state. *Phys. Rev. Lett.*, 97:167002, Oct 2006.

[118] Cenke Xu and Leon Balents. Topological superconductivity in twisted multilayer graphene. *Physical review letters*, 121(8):087001, 2018.

[119] Xiao Yan Xu, KT Law, and Patrick A Lee. Kekulé valence bond order in an extended hubbard model on the honeycomb lattice with possible applications to twisted bilayer graphene. *Physical Review B*, 98(12):121406, 2018.

[120] Matthew Yankowitz, Shaowen Chen, Hryhoriy Polshyn, Yuxuan Zhang, K Watanabe, T Taniguchi, David Graf, Andrea F Young, and Cory R Dean. Tuning superconductivity in twisted bilayer graphene. *Science*, 363(6431):1059–1064, 2019.

[121] Matthew Yankowitz, Qiong Ma, Pablo Jarillo-Herrero, and Brian J LeRoy. van der waals heterostructures combining graphene and hexagonal boron nitride. *Nature Reviews Physics*, 1(2):112–125, 2019.

[122] Norman Y Yao, Fabian Grusdt, Brian Swingle, Mikhail D Lukin, Dan M Stamper-Kurn, Joel E Moore, and Eugene A Demler. Interferometric approach to probing fast scrambling. *arXiv preprint arXiv:1607.01801*, 2016.

[123] Yi-Zhuang You, Andreas WW Ludwig, and Cenke Xu. Sachdev-ye-kitaev model and thermalization on the boundary of many-body localized fermionic symmetry-protected topological states. *Physical Review B*, 95(11):115150, 2017.

[124] Noah FQ Yuan and Liang Fu. Erratum: Model for the metal-insulator transition in graphene superlattices and beyond [phys. rev. b 98, 045103 (2018)]. *Physical Review B*, 98(7):079901, 2018.

[125] Ya-Hui Zhang, Dan Mao, Yuan Cao, Pablo Jarillo-Herrero, and T Senthil. Nearly flat chern bands in moir$\vec{e}$ superlattices. *Physical Review B*, 99(7):075127, 2019.

[126] Ya-Hui Zhang, Dan Mao, and T Senthil. Twisted bilayer graphene aligned with hexagonal boron nitride: anomalous hall effect and a lattice model. *Physical Review Research*, 1(3):033126, 2019.

[127] Ya-Hui Zhang and T Senthil. Bridging hubbard model physics and quantum hall physics in trilayer graphene/h- bn moir$\vec{e}$ superlattice. *Physical Review B*, 99(20):205150, 2019.